

SMR: 1133/16

WINTER COLLEGE ON
SPECTROSCOPY AND APPLICATIONS

(8 - 26 February 1999)

"Raman Spectroscopy in Nanostructures"

A. Principles and Methods of Raman Spectroscopy
B. Applications to Nanostructured Systems

presented by:

Gino MARIOTTO

Università degli Studi di Trento

Dipartimento di Fisica

Trento

Italy

These are preliminary lecture notes, intended only for distribution to participants.

strada costiera, 11 - 34014 trieste italy - tel. +39 40 2240111 fax +39 40 224163 - sci_info@ictp.trieste.it - www.ictp.trieste.it

RAMAN SPECTROSCOPY IN NANOSTRUCTURES

G. MARIOTTO

PHYSICS DEPARTMENT

TRENTO - ITALY

A - PRINCIPLES AND METHODS OF R.S.

- BACKGROUND ABOUT LIGHT SCATTERING
- POLARIZABILITY MODEL
- RAMAN SCATTERING BY PHONONS
- EXPERIMENTAL CONSIDERATIONS
- MICRO-SAMPLING APPROACH

B - APPLICATIONS TO NANOSTRUCTURED SYSTEMS

1) MICRO-RAMAN SPECTROSCOPY ON POROUS SILICON

- PHYSICAL PROPERTIES OF p-Si
- DEPTH-PROFILING EXPERIMENTS
- PHONON CONFINEMENT MODELS

2) LOW-FREQUENCY RAMAN SPECTROSCOPY ON SEMICONDUCTOR AND METAL PARTICLES

- RAMAN SCATTERING FROM ACOUSTIC PHONONS IN:
 - a - SEMICONDUCTOR QUANTUM DOTS (Si, Ge, CdS)
 - b - METAL CLUSTERS (Ag)

→ WINTER COLLEGE ON "SPECTROSCOPY AND APPLICATIONS"
ICTP - TRIESTE - FEBRUARY 18-22, 1999

RAMAN SPECTROSCOPY IN NANOSTRUCTURES

REFERENCES

1) R.S. PRINCIPLES AND METHODS

- M. CARDONA (ed.)
"LIGHT SCATTERING IN SOLIDS"
TOPICS APPL. PHYS. VOL. 5 (SPRINGER, 1975)
- M. CARDONA and G. GUNTERDIT (eds.)
"LIGHT SCATTERING IN SOLIDS II"
TOPICS APPL. PHYS. VOL. 50 (SPRINGER, 1982)
- W. HAYES
"SCATTERING OF LIGHT BY SOLIDS"
CONTEMP. PHYS. 16, 69-91 (1975)
- P. DHAMELINCOURT et al.
"RAMAN MICRO SPECTROMETRY"
SPECTROSCOPY EUROPE VOL 5/No. 2, 16-26 (1993).
- B. CHASE
"A NEW GENERATION OF RAMAN INSTRUMENTATION"
APPLIED SPECTROSCOPY VOL. 48/No. 7, 14A-19A (1994).

2) PHONON CONFINEMENT MODELS

- H. RICHTER, Z.P. WANG and L. LEY
SOLID STATE COMMUN. 39, 625 (1981)
- I. H. CAMPBELL and P. H. FAUCHET
SOLID STATE COMMUN. 58, 739 (1986)

3) R.S. ON SEMICONDUCTOR AND METAL NANOPARTICLES

- D.R. DOS SANTOS and I. L. TORRIANI
SOLID STATE COMMUN. 85, 307 (1993)
- G. MARWITT, F. ZIGLID and F. L. FREIRE, Jr.
J. NON-CRYSTALL. SOLIDS 192&193, 253 (1995)
- K.E. LIPINSKA-KALITA, G. MARWITT and E. ZANGHELLINI
PHIL. MAG. B 71, 547 (1995)
- M. FUJII et al.
PHYS REV. B 44, 6243 (1991); ibidem 54, R8373 (1996)
- G. MARWITT et al., EUROPHYS. LETT. 6, 239 (1988).

INTRODUCTION

- Light scattering is a general expression to indicate a class of two-photon processes between electro-magnetic radiation and condensed matter.
- The subject is of great interest for the study of solids because it gives detailed information about their elementary excitations.
- The scattering of light arises through the modulation of the **dielectric constant** of the system by internal excitations. The dielectric constant is sensitive to any change of the electronic state of solids and this permits coupling with essentially all types of excitations in solids (plasmons, excitons, **phonons**, magnons).
- Hereafter we shall deal with **Raman scattering by phonons**.

PHENOMENOLOGY OF LIGHT SCATTERING

When a monochromatic light of frequency ν_0 impinges on a solid characterized by elementary excitations of frequency ν_k we can find, under certain circumstances, that scattered light contains, besides the frequency ν_0 , also frequencies ν_k given by:

$$\nu_s = \nu_0 \pm \nu_k$$

- The interactions giving rise to elastically scattered component at ν_0 are usually referred to as **Rayleigh scattering**.
- The sidebands occurring at $\nu_0 \pm \nu_k$ arise from inelastic scattering processes and provide us directly with the frequency (or energy) of the k -th elementary excitation within the solid.

- The sidebands occurring at $\nu_0 - \nu_k$ are referred to as **Stokes** components, while the sidebands at $\nu_0 + \nu_k$ are referred to as **anti-Stokes** components.
- If the sidebands $\nu_s = \nu_0 \pm \nu_k$ are due to:
 - i) acoustic phonons (**Brillouin scattering**);
 - ii) electronic excitations or optic phonons (**Raman scattering**).
- Raman scattering sidebands occur in the wavenumber range of $\sim 10 \div 1000 \text{ cm}^{-1}$, while Brillouin scattering sidebands are confined below $\sim 1 \text{ cm}^{-1}$ far from the laser energy.

The **wavenumber unit (cm^{-1})** is used by spectroscopists.

1 cm^{-1} corresponds to a frequency of **30 GHz** and to an energy of **$\sim 1.24 \times 10^{-4} \text{ eV}$** .

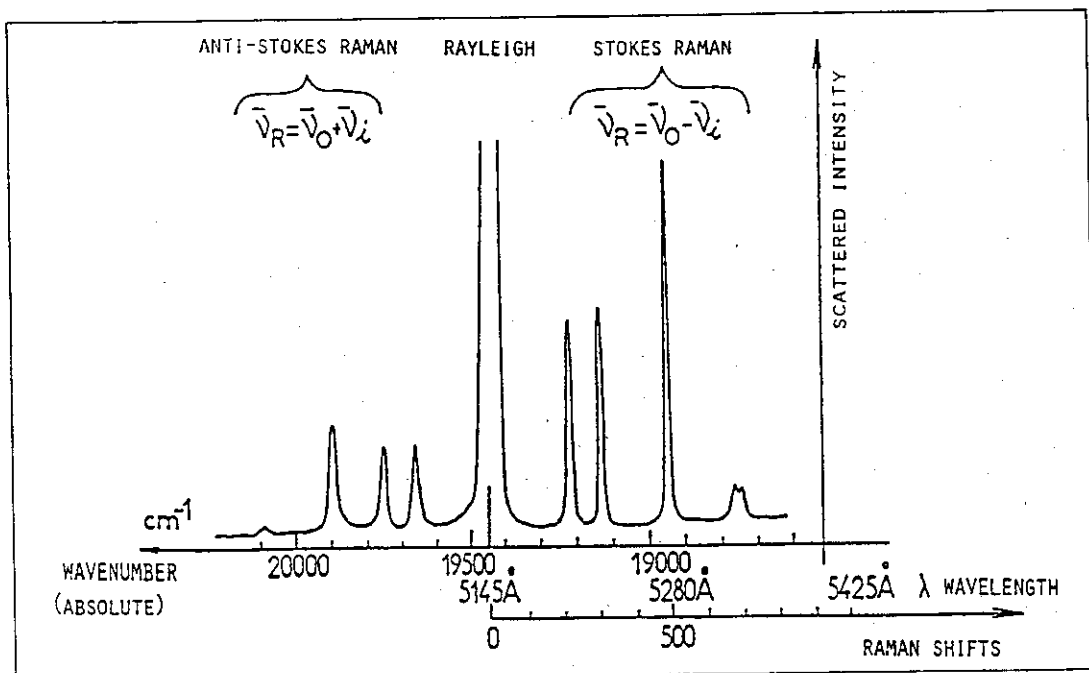


Figure 1. Schematic representation of a Raman spectrum excited with the green line of an argon ion laser, $\lambda_0 = 514.5 \text{ nm}$.

HISTORICAL BACKGROUND

- Raman scattering was independently observed in 1928 by:
 - i) Raman & Krishnam in liquids;
 - ii) Lansberg & Mandestam in crystals.
- Raman observed that the light from a mercury lamp was scattered by benzene in such a way that the spectrum of light contained some additional lines, besides that of mercury itself, occurring in both sides at higher and lower frequency than that of mercury lamp.
- Raman spectrum of liquid carbon tetrachloride excited at 435.3 nm and recorded over a photographic film.
- Smekal in 1923 derived the following formula from quantum mechanical considerations on atomic transitions:

$$h\nu_0 + E_0 = h\nu_s + E_m$$

where E_0 and E_m stand for energy eigenvalues of the medium before and after the light scattering process, and ν_0 and ν_s are the frequency of the incident and scattered radiation.

- Therefore the scattering of frequency-shifted radiation (i.e.: the inelastic scattering of light), is a **quantum effect**.
- Although no complete theory of light scattering processes can be built up without an extensive use of quantum mechanical concepts, nevertheless some basic insights can be obtained from pure classical considerations.
- **Molecular model** of light scattering processes.

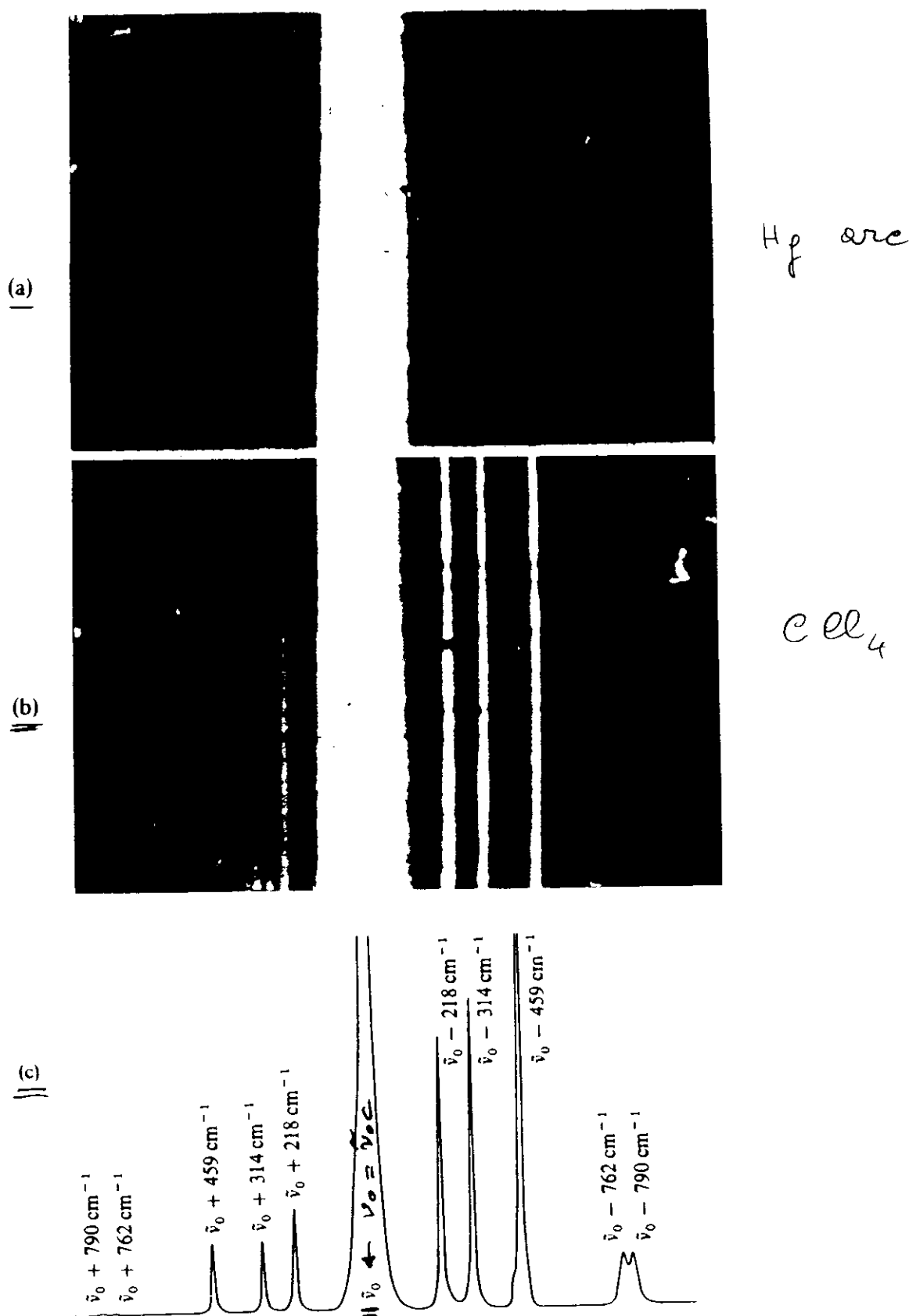


Fig. 1.2 (a) Spectrum of a mercury arc in the region of 4358.3 \AA (435.83 nm , $\nu_0 = 22\,938 \text{ cm}^{-1}$); (b) Rayleigh and Raman spectra of carbon tetrachloride (liquid) excited by mercury arc radiation, $\nu_0 = 22\,938 \text{ cm}^{-1}$; (c) Rayleigh and Raman spectra of carbon tetrachloride (liquid) excited by an argon ion laser, $\nu_0 = 20\,487 \text{ cm}^{-1}$ (4879.9 \AA , 487.99 nm). The spectra in Fig. 1.2(a) and (b) are facsimiles of spectra recorded by Raman and Krishnan (*Proc. Roy. Soc.*, vol. 122, p. 23, 1929) and were photographically recorded.

MOLECULAR MODEL OF LIGHT SCATTERING

- PURELY CLASSICAL TREATMENT

- BASIC ASSUMPTIONS OF CLASSICAL THEORY:

- 1- THE LIGHT IS SCATTERED AS A RESULT OF FORCED OSCILLATIONS OF THE MOLECULE DIPOLE MOMENT, INDUCED BY THE ELECTRO-MAGNETIC FIELD OF THE INCIDENT LIGHT WAVE
- 2- THE LIGHT IS MAINLY SCATTERED BY THE OUTER ELECTRON SHELLS OF THE MOLECULE: THE ATOMIC NUCLEI, WHICH ARE THE BACKBONE OF THE MOLECULE BEING DISPLACED INSIGNIFICANTLY;
- 3- THE LIGHT SCATTERING IS DUE TO THE COUPLING BETWEEN THE MOVEMENT OF THE ELECTRONS IN THE MOLECULE AND THE MOVEMENT OF THE NUCLEI AND IS ASSOCIATED WITH THE MODULATION OF THE INDUCED DIPOLE MOMENT BY THE MOLECULAR SKELETAL VIBRATIONS

→ THE STRENGTH OF THE INDUCED DIPOLE MOMENT BY A LIGHT WAVE $\vec{E} = \vec{E}_0 \cos(\omega_0 t)$ IS

$$\vec{P} = \alpha \vec{E} \quad \leftarrow \text{IN LINEAR APPROXIMATION}$$

- $\vec{P}(t)$ IS OSCILLATING AT A FREQUENCY WHICH DEPENDS ON ω_0 AS WELL AS ON THE VIBRATIONAL FREQUENCY OF THE MOLECULE THROUGH α
- α IS THE POLARIZABILITY OF THE MOLECULE AND, IN CLASSICAL THEORY, IS A PHENOMENOLOGICAL QUANTITY WHICH DEPENDS ON THE ^{INSTANTANEOUS!} NUCLEI POSITION

- LET q_k THE VIBRATIONAL COORDINATE WHICH DESCRIBES THE k -TH VIBRATIONAL MODE OF THE MOLECULE, SO THAT WE MAY WRITE $\alpha = \alpha(q_k)$
- IF q_k IS SMALL, THEN α CAN BE EXPANDED IN A POWER SERIES OF q_k AROUND THE EQUILIBRIUM VALUE $q_k^0 = 0$:

$$\alpha(q_k) = \alpha_0 + \left(\frac{\partial \alpha}{\partial q_k} \right)_0 q_k + \text{c.c.}$$

- TAKING $q_k = q_{k0} \cos(\omega_k t + \phi_k)$ WE WRITE :

$$\begin{aligned} \vec{P}(t) &= \alpha \cdot \vec{E} \\ &= \left[\alpha_0 + \left(\frac{\partial \alpha}{\partial q_k} \right)_0 q_{k0} \cos(\omega_k t + \phi_k) \right] \cdot \vec{E}_0 \cos(\omega_0 t) \\ &= \alpha_0 \vec{E}_0 \cos(\omega_0 t) + \left(\frac{\partial \alpha}{\partial q_k} \right)_0 q_{k0} \vec{E}_0 \cos(\omega_0 t) \cos(\omega_k t + \phi_k) \end{aligned}$$

$$\begin{aligned} \Rightarrow \vec{P}(t) &= \alpha_0 \vec{E}_0 \cos(\omega_0 t) \quad \leftarrow \text{RAYLEIGH SCATTERING} \\ &+ \frac{1}{2} \left(\frac{\partial \alpha}{\partial q_k} \right)_0 q_{k0} \vec{E}_0 \cos[(\omega_0 - \omega_k)t + \phi_k] \\ &+ \frac{1}{2} \left(\frac{\partial \alpha}{\partial q_k} \right)_0 q_{k0} \vec{E}_0 \cos[(\omega_0 + \omega_k)t + \phi_k] \end{aligned}$$

- THEREFORE, THE MODULATION OF THE INDUCED DIPOLE MOMENT BY THE VIBRATIONS OF ATOMIC NUCLEI GIVES RISE TO SUM AND DIFFERENCE FREQUENCIES $\omega_0 + \omega_k$ AND $\omega_0 - \omega_k$ IN THE SPECTRUM OF THE SCATTERED RADIATION.
- THE SIDE BANDS AT $\pm \omega_k$ WITH RESPECT TO ω_0 ARE USUALLY REFERRED TO AS RAMAN SCATTERING
- $\omega_0 - \omega_k \rightarrow$ RAMAN STOKES SCATTERING
 $\omega_0 + \omega_k \rightarrow$ RAMAN ANTI-STOKES SCATTERING
- BUT, TO OBSERVE R.S. IT SHOULD BE $\left(\frac{\partial \alpha}{\partial q_k} \right)_0 \neq 0!$

THE POLARIZABILITY TENSOR : $\tilde{\alpha}$

- IN GENERAL, THE SCATTERING SYSTEMS ARE CHARACTERIZED BY A CERTAIN ANISOTROPY DEGREE, THEIR PROPERTIES DIFFERING IN DIFFERENT DIRECTIONS!
- FOR SUCH SYSTEMS, THE INDUCED DIPOLE MOMENT \vec{P} DOES NOT POINT IN THE DIRECTION OF THE ELECTRIC FIELD VECTOR OF THE INCIDENT WAVE \vec{E}
- THIS FACT IS USUALLY EXPRESSED AS :

$$P_i = \sum_j \alpha_{ij} E_j$$

- THE SET OF PARAMETERS α_{ij} , WHICH DETERMINE THE PROPERTIES OF THE SCATTERED RADIATION, CONSTITUTE THE SCATTERING TENSOR $\tilde{\alpha}$
- IN CLASSICAL APPROXIMATION $\tilde{\alpha}$ IS REAL AND SYMMETRIC, WITH A MAXIMUM OF SIX COMPONENT
- IN PRACTICAL EXPERIMENT IT IS POSSIBLE TO SEPARATE THE SCATTERING CONTRIBUTIONS FROM THE DIFFERENT COMPONENTS OF $\tilde{\alpha}$ BY USING LINEARLY POLARIZED INCIDENT LIGHT (LASER BEAMS) AND PROPER POLARIZATION ANALYZERS FOR THE SCATTERED RADIATION.
- IF, FOR INSTANCE, \vec{E} IS ARRANGED TO HAVE ONE NON-VANISHING COMPONENT ONLY : E_z AND THE POLARIZER FILTER AXIS IS CONVENIENTLY ORIENTED $\parallel z$, IT BECOMES POSSIBLE TO ISOLATE THE LIGHT SCATTERED ACCORDING TO THE α_{zz} ELEMENT SEPARATELY.

COMPLEMENTARITY BETWEEN RAMAN SPECTROSCOPY AND IR

- SYMMETRY OF VIBRATIONS!


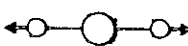
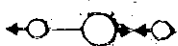
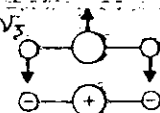






Molecule	 <chem>CO2</chem>		
Mode of vibration	ν_1 	ν_2 	ν_3 
Variation of polarizability with normal coordinate (schematic)			
Polarizability derivative	$\neq 0$	$= 0$	$= 0$
Raman activity	Yes	No	No
Variation of dipole moment with normal coordinate (schematic)			
Dipole moment derivative	$= 0$	$\neq 0$	$\neq 0$
Infrared activity	No	Yes	Yes

Fig. 3 Polarizability and dipole moment variations in the neighbourhood of the equilibrium position and vibrational Raman and infrared activities for a linear ABA molecule

PROPERTIES OF INELASTIC PHOTON-PHONON SCATTERING

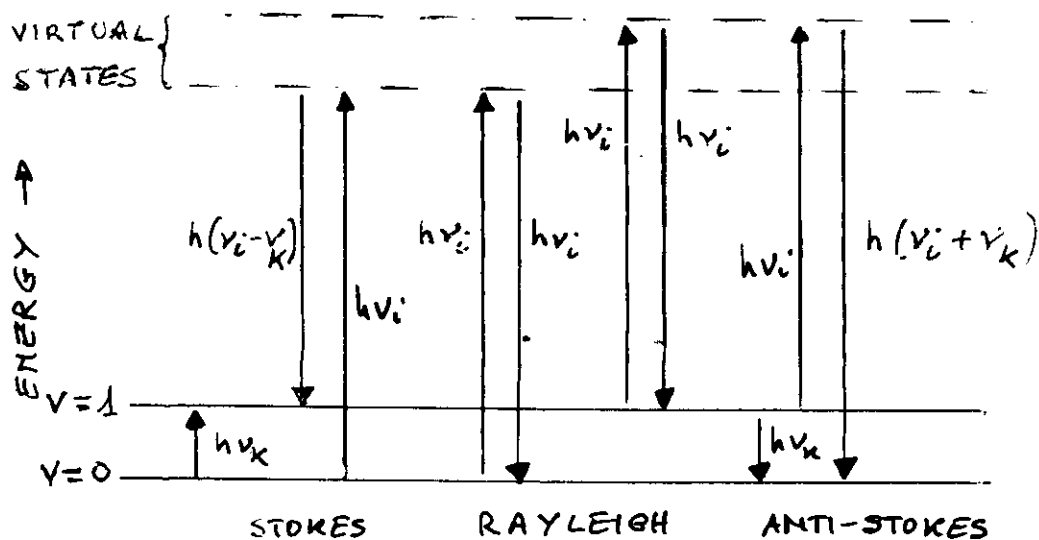
• CONSERVATION RULES (ONE-PHONON PROCESS)

ENERGY $\rightarrow \quad \nu_i = \nu_s \pm \nu_k$

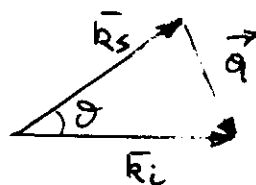
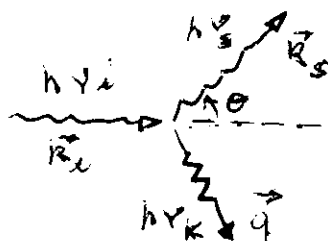
WAVE VECTOR $\vec{k}_i = \vec{k}_s \pm \vec{q} \quad (|\vec{k}| = \frac{2\pi}{\lambda})$

WHERE \vec{k} HAS THE DIRECTION OF THE NORMAL OF THE WAVEFRONT OF THE LIGHT

SCHEMATIC REPRESENTATION OF AN ENERGY TRANSFER MODEL FOR LIGHT SCATTERING PROCESSES

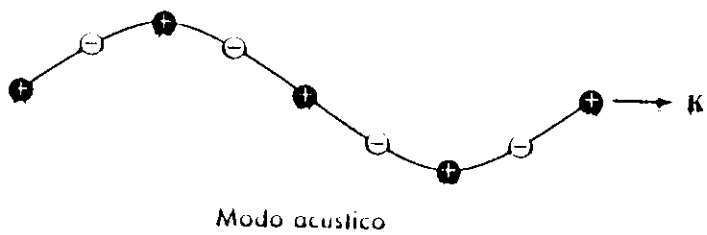
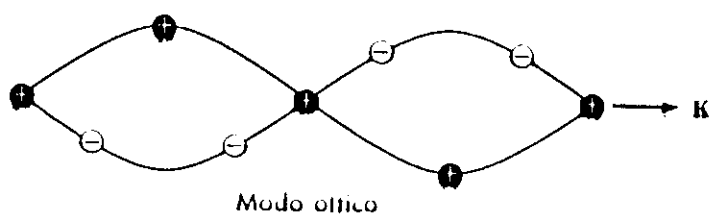
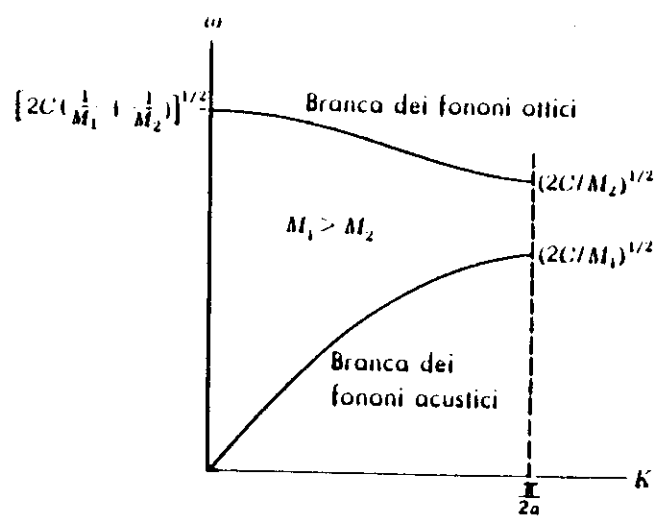


SCHEMATIC REPRESENTATION OF THE SCATTERING
OF A PHOTON (ν_i, \vec{k}_i) WITH THE CREATION OF A
PHONON (ν_s, \vec{q}) : WAVE-VECTOR CONSERVATION.



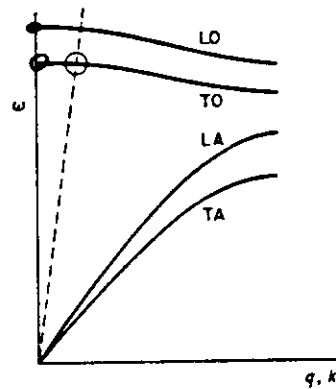
LIGHT SCATTERING BY PHONONS

- In crystalline solids, besides the molecular vibrations (internal modes), lattice vibrations (external modes) exist. These lattice deformations are transmitted throughout the crystal and are described by plane waves (**phonons**) with wave vector **q** either perpendicular (transverse) or parallel (longitudinal) to atomic displacements.
- Lattice vibrations are classified into acoustic and optical modes, the related plane waves being called acoustic and optical phonons. Optical phonons are much more energetic than the acoustic ones (i.e.: elastic waves in a continuum).
- The phonon spectrum of a crystal consists of both acoustic and optical phonon branches.
- In general, optical modes of crystals are less energetic than molecular vibrations. In fact:
 - molecular vibrations occur in the range of $\approx 400 \div 4000 \text{ cm}^{-1}$ (i.e.: $\approx 0.05 \div 0.5 \text{ eV}$);
 - optical lattice modes occur in the range of $\approx 10 \div 1000 \text{ cm}^{-1}$.
- Raman scattering from crystalline systems ranges between few wavenumbers far from the Rayleigh line and some thousands of wavenumbers. Therefore its detection in a light scattering experiment requires the use of a laser, as source of monochromatic light beam, and high contrast spectrometers, as energy analyzer systems.
- Schematic representation of phonon propagation.



DISPERSIVE EFFECTS

- In principle, scattering experiments on a crystalline system allow to determine the phonon dispersion curves of the crystal (i.e.: the frequency ω vs. \mathbf{q}), according to both energy and wavevector conservation rules.
- Unfortunately, by scattering experiments with visible light only the phonons with $\mathbf{q} \cong 0$, i.e.: phonons occurring very near to the centre of the first Brillouin zone (Γ -point of BZ), can be probed.
- In fact, for light of $\lambda = 500$ nm we have: $|\mathbf{k}_i| \approx |\mathbf{k}_s| \cong 10^5 \text{ cm}^{-1}$ and $|\mathbf{q}| = 2 |\mathbf{k}| \sin (\theta/2)$, where we assumed: $|\mathbf{k}| = |\mathbf{k}_i| \cong |\mathbf{k}_s|$.
- This means that $|\mathbf{q}| \leq 2 |\mathbf{k}| \cong 2 \cdot 10^5 \text{ cm}^{-1} \ll \pi/a (\cong 10^8 \text{ cm}^{-1})$.
- Then, only phonons with very long wavelengths, much longer than the lattice spacings, are observed in first-order Raman scattering from crystals.
- • It should be emphasized here that the magnitude of the wave vector \mathbf{q} determines the spatial resolution by which we can probe the crystalline systems.
- In contrast to light scattering experiments, by using X-rays and thermal neutrons (with $\mathbf{k} \geq 10^8 \text{ cm}^{-1}$) we could explore phonons at all the wavelengths down to interatomic separation ($a \cong 0.1$ nm). In fact, X-ray and neutron scattering experiments are used to determine the phonon dispersion curves of crystalline solids.
- The magnitude of wave vector \mathbf{q} is not so important in Raman scattering (\rightarrow optical phonons), but it is very crucial for Brillouin scattering (\rightarrow acoustic phonons), since the frequency of acoustic phonons varies almost linearly vs. \mathbf{q} near the Γ -point of the BZ.



Superposition of phonon spectrum (continuous lines) and photon spectrum (broken line).

RANGE OF FREQUENCY VS. \vec{k}
(LOG-LOG SCALE)

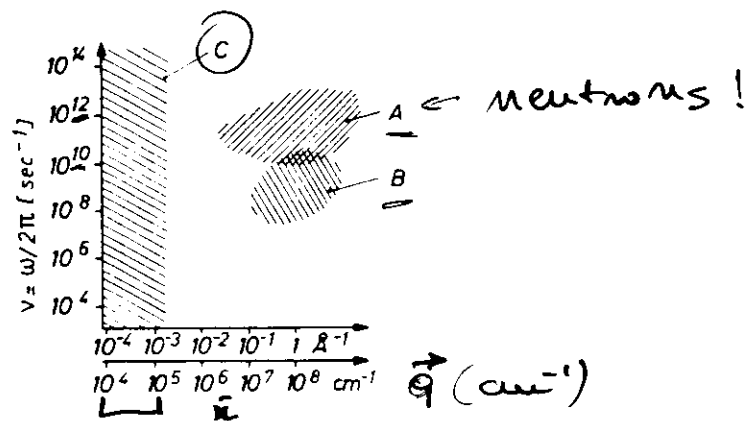


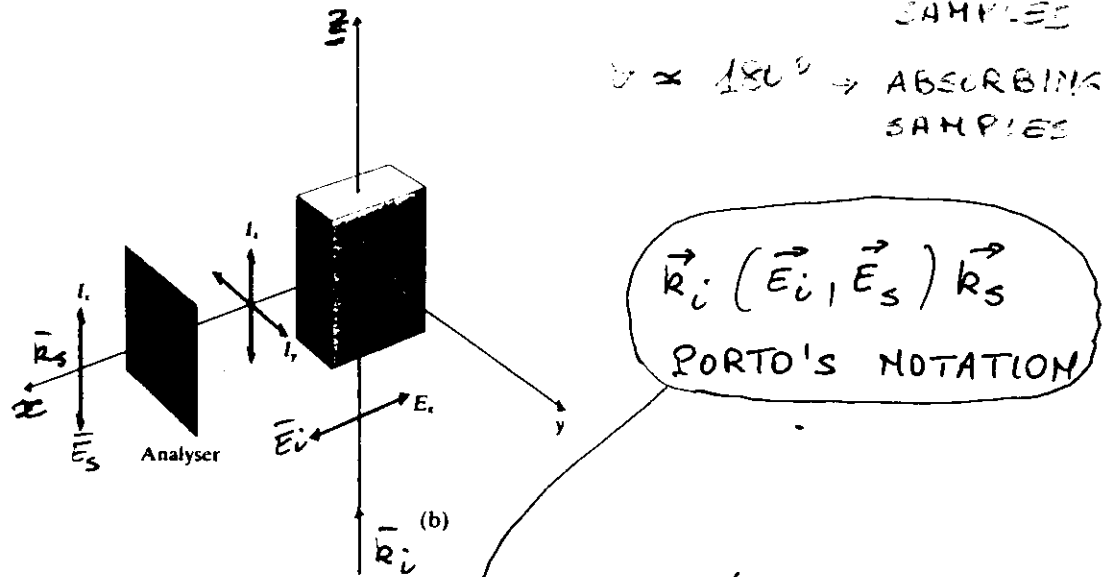
Fig. 6. Range of frequency $\nu = \omega/2\pi$ and wave vector \vec{k} of the Fourier components accessible to scattering experiments. A: Region of conventional neutron spectrometers. B: region of the "90°-spectrometer" (Section 3.2). C: Raman, infrared, and Laser spectroscopy

RAMAN SCATTERING EXPERIMENTS

- Polarized monochromatic laser beams are generally used to excite Raman spectra of crystals.
- **Macro-sampling** approach is usually adopted for Raman scattering experiments carried out from crystalline systems. In this approach, the incident laser light is focused on the sample by a lens of proper focal length.
- Nowadays, Raman scattering experiments on nanostructured systems are preferentially carried out in **micro-sampling** configuration, because of the much higher spatial resolution attainable in focusing the laser beam by a microscope objective.
- Scattered light is collected into an optical system placed at some angle θ with respect to the direction of the incident laser beam. This angle θ defines the scattering geometry.
- Polarization of the scattered light can be properly determined by a polarization analyzer system (polarizing plate + scrambler).
- Scattered radiation is frequency resolved by a spectrometer, i.e.: a double- or triple-monochromator, mounting (holographic) gratings, and is collected into a photon detector, i.e.: PMT (photomultiplier tube) or CCD (charge coupled device).
- Photomultiplier tube are usually operated in photon counting mode to increase their sensitivity in detecting weak light signals. Since the end of 80s, new photon detectors (CCD array detectors) have been developed and are currently used by Raman spectroscopy apparatus, especially by those equipped with microprobe sampling facilities.
- Schematic representation of Raman scattering from crystals.

RAMAN SCATTERING FROM SINGLE-CRYSTALS

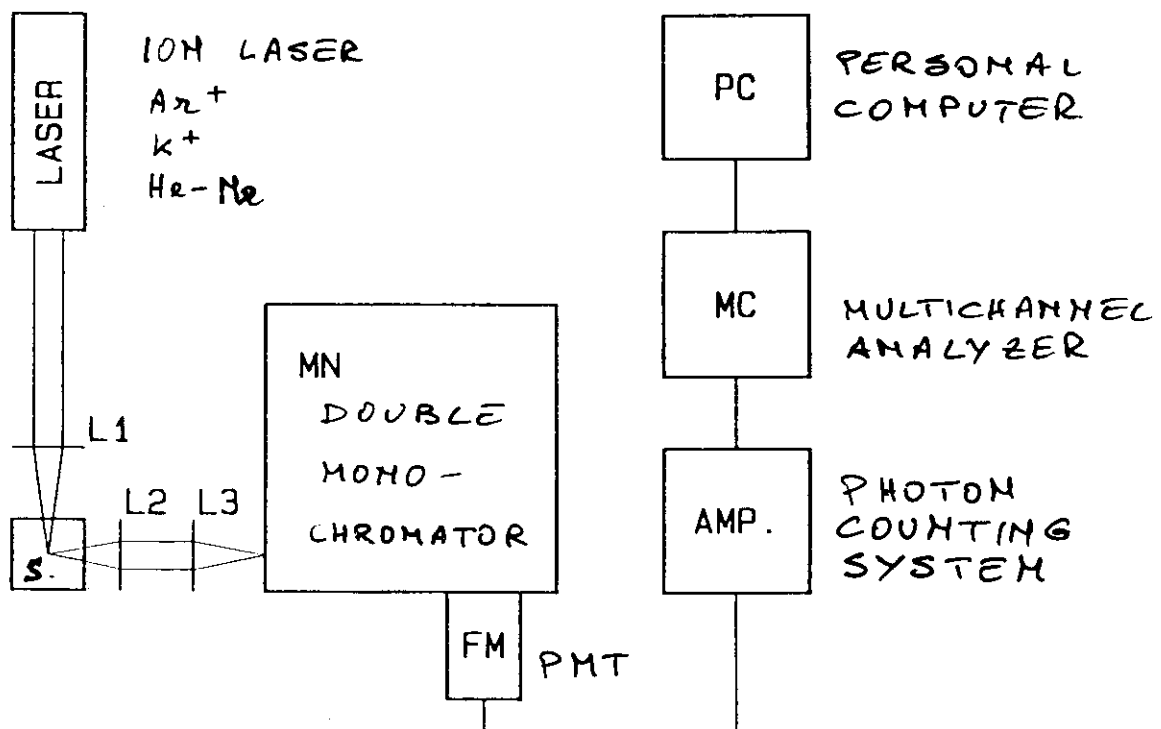
- SCATTERING GEOMETRIES: $\theta = 90^\circ \rightarrow$ TRANSPARENT SAMPLES



Raman scattering from a crystal: geometry for $z(xz)x$ measurement

- SELECTION OF POLARIZATION TENSOR COMPONENTS

→ TYPICAL RAMAN SCATTERING EXPERIMENTAL SET-UP



SPECTRAL INTENSITY OF SCATTERED LIGHT

- From a microscopic point of view, the scattering of light in a crystal is caused by local fluctuations of the dielectric constant ϵ due to lattice deformations associated to its internal excitations.
- The spectral intensity of the scattered light by an elementary excitation of frequency ω and wavevector \mathbf{q} in crystalline solids can be properly expressed in terms of Fourier transformation of the autocorrelation function of space-time fluctuation, $\delta\epsilon(\mathbf{r},t)$, of the dielectric constant $\epsilon(\mathbf{r},t)$ from the equilibrium value ϵ_0 :

$$I(\mathbf{q},t) = (A/2\pi) \int_{-\infty}^{+\infty} dt e^{-i\omega t} \langle \delta\epsilon^*(\mathbf{q},0) \cdot \delta\epsilon(\mathbf{q},t) \rangle$$

where $\omega = \omega_i - \omega_s$.

The star * denotes the complex conjugated, $\langle \delta\epsilon^*(\mathbf{q},0) \cdot \delta\epsilon(\mathbf{q},t) \rangle$ is the time-correlation function, and:

$$A = (I_0 \omega_0^4) / (16 \pi R^2 c^4 \epsilon_0)$$

Finally, $\delta\epsilon(\mathbf{q},t)$ is the space-transform of the dielectric function fluctuation :

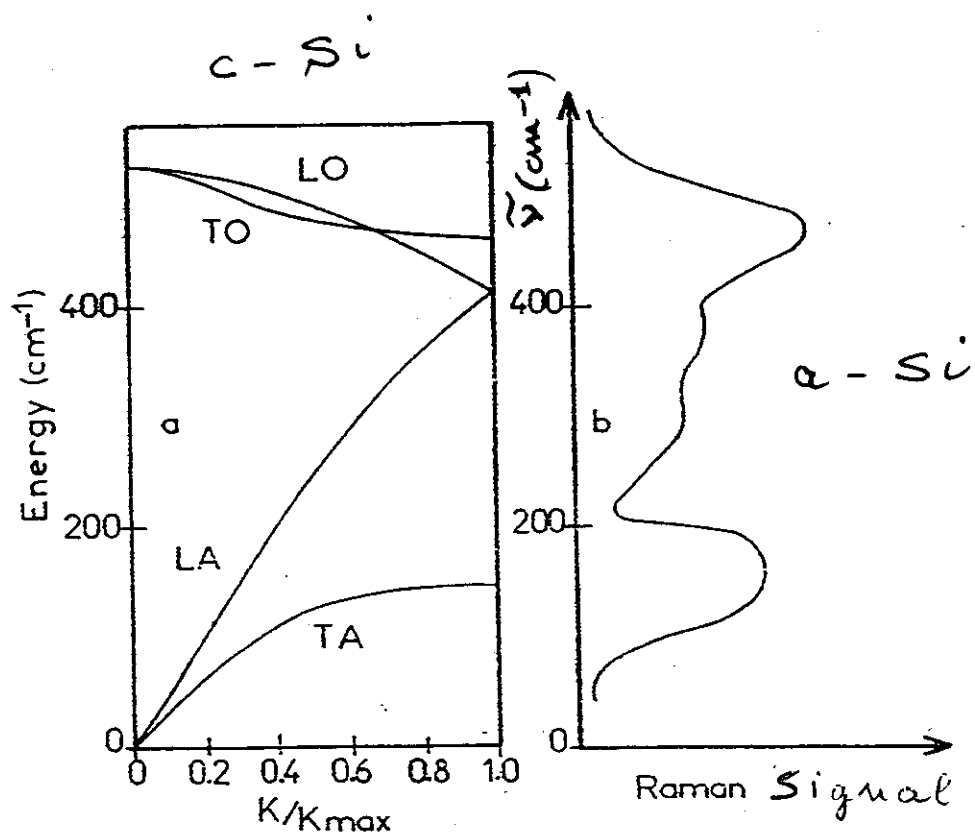
$$\delta\epsilon(\mathbf{q},t) = \int_{-\infty}^{+\infty} d\mathbf{r} e^{-i\mathbf{q}\cdot\mathbf{r}} \delta\epsilon(\mathbf{r},t).$$

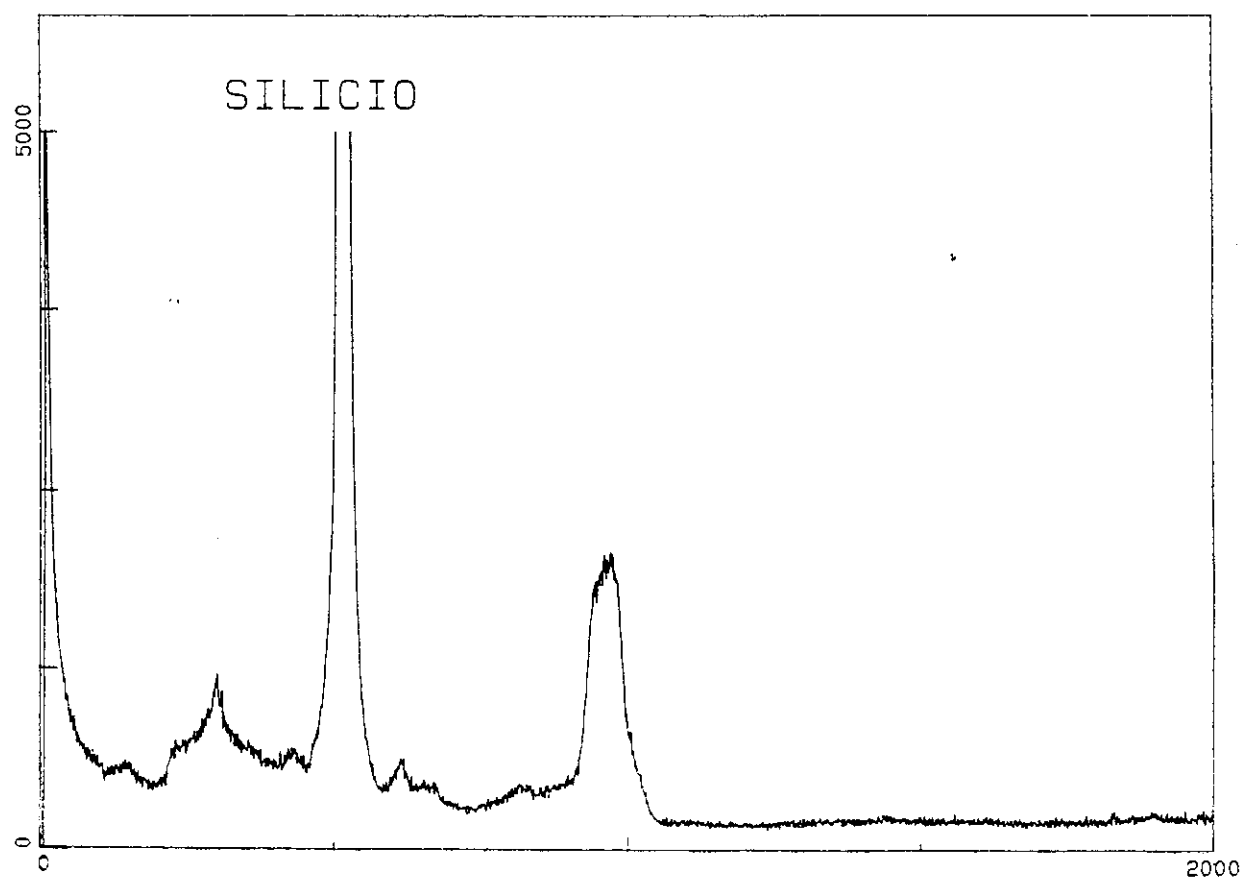
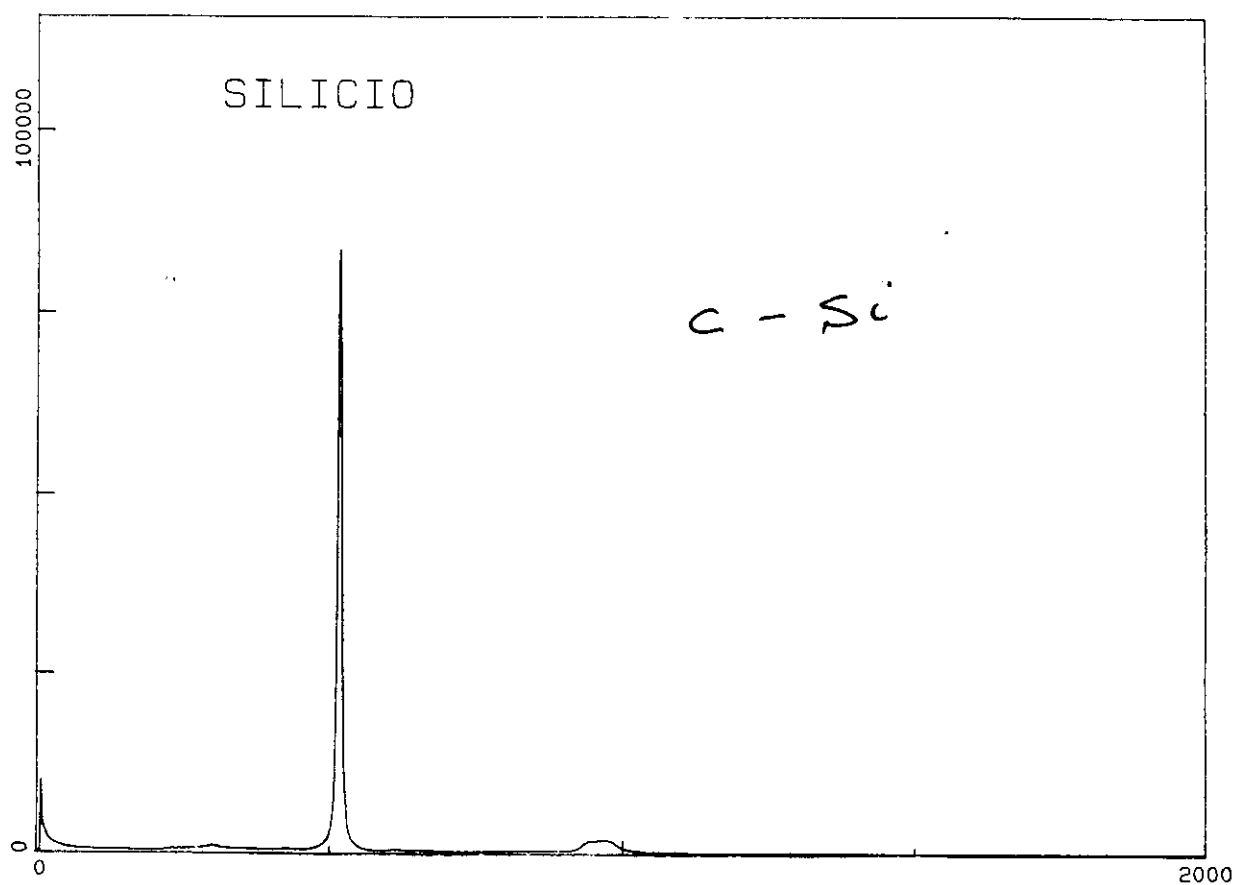
- Notice the ω_0^4 -dependence of the scattered light intensity.

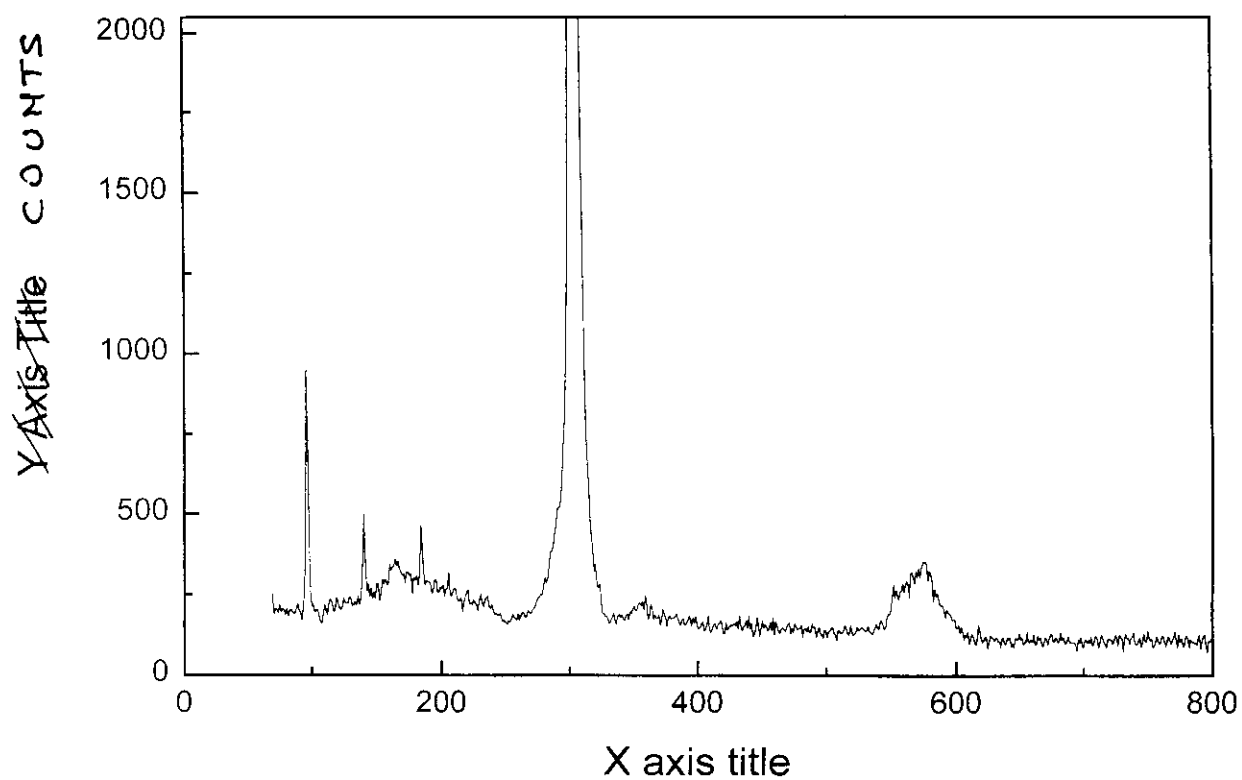
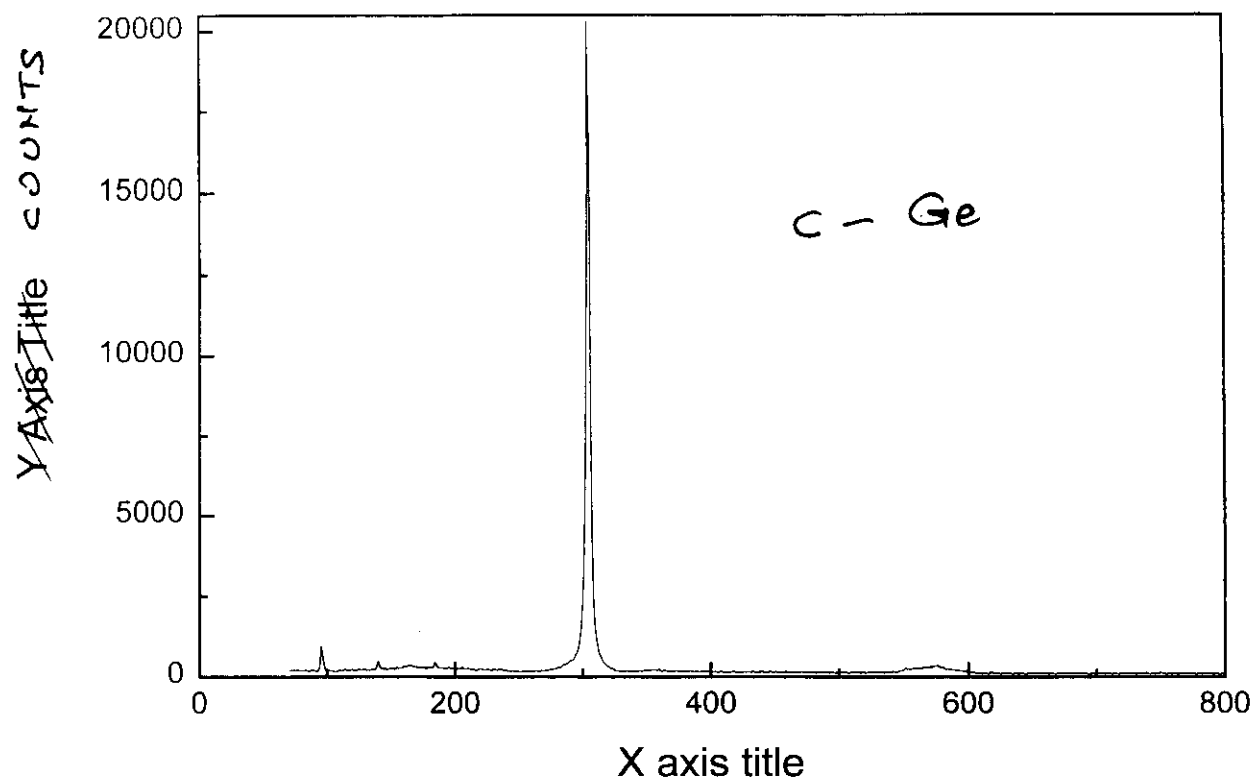
SPECTRAL CHARACTERISTICS OF FIRST-ORDER RAMAN SCATTERING BY PHONONS

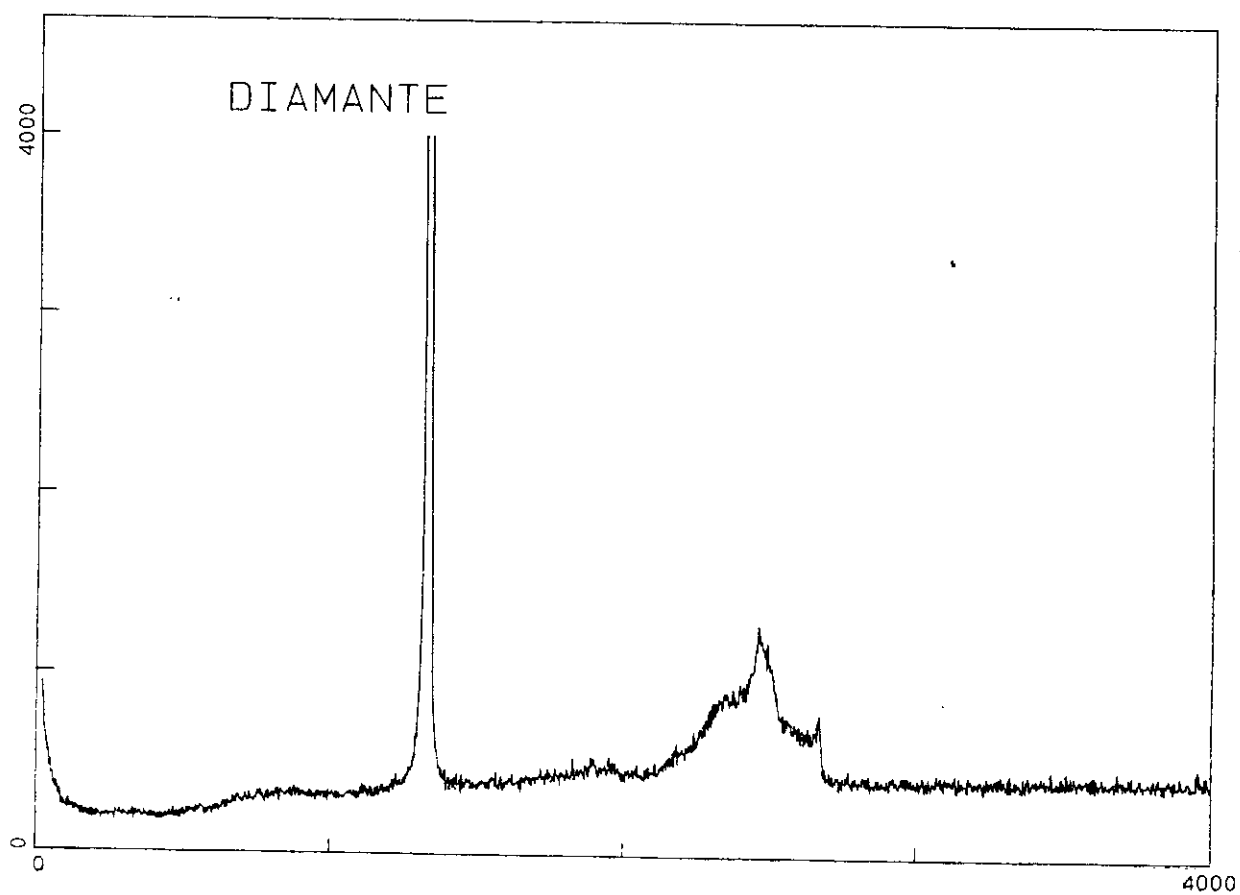
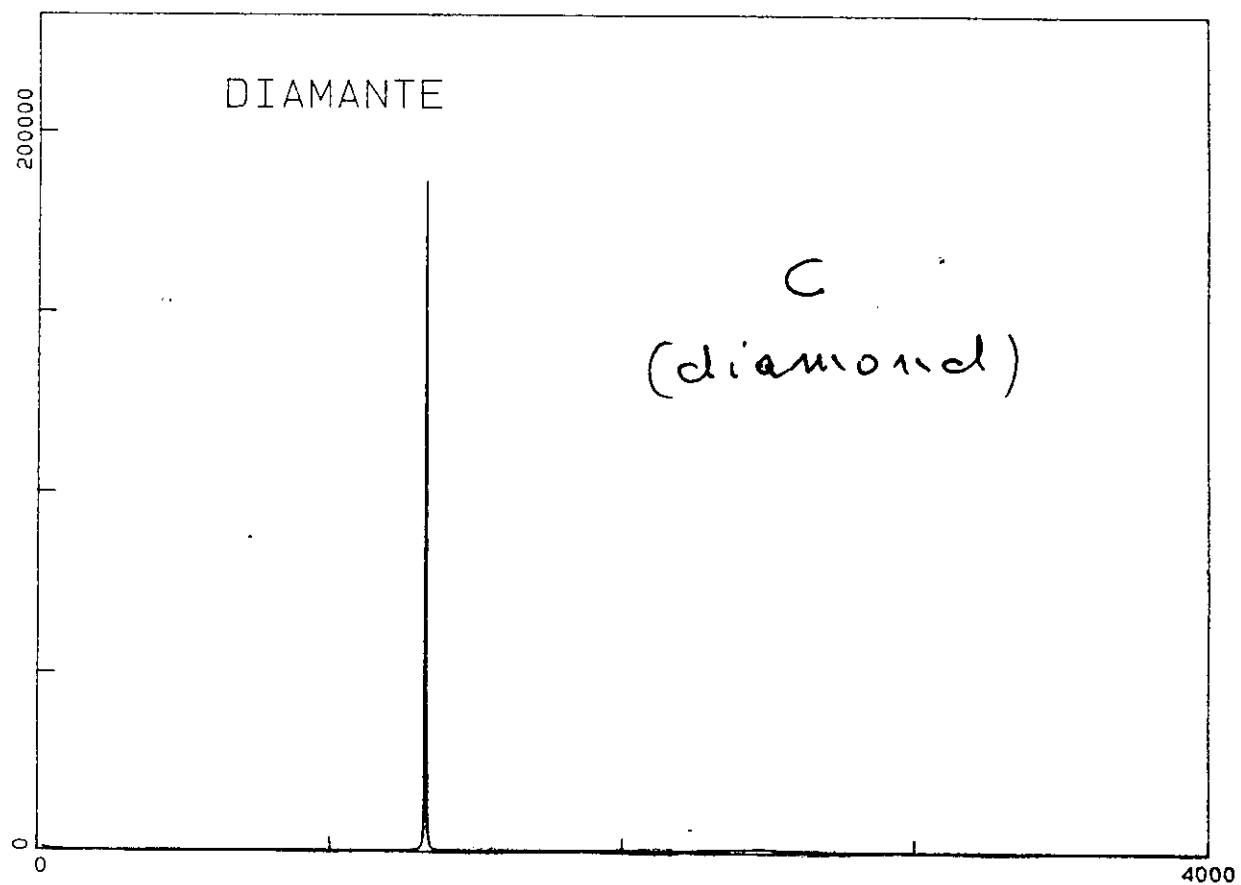
- Raman spectra of crystalline solids consist of a set of discrete and relatively sharp peaks (lines), due to light scattering by optical phonons at the centre of the first Brillouin ($\mathbf{q} \cong 0$).
- The discrete character of Raman spectrum of a crystal is a direct consequence of the conservation of energy and crystal momentum.
- When the crystal momentum and the wave vector conservation restraint is relaxed (as it should be for a disordered crystal or an amorphous solid) the entire energy spectrum of vibrational excitations becomes accessible to the light scattering.
- Main types of disorder in crystalline solids: point defects (impurities), dislocations, grains (nonstructured systems).
- In these cases the Raman spectrum of the system consists of broad bands rather than of sharp lines, which reproduces the vibrational density of states projected at the centre (Γ -point) of the first Brillouin zone.
 ω
- Spectral effects of topological disorder on the Raman scattering from solids: the case of amorphous silicon.
- Hereafter some examples from:
 - covalent crystals (Ge, Si and C-diamond);
 - molecular crystals (sapphire);
 - disordered crystals (beta-alumina).
 - amorphous solids and glasses.

DISPERSION CURVES OF SILICON (001) AND RAMAN SPECTRUM OF α -Si









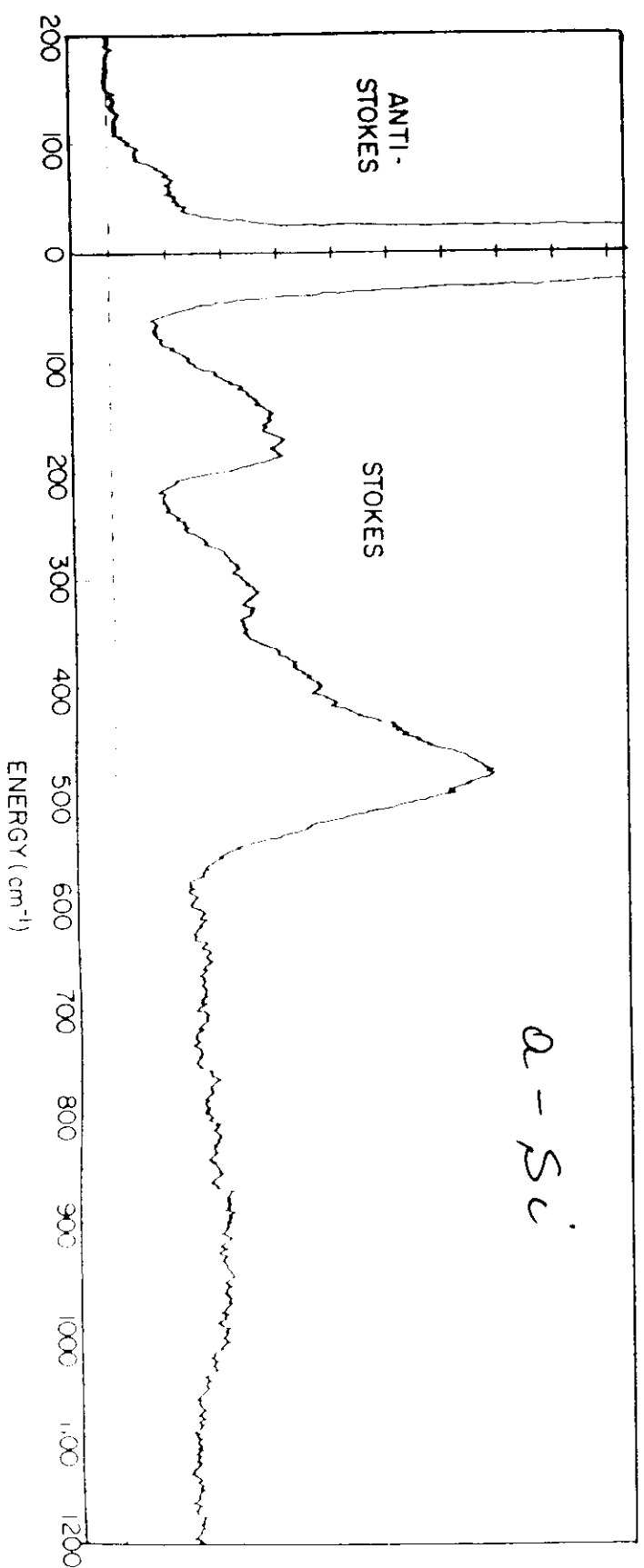
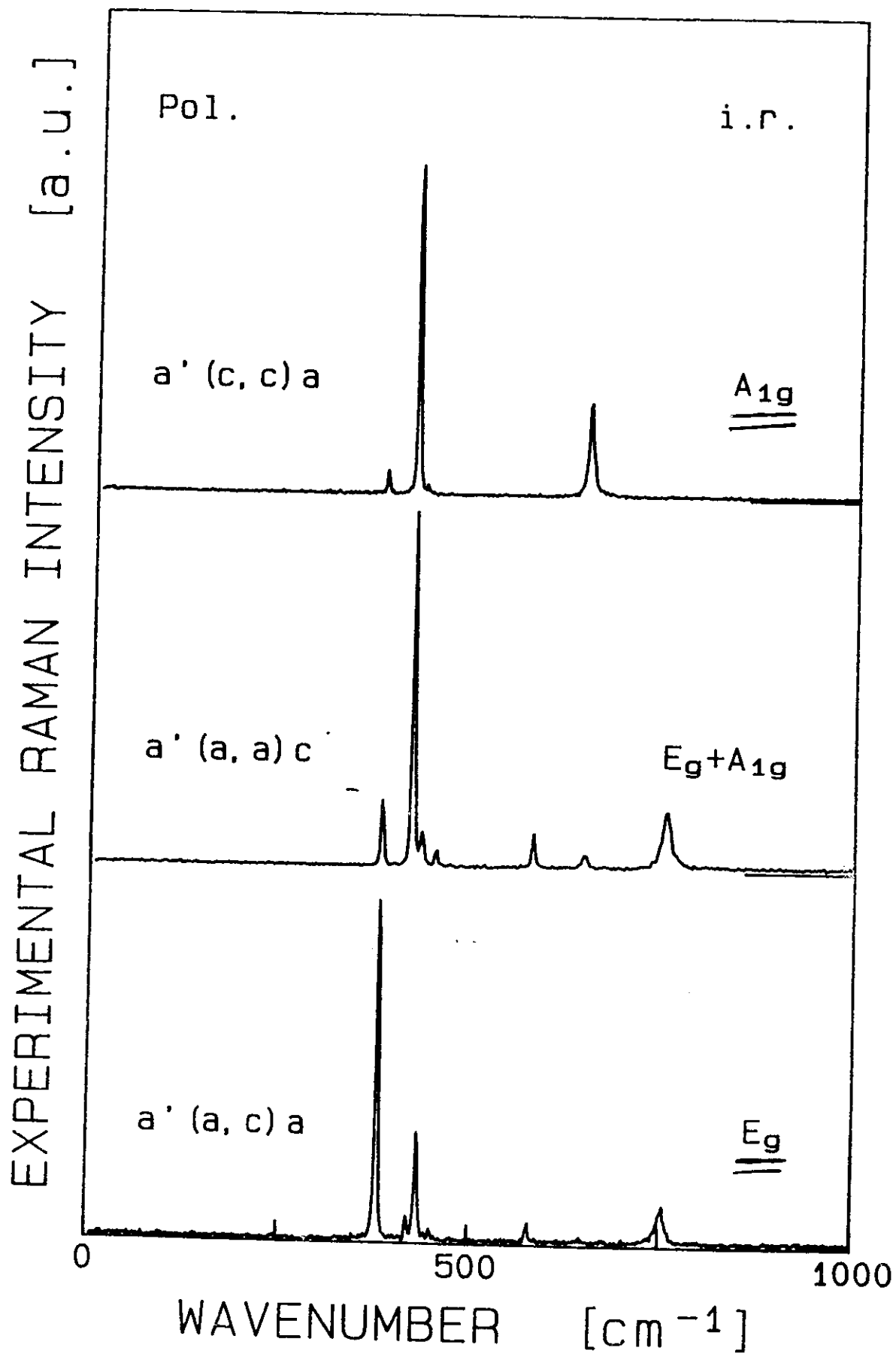


FIG. 1. Raman spectrum of amorphous Si at 27 K. The material was prepared by high-energy ion bombardment. Instrumental resolution is 10 cm⁻¹. The spectrum was excited by 0.24 W of 488-nm light and the measured peak height at 480 cm⁻¹ is 35 photons/sec (Ref. 21).

VIRGIN CRYSTAL

α - Al_2O_3

$T = 293 \text{ K}$



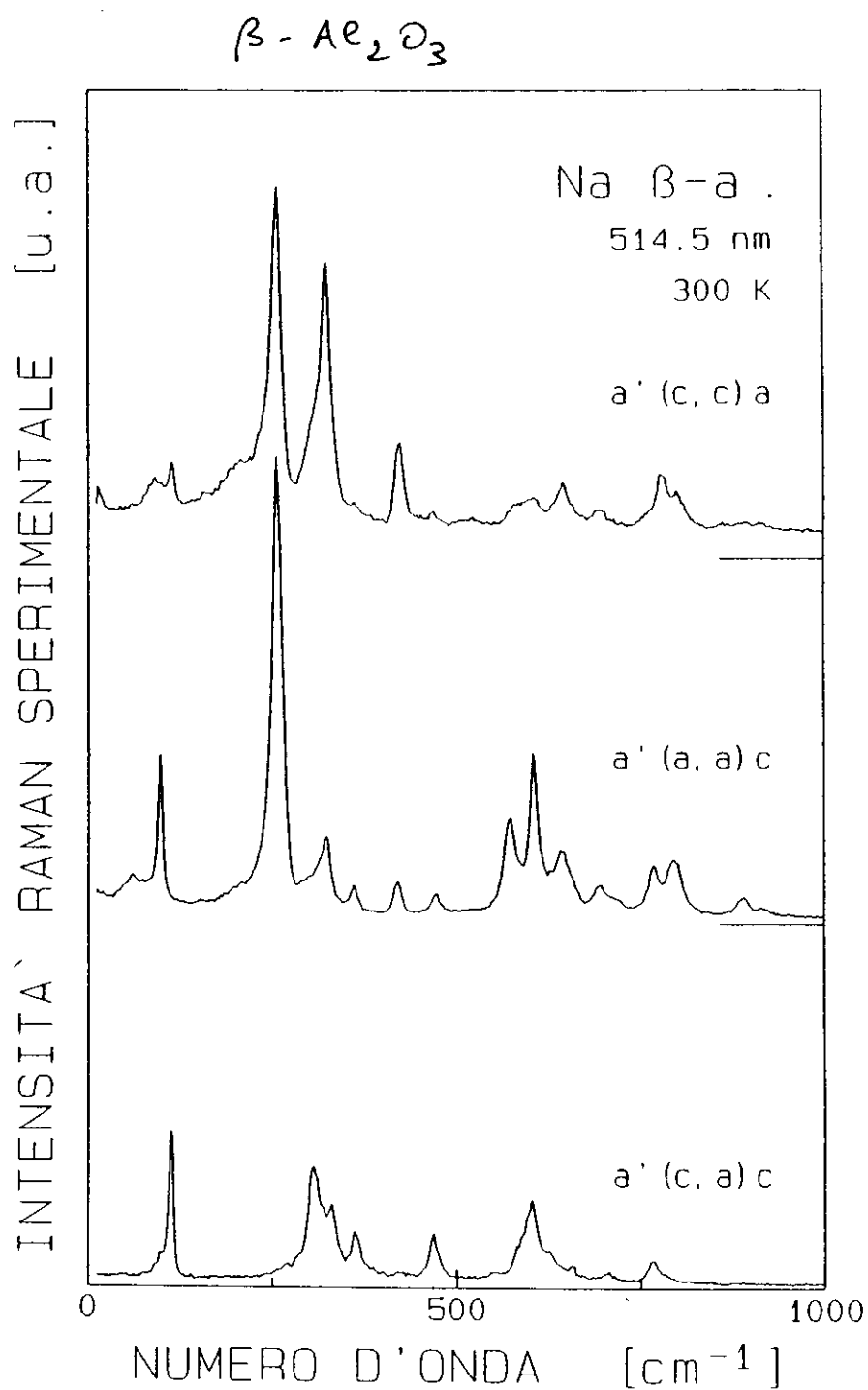
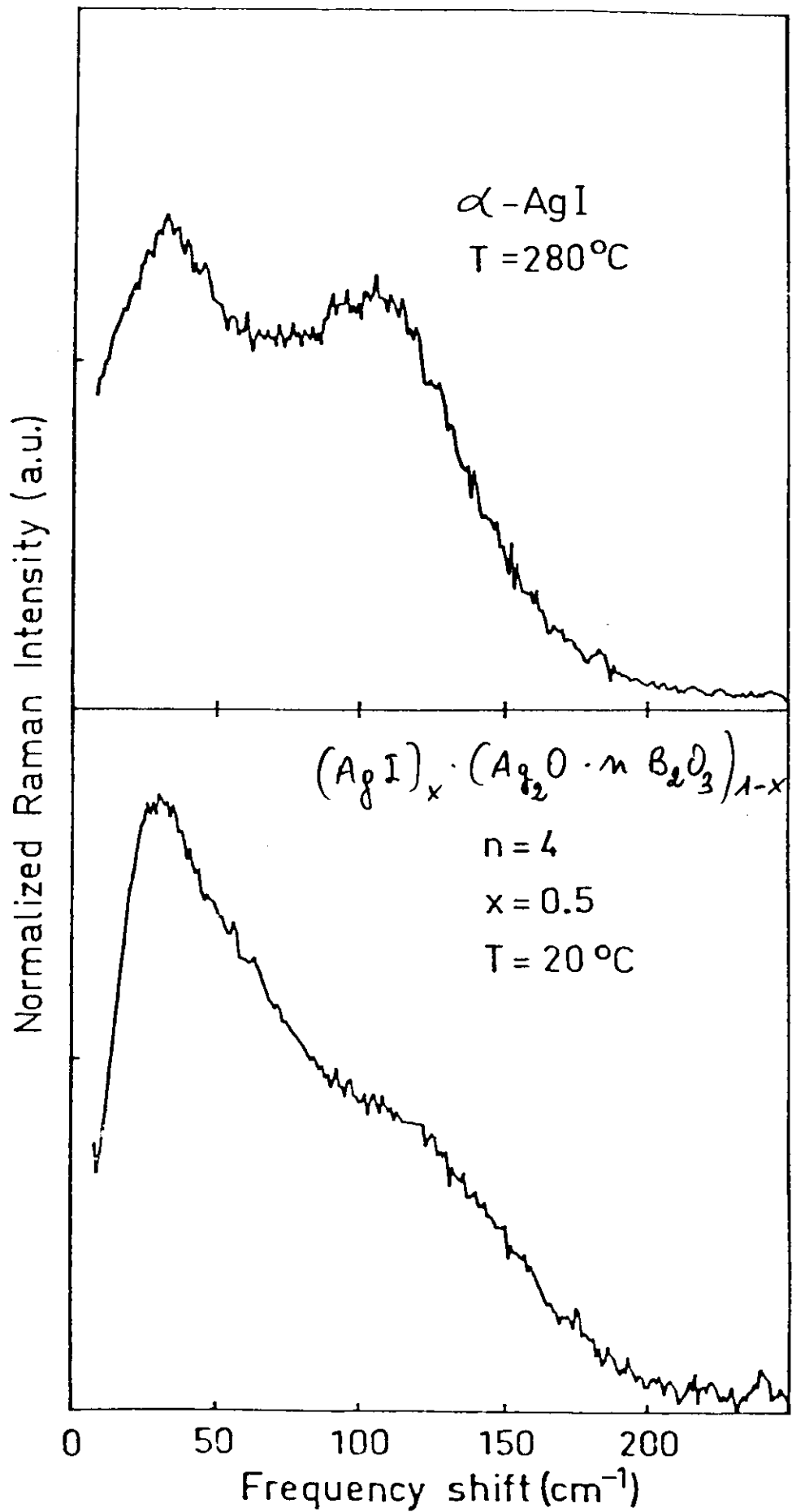
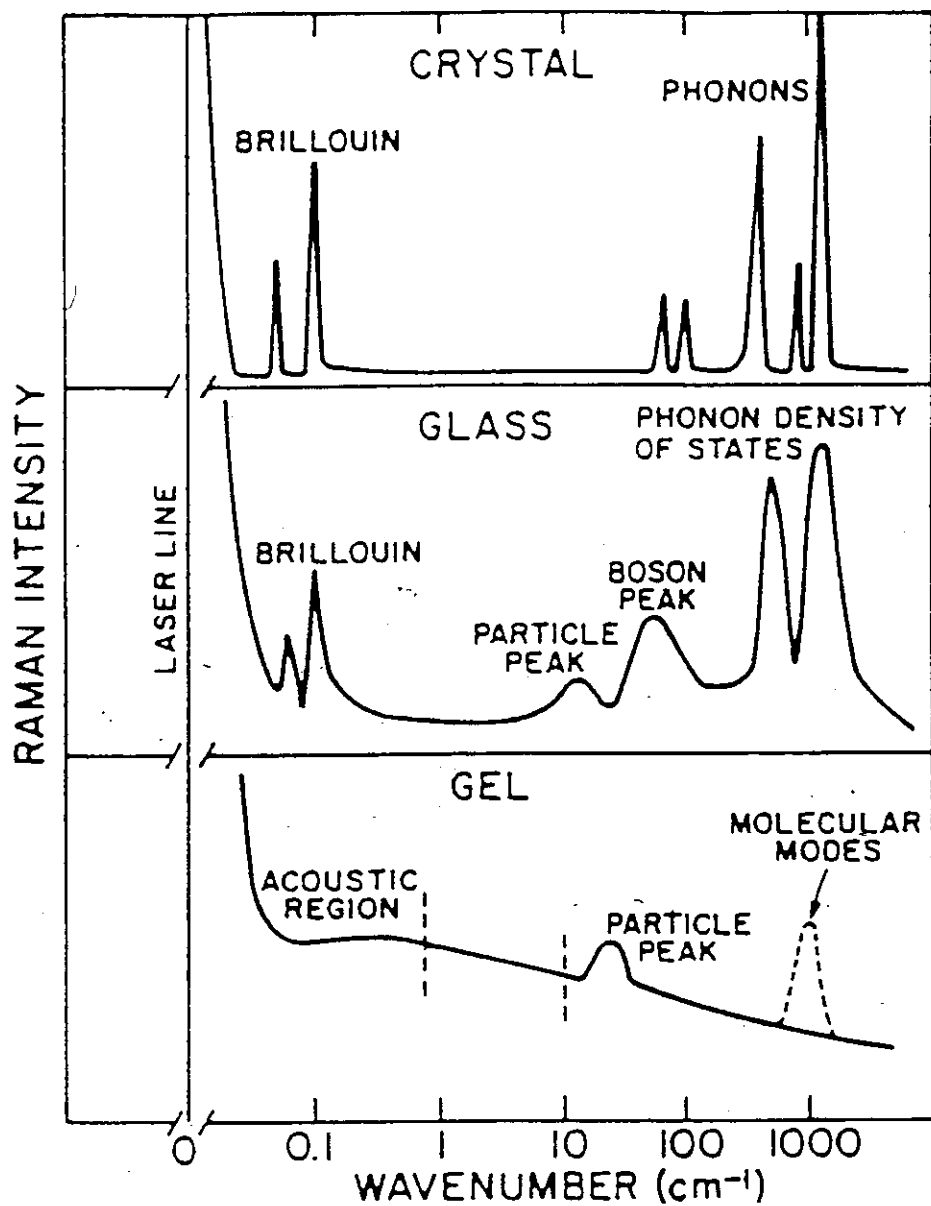


Figura C.2: Spettri Raman per la sodio β -allumina nelle tre polarizzazioni atte ad individuare la simmetria dei modi.

$$\bar{E}_{\text{exc}} = 632.8 \text{ nm}$$





Sketch comparing Raman spectrum of well-ordered crystal with that of a glass and a gel.

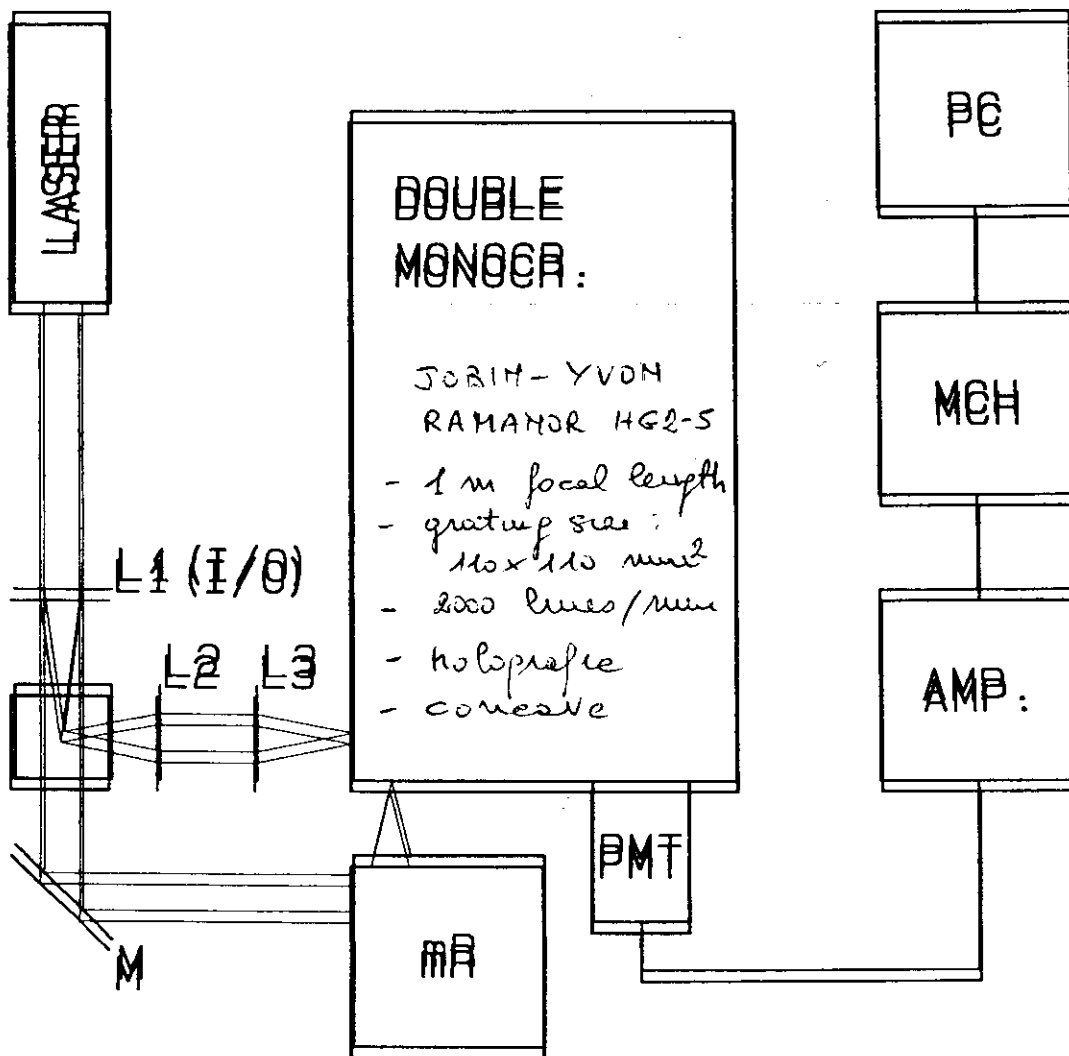
SOME EXPERIMENTAL CONSIDERATIONS

- Raman scattering is a two-photons process:
Typical scattering efficiency : $\sim 10^{-7} \div 10^{-10}$
- The scattered radiation is not easily detectable: need of sophisticated detection systems: PMT (photon counting), and CCD arrays (intensified).

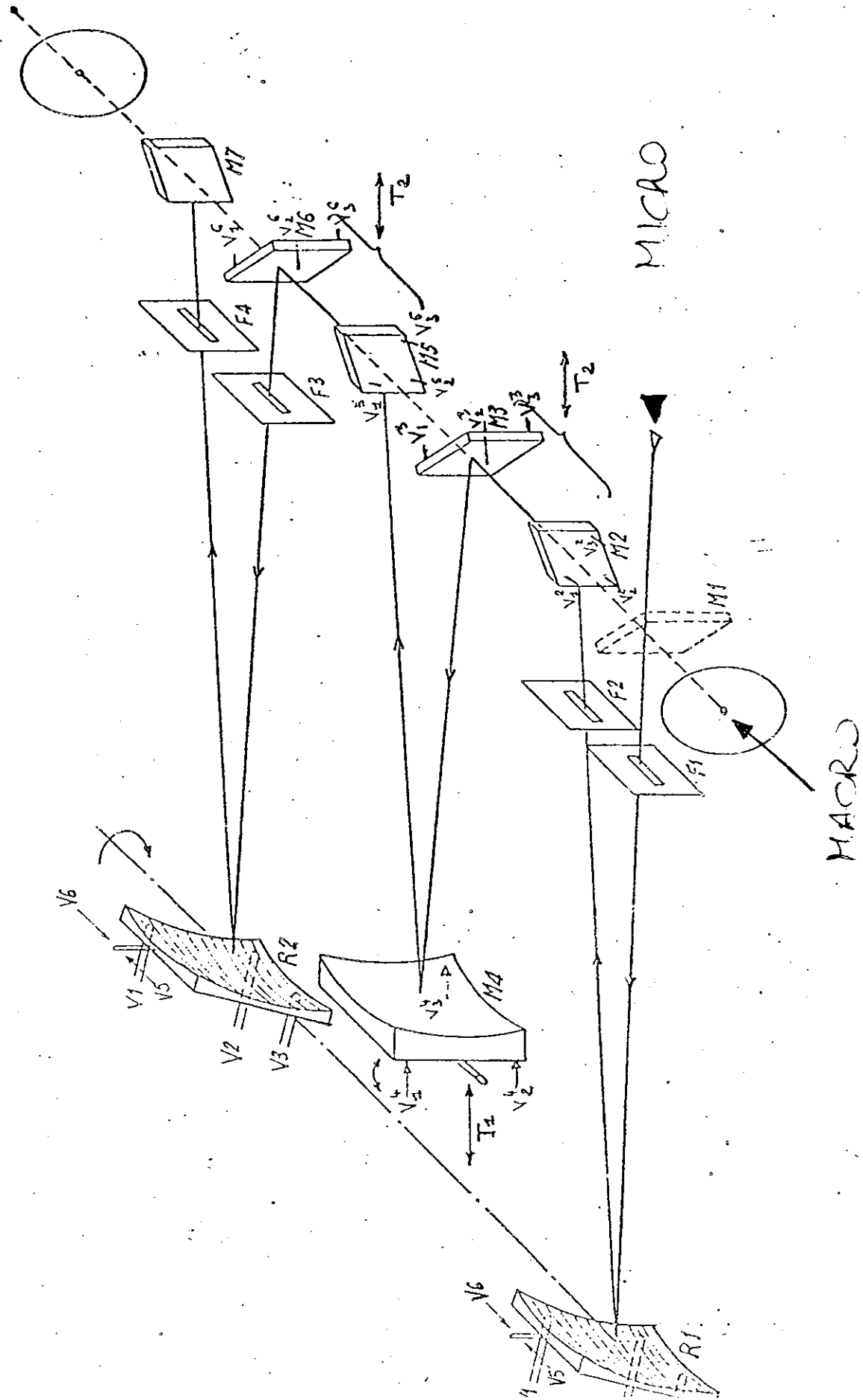
Expected values for a typical experiment on solids:

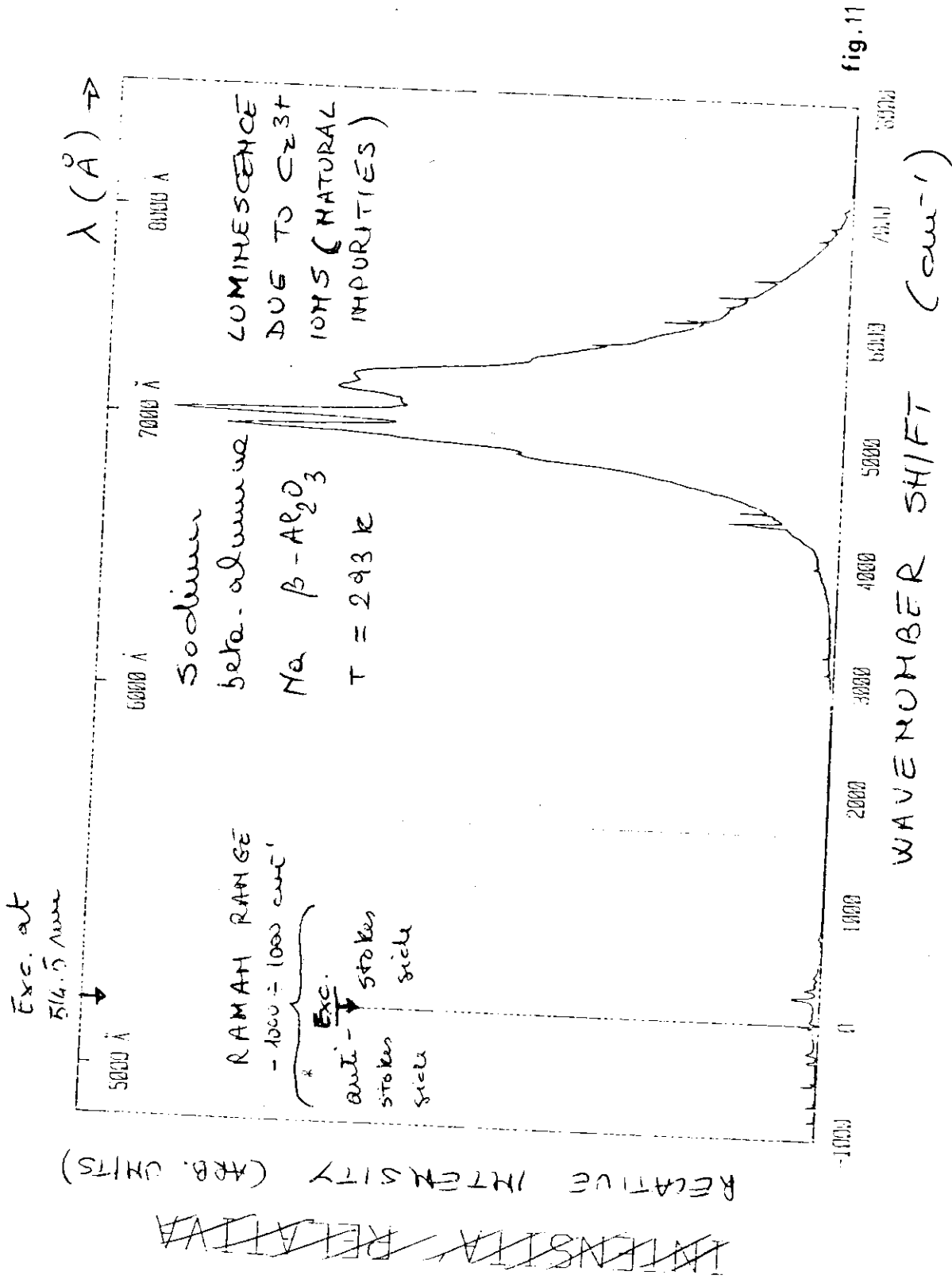
- Number of incident photons : $\sim 3 \times 10^{17}$ quanta/s (i.e: the power of 100 mW of a laser beam operated at 600 nm).
- Number of photons entering into a collecting lens: $\sim 10^9$ for a strong scatterer (but it may be equal to 10^6 for a poor scatterer)
- Transmission efficiency of spectrometer: $\sim 10\%$.
- Number of photons arriving to the PMT photocatode is: $\sim 10^6$ (for a strong scatterer), when the spectrometer resolution is set so that the instrument bandpass contains 1% of transmitted light.
- Assuming a photocatode's quantum efficiency of $\sim 10\%$ and a PMT gain of $\sim 10^6$, we get a current signal of $\sim 10^{-8}$ A ($\approx 10^{11}$ electrons/second).
- Typical dark current : $\sim 10^{-11}$ A, which correspond to 10^2 pulses/second. Cooled PMT show dark currents of $\sim 10^{-13}$ A (i.e.: few pulses/second).
- In the case of strong scatterers Raman signal can be recorded in **current detection mode**, and PMT cooling is not mandatory to obtain good signal-to-noise ratios.
- • For very low levels of light (as in the case of poor scatterers) **Photon counting detection techniques** are required and the PMT must be cooled in order to obtain reasonable signal-to-noise ratios.

RAMAN APPARATUS OF TRENTO'S GROUP



OPTICAL LAYOUT OF DOUBLE-MONOCHROMATOR OF TRENTO'S GROUP





~~FREQUENZA (cm-1)~~

Raman Instrumentation: characteristics and evolution

Background

Hereafter a minimal explanation about the light scattering is given in the aim to aid understanding of the improvement in the Raman Spectroscopy instrumentation.

When a monochromatic light from a laser is allowed to strike a sample, almost all of the light is observed to be scattered elastically, with no change in energy or frequency (Rayleigh scattering).

A very small part, approximately 1 in 10^8 – 10^{10} , is scattered with a change in frequency (Raman scattering).

The difference between incident and scattered frequencies correspond to an excitation of the molecular system, most often an excitation of a vibrational mode.

By measuring the intensity of the scattered light as a function of the frequency difference, we obtain the Raman spectrum of the system.

Given to very low efficiency of this process, it is clear that detection of these scattered photons will require a high selectivity against the large number of elastically scattered photons at the incident laser frequency.

This is the first and most important problem in light scattering experiments on crystalline solids. In all type of Raman instrumentation we must find a way to eliminate or severely reduce the intensity arising from the elastically scattered radiation (Rayleigh scattering). This is obtained either by using high contrast double-monochromators, mounting holographically ruled gratings, or, recently, by using holographic «notch» filter, especially conceived to reject the elastically scattered light.

A second problem which often interfere with the detection of Raman scattered photons is the fluorescence, arising either from the material of interest or from impurities embedded in the sample. Given to low efficiency of the Raman scattering process, a very small amount of impurity can give rise to a fluorescence signal which completely obscure the Raman photons.

Much work has gone into various experimental techniques to avoid fluorescence: these techniques include either time-based discrimination (time-resolved Raman Spectroscopy), which exploit the different time-scale of the electronic (10^{-8} - 10^{-6} s) and vibrational (10^{-12} s) processes or red or near infrared excitation (Fourier Transform Raman Spectroscopy). This last provides the most successful approach to avoid the electronic absorption process that leads to fluorescence, since sample excitation occur in the IR or in NIR.

Without entering into the technical aspects of FT-Raman spectroscopy, here we shall focus on the historical evolution of «dispersive» Raman spectroscopy.

Dispersive Raman Spectroscopy

Dispersive Raman spectroscopy is the historically original technique since the observation of the first Raman spectrum, but, during the last decades, has largely benefited from technological advances in light sources (lamps, lasers), filters, spectrometers (prisms, monochromators, with holographically ruled gratings) and light detectors (photographic plates, photomultiplier tubes, and CCD arrays).

History

Since RS has historically used visible light as the exciting frequency, the main advances in the technique came from the improvements on light sources and light detectors in the visible region of the spectrum.

When first observed by Raman in 1928 and for several years thereafter, the techniques was carried out using high intensity mercury lamps as light sources and photographic plates as light detector.

In the 1960s mercury lamps were replaced by gas laser sources and photographic emulsion by photomultiplier tubes.

The strength of the elastic (Rayleigh) scattering from the samples and the sensitivity of the PMT led the need for double or triple-monochromators. These effectively rejected the Rayleigh line so that the inelastic (Raman) scattering (which is a factor 10^8 - 10^{10} less intense) could be observed.

At the end of 1980's FT-Raman spectrometers were introduced using near-infrared laser excitation and a Fourier transform spectrometer, configured for the NIR, for the frequency analysis of the Raman signal. The rejection of the Rayleigh line was carried out by the use of «notch» filters, which rapidly became the method preferred over monochromators.

In fact, holographic notch filters join a high rejection of the exciting frequency with a high throughput of the Raman scattered light. Used in Raman spectroscopy these notch filters often eliminate the need for double or triple monochromators whose only purpose was to remove the intense Rayleigh scattering. With such filter, only a single monochromator is needed to disperse the spectrum, with consequently large gains in optical throughput and signal-to noise ratio.

Lasers

Advances in laser technology have contributed significantly to the increased utility of Raman spectroscopy. There are now many laser lines available from various lasers for uses in Raman instrumentation. Most of these systems are cw in nature.

The visible region of the spectrum is still covered quite effectively by the discrete line output of either argon- or krypton-ion laser, as well as the various dye lasers.

Spectrometers

From the prism spectrographs (used by Raman in his experiments) to double or triple-monochromators, equipped with holographic gratings.

Our double-monochromator (Jobin-Yvon, model Ramanor HG.2S is equipped with concave holographically ruled gratings with 2000 lines/mm).

Technical features:

Focal length: 1 m, F/8 aperture, grating size: 110x110 mm²

Two beam entrance apertures: lateral and axial entrances.

Two beam exit apertures with detector attachment

Slits: Straight and horizontal, length 20 mm, width up to 2 mm, with definition 1 μ m, each slit being operated by stepping motor.

Spectral performances (for visible version):

Spectral range: 440 - 800 nm (22720 - 12500 cm⁻¹)

Dispersion 2.5 Å/mm - 100 μ m slit width corresponds to 1 cm⁻¹ at 500 nm

Stray light rejection: 10^{-14} at 20 cm⁻¹ far of the Rayleigh line.

Resolution: Better than 0.5 cm⁻¹ at 514.5 nm

Advantages and disadvantages of double and triple monochromators

The main advantages of using dispersive systems in Raman spectroscopy derive from their high spectral resolution and their extraordinary efficiency in the rejection of the Rayleigh line, which allow to scan Raman spectrum down to few cm^{-1} far from the excitation energy. This is sometimes a mandatory requirement, especially for light scattering experiments from localized acoustic phonons in nanostructured compounds (superlattices and quantum dots).

One of the major limitation of dispersive systems for Raman spectroscopy has been the throughput of the monochromators. The need of double or triple monochromators arose from the requirement for Rayleigh line rejection. A single monochromator has a stray light level that is too high to use in Raman spectroscopy when Rayleigh scattering can be eight to ten order of magnitude stronger than Raman scattered intensity. Double or triple monochromators provide sufficient stray light rejection to cope this problem. Unfortunately using double or triple gratings systems results in 1-5% transmission efficiency because of the reflection losses and grating efficiencies.

Recent major advances in Raman instrumentation

Notch filters: The inconvenients (low efficiency) arising from the use of double or triple monochromators can be overcome by inserting a holographic notch filter at the entrance slit of a single grating monochromator, which removes the Rayleigh scattered light, so that a single grating system is now quite usable for Raman scattering. The major advantage of such a system is the very high efficiency, since there are now as few as two reflecting surfaces and only one grating. The throughput can approach 50%. An additional advantage is the reduced size of the instrument (which can be of only one-fourth the size of the double or triple monochromator). But unfortunately notch filter approach is not useful for experimental investigation of the very low-frequency Raman scattering region, down to few cm^{-1} far from the Rayleigh line.

Array detectors: Another major advance in RS has been in the area of array detectors. Recent detector technology has moved forward once again in parallel with what happening in photography. The most sensitive detector for visible light (and increasingly for near-infrared light) is the Charge Coupled Device (CCD), similar to the detector found in the modern camcorder. This consists of an array of detector elements (pixel), typically 1000×1000 pixels in size. This solid state silicon device produces electrons when photons illuminate a depletion layer with efficiencies of typically 50%, but which can be higher than 80%. The accumulated electron charge is the «read out» from the device. For critical detector applications, their sensitivity is enhanced by reading out the charge at relatively slow rates compared with camcorder. But, by far the greatest increase in signal-to-noise ratio is gained by cooling the CCD detector. The dark current, which can be thought of as detector noise, is of the order of 50000 electron per second per detector element (pixel) at room temperature but falls dramatically as the temperature is reduced to a less than 0.05 electron per second per pixel when at -40 C. This means that the cooled CCD is a detector which can literally detect a few tens of photons over an area of one or two square centimeters.

Advantages and disadvantages of CCD arrays in dispersive RS

The grating disperses the spectrum in a stripe across the CCD so that all Raman shifted frequencies are measured simultaneously. This gives much faster acquisition times than a conventional scanning instrument, but until now this has restricted either the resolution or the spectral range of such instruments.

Laser confocal Raman microspectrometry

P. Dhamelincourt^{*1}, J. Barbillat¹ and M. Delhay²

¹LASIR, UPR 2631L, CNRS, Université de Lille I, F-59655 Villeneuve d'Ascq Cedex, France.

²DILOR, 244 ter rue des Bois Blancs, F-59000 Lille, France.

^{*}Author to whom correspondence should be addressed.

Introduction

From the time of its discovery in 1928 until 20 years ago, Raman scattering has been used for studying macroscopic bulk samples and furnishing information about fundamental molecular properties, providing an important tool in the spectroscopy laboratory. Raman spectroscopy is based on the spectral distribution of inelastically scattered light and is a highly-selective technique for investigating molecular species in all phases of matter, as they are fingerprinted by their vibrational spectra. The introduction of lasers as sources has greatly enhanced the potential of Raman spectroscopy for microanalysis. Indeed Raman scattering can provide information which previously was not available from any other widely used techniques such as electron, ion and Auger microprobes. These last techniques can readily identify, map out the distribution and determine the quantity of elemental constituents present but do not readily distinguish the chemical forms of polyatomic species present as specific compounds in a sample. With lasers as sources for excitation of Raman scattering and the continuing development of instrumentation for optical spectroscopy, Raman microspectrometry has now matured to the point at which non-destructive chemical microanalysis and mapping has become routinely practicable for both research and industrial purposes. In this paper, recent development and applications in confocal Raman microspectrometry are described.

Principles of Raman spectroscopy

Spectroscopic measurements done with Raman spectrometers are mainly based on the excitation and detection of the normal (spontaneous) Raman effect, which has been fully described.¹ The effect is an inelastic scattering process

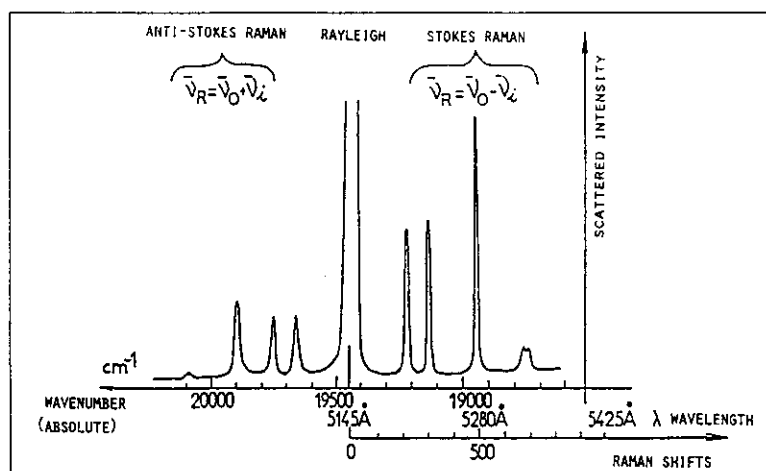


Figure 1. Schematic representation of a Raman spectrum excited with the green line of an argon ion laser, $\lambda_0 = 514.5$ nm.

observed in the near UV/visible to near infrared spectral region, which involves the interaction of a monochromatic beam of light with the molecules of the sample. This interaction produces scattered radiation at different frequencies. These frequency shifts (from the exciting line) are identified with the frequencies of the atom oscillations in polyatomic structures contained in the sample. A schematic representation of a Raman spectrum is presented Figure 1. Excitation with the green line (514.5 nm) of an argon ion laser is assumed. The Stokes Raman lines ($\tilde{\nu}_0 - \tilde{\nu}_i$) and the corresponding weaker anti-Stokes lines ($\tilde{\nu}_0 + \tilde{\nu}_i$) appear symmetrically on both sides of the strong Rayleigh line ($\tilde{\nu}_0$). In this representation, $\tilde{\nu}_0$ and $\tilde{\nu}_i$ are the absolute wave numbers ($\tilde{\nu} = \nu/c$) expressed in cm^{-1} of the exciting line and of the Raman lines respectively. The Raman shifts $\tilde{\nu}_R$, are read directly on the Raman spectrum recording, which usually consists only of the more intense Stokes part. The intensities of the lines are determined by the Raman cross-section (see below) and are directly proportional to the number of molecules which are probed. The kind of information provided by the Raman spectrum is essen-

tially the same that is obtained from infrared spectra. Thus, Raman spectra can be regarded as unique fingerprints which also contains information on the local molecular environment (e.g. amorphous or crystalline phases). In the spontaneous Raman effect described above, the incident photon energy is below the energies of any excited electronic levels. But if the exciting wavelength is such that the incident photon energy approaches or is equivalent to these levels, then other inelastic processes such as resonant Raman scattering² and fluorescence³ may be induced. The fluorescence emission which is often an order of magnitude or more greater than the Raman scattering may sometimes mask the Raman emission.

Confocal laser Raman microspectrometry Instrumentation

The intensity of the signal delivered by the detector of a spectrometer analysing a given Raman line at the wavelength λ can be expressed by:

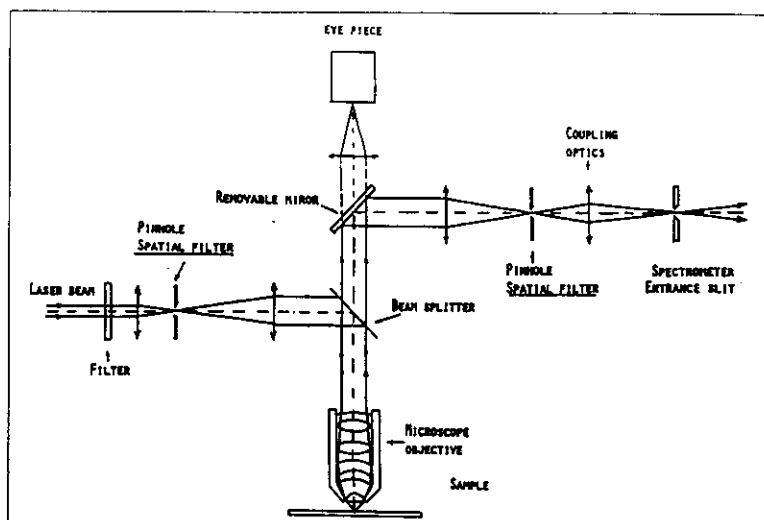


Figure 2. Optical scheme of the illuminating and collecting optics of a micro-Raman spectrometer.

$$S \sim I_0 \sigma_{\lambda} N \Omega T_{\lambda} s_{\lambda}$$

where I_0 is the laser irradiance at the sample (watts unit area⁻¹), σ_{λ} is the differential cross-section for the Raman line analysed (cm² . sterad⁻¹ . molecule⁻¹), N is the number of molecules in the probed volume V , Ω is the solid angle of collection of the Raman light and T_{λ} and s_{λ} are the throughput of the instrument and the sensitivity of the detector at the wavelength λ , respectively. When a small volume of matter has to be examined, there are only a few parameters which can be modified in order to compensate for the large reduction in the number of molecules N in the probed volume V , namely I_0 and Ω . In fact, the probed volume and the solid angle of collection are not independent and extensive work at the LASIR, several years ago, was devoted to explore techniques for developing micro-Raman instruments.^{4,5} From experience gained in this work, it was concluded, that the use of microscope objectives for

both illuminating the sample and collecting the Raman light was the best way to decrease V while increasing Ω and I_0 . Indeed, microscope objectives which are high-numerical aperture (NA) optics are able to focus the laser beam into a very small volume and to collect, under a wide angle, the light scattered by this volume. Thus, both the enormous increase of the local irradiance I_0 and the wide angle of collection Ω compensate for the decrease of the number of molecules N . A micro-Raman instrument possesses a good quality light microscope coupled to a spectrograph (or spectrometer). This optical coupling must be optimised from the sample to the photoelectric detector via the collection optics and the spectrograph and/or the spectrometer. A schematic diagram of the widely adopted laser focusing, sample viewing and scattered light collection geometry is represented in Figure 2. It can be seen, from this figure, that a micro-Raman spec-

trometer was conceived, at its origin, as a confocal microscope. In fact, a real confocal configuration requires a very accurate optical alignment and a high degree of stability and reproducibility of the mechanical and optical alignment.

Confocal Raman microscopy

In a confocal microscope,⁶ the laser beam is filtered by an illumination pinhole. This initial spatial filtering removes unwanted rings and noise and produces a clean point source waist which is imaged on to the sample (at the object plane of the microscope objective) (Figure 3). The Raman light scattered by the sample is directed to an adjustable pinhole placed in the image plane of the microscope objective. The pinhole used for the filtering of the laser beam (illumination pinhole D_1) and the one used for transmitting the Raman light to coupling optics and spectrometer (adjustable pinhole D_2) are the "confocal diaphragms". They are optically conjugated with the point source in the object plane. This arrangement ensures that only light coming from the focal plane entirely reaches the detector while that coming from upper and lower planes is partially attenuated. This accounts for the confocal micro-Raman spectrometer's ability to discriminate between parts of the sample which are not at the same depth allowing "optical sectioning". In Figure 3, the intensity distribution has been represented as a function of the altitude Z of the object plane. This shows that the axial resolving power, which is defined as the full-width at half-maximum (FWHM) of the curve, for a confocal microscope is increased compared to that of a conventional microscope. The confocal configuration is especially valuable in Raman spectrometry since it almost eliminates stray light (background, fluorescence) coming from outside the focal volume. Decreasing the size of the spectrometer "confocal diaphragm" improves the axial resolution and stray light rejection. The use of an adjustable size spectrometer "confocal diaphragm" allows a variable confocal effect and thus an optimum adjustment of the recording conditions to the sample geometry.

Raman imaging

Micrographic images revealing the spatial distribution of a given molecular species within a sample can be produced by isolating with a filter a narrow spectral bandpass centred on a characteristic Raman wavenumber of this compound

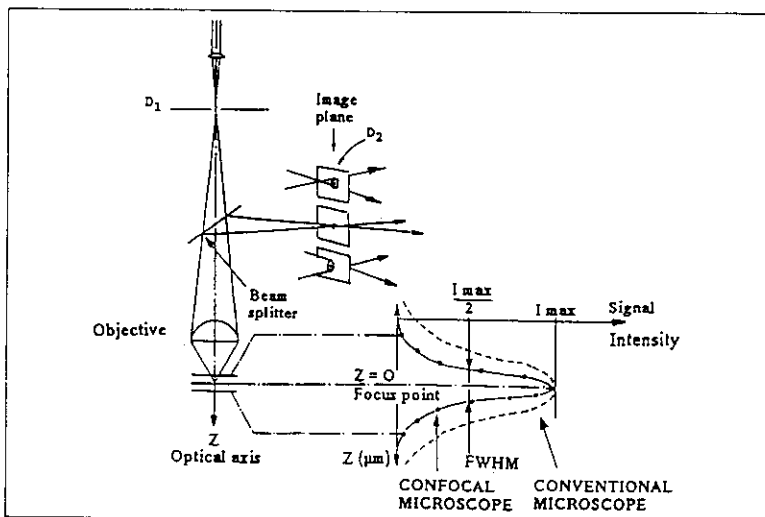


Figure 3. Principle of confocal microscopy.

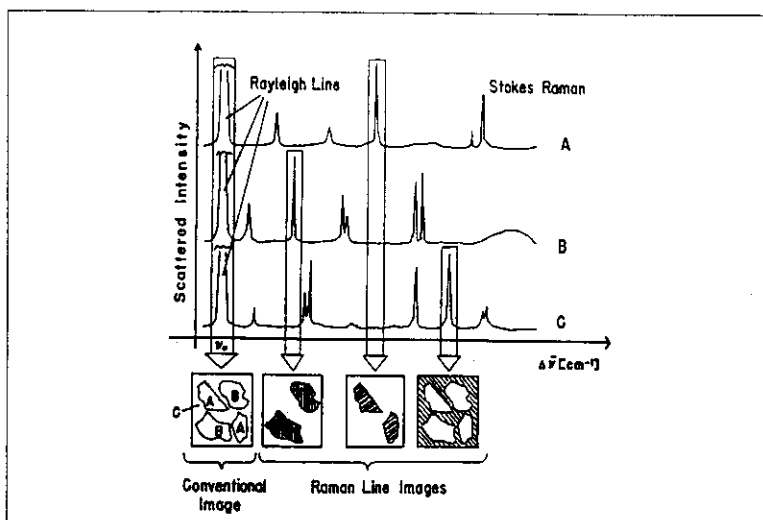


Figure 4. Principle of Raman imaging.

(Figure 4). This is the basic principle of Raman microscopy pioneered 20 years ago by some of us and demonstrated, for the first time, with the MOLE microprobe.⁷ Since then, Raman imaging has matured and now incorporates the latest development in confocal microscopy which provides the spectroscopist with the most efficient technique for Raman microprobing and Raman mapping with

a spatial resolution close to the diffraction limit. Various techniques of Raman imaging have been proposed which differ by sample laser illumination (global, point and line) and detector configuration (PMT, linear or 2D multichannel detector).⁸⁻¹¹ Two of these are worth emphasising: global illumination and the recently introduced confocal line illumination, both using 2D.

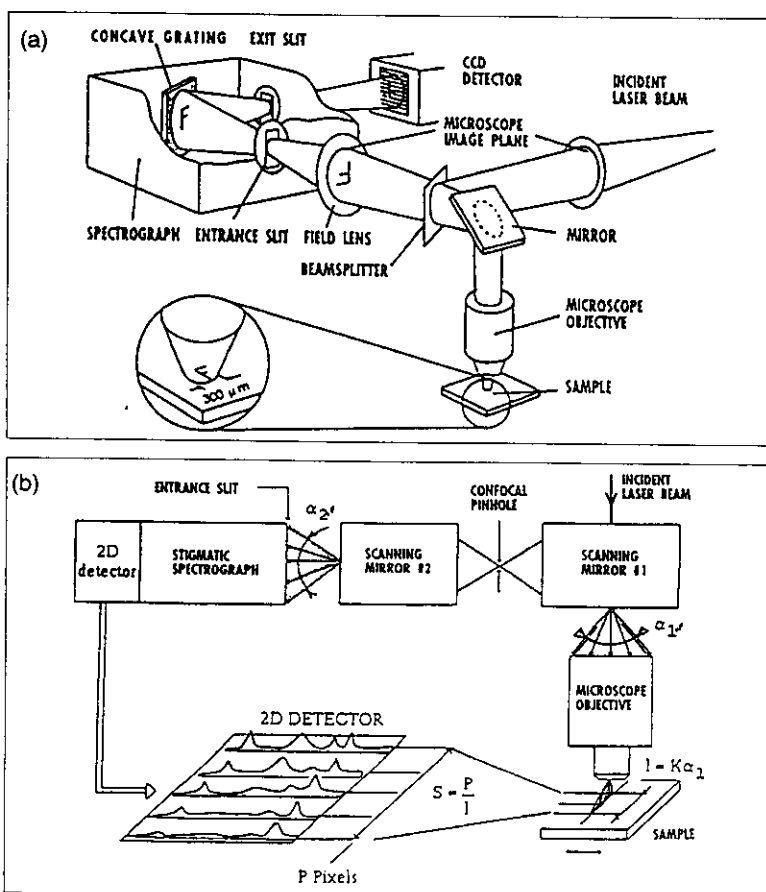


Figure 5. (a) Raman microscopy with global illumination; (b) Principle of confocal line illumination technique.

Global illumination

This technique has been employed in the first Raman microprobe (MOLE) and is the only way which allows direct real-time imaging. A large area of the sample is illuminated by the laser beam. A filter (grating monochromator or optical filter), tuned to a characteristic Raman line of one component of the sample transmits a monochromatic enlarged image of this to a 2D detector [Figure 5 (a)]. Lateral and axial resolution of the Raman microscope are defined by the microscope objective but cannot benefit from the confocal arrangement. Indeed, since the exit pupil of the microscope objective is optically conjugated to the slits of the monochromator, this arrangement necessitates wide slit openings so as not to impair the resolution of the microscope. This requirement has two important consequences: low spectral resolution and poor stray light rejection which have strongly limited the applications of the MOLE. However, new designs integrating low noise CCD detectors and high performance optical filters have already improved the field of direct Raman microscopy.^{12,13}

Confocal line illumination

The line illumination technique allows a better use of a two-dimensional array detector (CCD for instance) since both spectral and spatial information can be obtained simultaneously: data along the slit are related to the spatial distribution of molecular species within the illuminated line of the sample and data perpendicular to the slit are related to spectral information. We have recently designed and patented a special optical device based on line illumination that preserves all the advantages of confocal Raman microscopy.¹⁴ Unlike "basic" line illumination, the confocal line scanning technique is a two-step process which involves two successive beam deflections¹⁵ [Figure 5 (b)]. A first scanner deflects the laser beam at the entrance of the microscope objective and produces a narrow line on to the sample (Figure 6). The same scanner also steers towards the spectrometer the Raman light scattered by the sample along the illuminated region. As a consequence, whatever the position of the laser spot on the sample, an enlarged image of the probed area may be focused on to an adjustable pinhole acting as a spatial filter (as previously described above). The second scanner (synchronous with the first one) deflects the light passing through the confocal aperture so that at each point of the sample corresponds a point of the entrance slit of the spectrometer. Linear

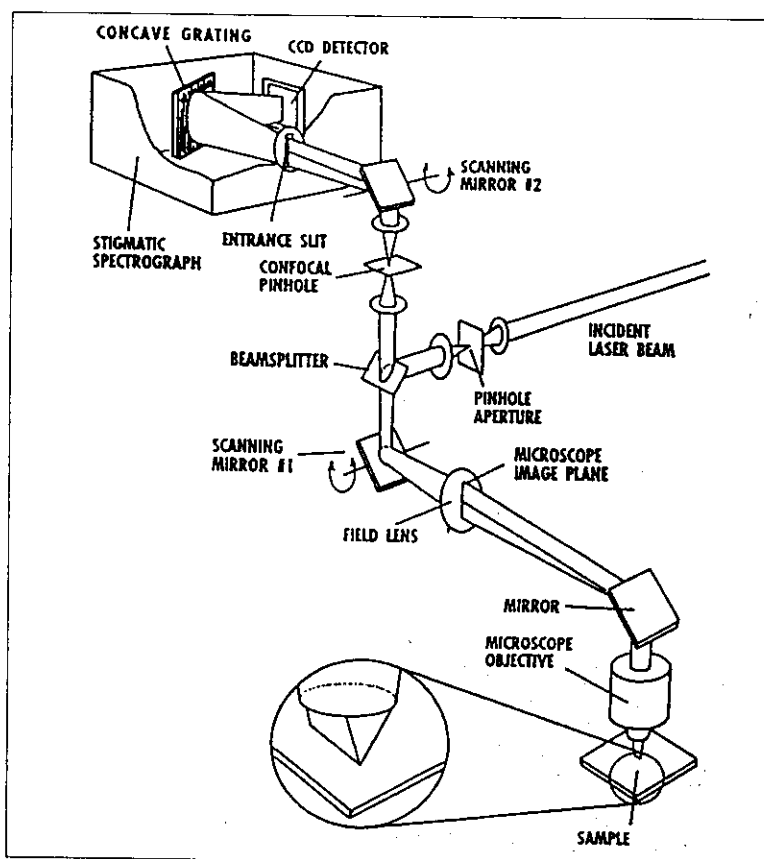


Figure 6. Optical scheme of the confocal line illumination device.

intensity distributions (line profiles) at many Raman wavenumbers are collected simultaneously by the 2D detector placed in the focal plane of the stigmatic spectrometer. Raman images at chosen Raman wavenumbers can be built up by moving the sample stepwise in a direction perpendicular to the laser line. This

configuration benefits from the main advantages of confocal microscopy given above (i.e. improved axial and lateral resolution, sectioning capability). It also possesses an integrated zoom capability which results from the two-fold beam deflection. By using different motion amplitudes for the two scanners it is

possible to change continuously the "spread factor" defined as the ratio of the number of illuminated pixels of the CCD (along the slit direction) over the length (expressed in μm) of the laser line onto the sample. A low spread factor can be used for a survey examination of the sample while a larger value will be preferred to map out a small region of the sample with more detail. Since the two scanners can be driven separately although remaining synchronised several modes of operation are available:

- Fixed mirrors enable the system to work like a conventional confocal Raman microspectrometer.
- Sample degradation of fragile material can be avoided by scanning the laser beam on to the sample while concentrating all the signal on to a single point of the slit.
- Evolution of a sample versus various physical parameters (temperature, pressure etc.) can be followed by focusing the laser beam on to a fixed point of the sample and by deflecting the scattered light along the slit.

Illustrations of Raman images are shown in Figure 7 (a) and (b).

Applications of micro-Raman spectrometry

Many kinds of problem can be investigated by micro-Raman spectrometry.

We give here some of the more common examples of the application.

Geology and gemmology

In the course of geological phenomena, whether they be hydrothermal, magmatic or metamorphic, the role played by fluids is very important. Studies of the composition and density of deep fluids, i.e. the intramineral inclusions whose sizes vary from a few to several tens of μm , can therefore provide sound proof of the origin of the minerals. Thus it is very important to examine each inclusion individually and non-destructively. Confocal Raman microspectrometry, through its capacity to examine a very small volume *in situ* (through the host mineral), is particularly well adapted to the study of fluid inclusions. It provides precise data for identification and determination of molar fractions of the main geological fluids (CH_4 , CO_2 , N_2 , H_2S , O_2 , H_2 , for example). The coupling of microthermometry with micro-Raman spectrometry allows a correct definition of the thermobarometric conditions of the fluid capture.^{16,17}

In a similar manner, micro-Raman spectrometry has proven to be an excellent technique for identifying fluid or solid inclusions in gems. Provided that the host gem is transparent, the laser beam can be focused directly through a crystalline or a cut facet (without any removal from the setting of the jewel) into the inclusion to be characterised. For the gemmologist, this identification is of the utmost importance not only for identification of gems and determination of their geological origin but also for discriminating between natural gems and the synthetic ones now, more and more, produced for jewellery (e.g. sapphire, ruby, emerald).¹⁸

Industrial material control

Contamination and the formation of defects are problems constantly encountered in the commercial production of materials. The chemical identification of these defects is of particular interest because it can lead to properly selected materials and processes. In semiconductor production, for example, because circuit-board geometries and components approach μm dimensions, contaminants

of this size often create reliability problems. The first step towards solving these problems is identification of the contaminant, for which micro-Raman spectrometry is often the only method with a chance of success.¹⁹ Inorganic but mainly organic (e.g. contaminants from etching or from packing materials) can be readily identified *in situ*. In addition to the identification of foreign contaminants on devices, micro-Raman spectrometry can also provide characterisation of the materials used in fabricating these devices. For example, with the development of large-scale integration (VLSI) technology, considerable emphasis has been placed on devising methods of fabricating high-quality silicon films on a variety of insulating substrates (e.g. vapour-phase epitaxy, thermal annealing). A good understanding of the crystal growth is essential for developing materials of correct quality. The Raman technique is often used as a rapid non-destructive method for processed silicon based on the position of the silicon band around 520 cm^{-1} which is very sensitive to local lattice characteristics. A further example is the control of stress distribution around devices since stress can exceed the plastic deformation and reduce the production yield. Still based on the shift of the 520 cm^{-1} band, compressive or tensile stress can be evaluated and this parameter be plotted as a function of the position. VLSI array transistors have recently been so examined.²⁰

In situ analysis of ancient works of art

Historical materials and works of art are unique and cannot be replaced; no risk of damage from the analysis can be tolerated. Micro-Raman spectrometry is well suited to authentication, as it causes no major damage to the historic item or *objet d'art* being examined. Work in this laboratory²¹ has demonstrated the ability of this technique to identify pigments on various ancient works of art. For example, Lazurite and mercury(II) sulphide (Cinabar, natural vermilion) were identified in the blue and red ornamented letters on a page of a twelfth century missal. Recent identification of pigments on mediaeval manuscripts has also been reported.²²

Microanalysis of biological tissues and cells

With the advent of the Raman probe, possibilities for molecular investigations appear to be opening in biology, pathology and tissue research at the cellular level. So far, because of the fragility of biological samples, studies have been mainly restricted to problems where the

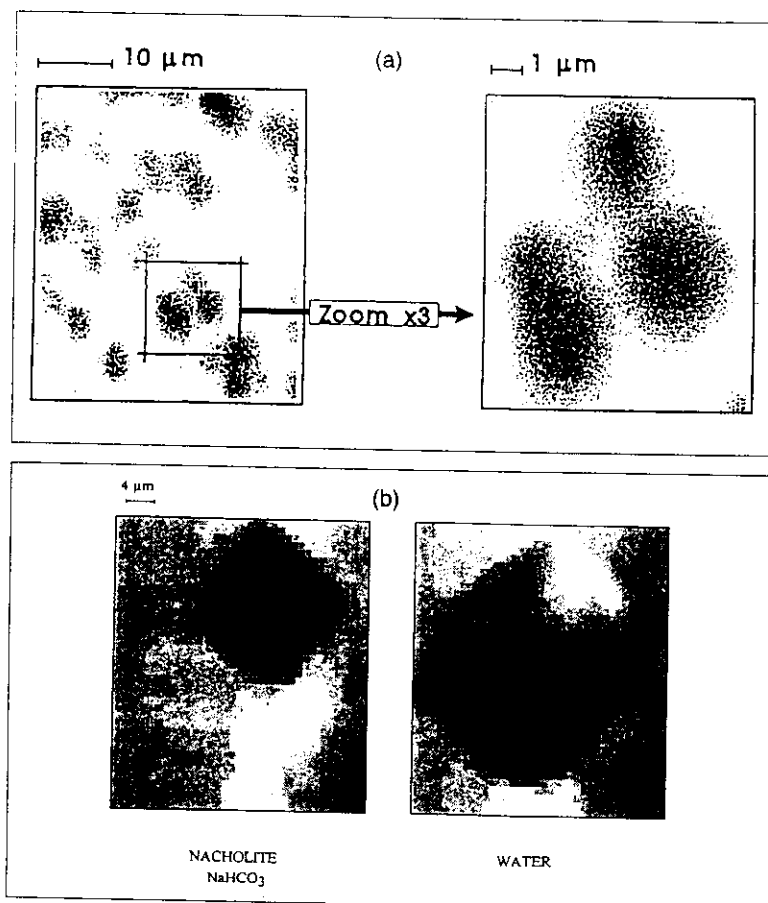


Figure 7. (a) Raman images of synthetic diamond microcrystals; (b) Raman images of the distribution of Nacholite and Water in a multiphase inclusion inside host quartz.

sample was sufficiently locally concentrated (i.e. bio-accumulations in cells and tissues, hard tissue formation, foreign bodies in tissue coming from the degradation of implanted prostheses etc.).²³ *In vivo* studies of pigments in vegetal and animal single cells are also directly possible²⁴ by using the resonance Raman effect or SERS (Surface Enhance Raman Spectroscopy).²⁵ Recently, studies of the interaction of an anti-tumour agent RP 6045 with DNA in living cells have been reported.²⁶ By using the SERS effect, spectra of the anti-tumour agent in the cytoplasm and the nucleus of a single K 562 cancer living cell were recorded. They gave important information on the mechanism of the action of this anti-tumour agent.

Conclusion

With routine detection limits in the range and high molecular selectivity, micro-Raman spectrometry has now become a major micro analytical technique for both research and industrial applications. Confocal Raman imaging has recently enhanced the capability of this technique to produce chemical maps at given depths inside a transparent sample.

Acknowledgement

Confocal Raman images were acquired and treated by using a special software program developed by S. Charonov who works with Professor M. Manfait, director of the "Laboratoire de Spectroscopie Biomoléculaire", Université de Reims, Faculté de Pharmacie, 51 rue Cognacq Jay, F-51096 Reims, France.

References

- D.A. Long, *Raman Spectroscopy*, McGraw-Hill, New York (1977).
- S.A. Asher, *Analytical Chemistry* **65**, 59A (1977).
- M. Salmon and P. Viallet, *Innov. Tech. Biol. Med.* **2**, 35 (1981).
- M. Delhay and P. Dhamelincourt, *J. Raman Spectrosc.* **3**, 33 (1975).
- P. Dhamelincourt, *Doctoral Thesis*, Université de Lille I (1979).
- T. Wilson and C. Sheppard, *Theory and Practice of Scanning Optical Microscopy*, Academic Press (1984).
- P. Dhamelincourt, F. Wallart, M. Lelercq, A. T. N'Guyen and D. O. Landon, *Anal. Chem.* **51**, 414A (1979).
- D.K. Weirs, V.K.F. Chia and G.M. Rosenblatt, *Appl. Optics* **26**, 50 (1987).
- D.J. Gardiner, C.J. Littleton and M. Bowden, *Appl. Spectrosc.* **42**, 15 (1988).
- M. Bowden, D.J. Gardiner and G. Rice, *J. Raman Spectrosc.* **21**, 37 (1990).
- K.L.K. Liu, L.H. Chen, R.S. Cheng and M.D. Morris, *Appl. Spectrosc.* **45**, 1717 (1991).
- D.N. Batchelder, B.J.E. Smith, S. Webster and C. Chang, in *Proceedings of 27th Annual Meeting of MAS*, Ed. by G. W. Bailey, San Francisco Press, San Francisco (1992).
- P.J. Treado, I.W. Levin and E.N. Lewis, *Appl. Spectrosc.* **46**, 1211 (1992).
- M. Delhay, E. Da Silva and J. Barbillat, *European Patent NO 92400141.5* (1992).
- J. Barbillat, E. Da Silva, M. Delhay, P. Dhamelincourt, M. Manfait and B. Roussel, *Proceedings XIIIth ICORS*, Ed. by W. Kiefer, John Wiley & Sons, Chichester and New York, p. 1074 (1992).
- P. Dhamelincourt, J.M. Beny, J. Dubessy and B. Poty, *Bull. Mineral.* **102**, 600 (1979).
- N. Guilhaumou, P. Dhamelincourt, J.C. Touray and J. Tourret, *Geochim. and Cosmochim. Acta* **45**, 657 (1981).
- M.L. Delé, P. Dhamelincourt, J.P. Poirot and H.J. Schubnel, *J. Mol. Struct.* **143**, 135 (1986).
- Z. Muggli and M.E. Andersen, *Solid State Technol.* **4**, 287 (1985).
- W.J. Rothwell, C. Hell and P.J. Pearson, *Proceedings XIIIth ICORS*, Ed. by W. Kiefer, John Wiley & Sons, Chichester and New York, p. 1064 (1992).
- B. Guineau, C. Couprie, M.T. Gousset, J. P. Forgerit and J. Vezin, *Scriptorium* (1986).
- S.B. Best, R.J.H. Clark and R. Withnall, *Proceedings XIIIth ICORS*, Ed. by W. Kiefer, John Wiley & Sons, Chichester and New York, p. 1042 (1992).
- L. Abraham and E.S. Etz, *Science* **206**, 716 (1979).
- G.J. Puppels, F.E.M. De Mul, C. Otto, J. Greve, M. Robert-Nicoud, D.J. Arndt-Jovin and T.M. Jovin, *Nature* **347**, 301 (1990).
- B. Pettinger, *Phys. Chem.* **91**, 308 (1987).
- M. Manfait, J.F. Riou, H. Morjani, F. Lavelle and I.R. Nabiev, *Proceedings XIIIth ICORS*, Ed. by W. Kiefer, John Wiley & Sons, Chichester and New York, p. 520 (1992).

PART B :

APPLICATIONS OF RAMAN SPECTROSCOPY TO MANUFACTURED SYSTEMS

- B-1) MICRO-RAMAN SPECTROSCOPY
ON POROUS SILICON
- B-2) LOW-FREQUENCY RAMAN
SPECTROSCOPY ON SEMICONDUCTOR
AND METAL PARTICLES.

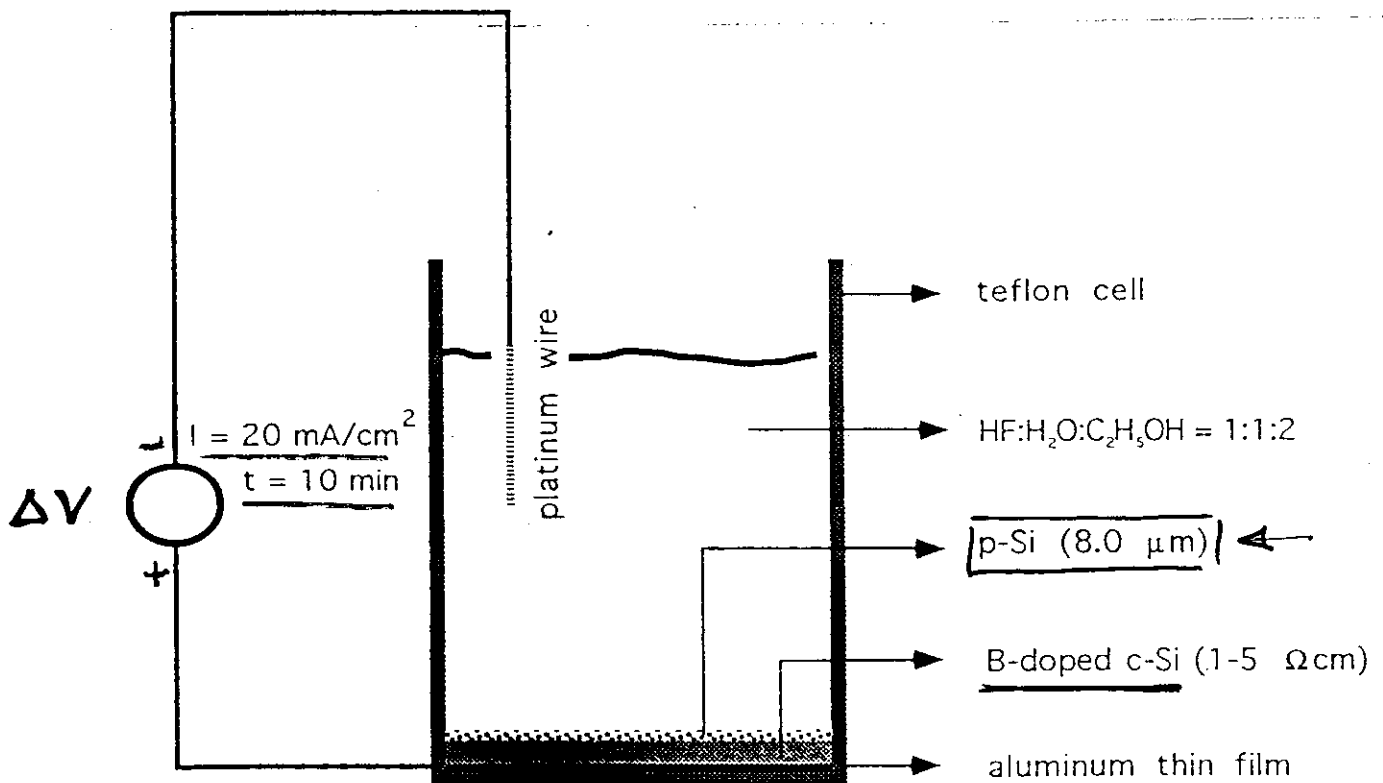
NANOSTRUCTURED SYSTEMS

- Nanostructured systems consisting either of semiconductor crystallites (quantum wires and dots) or of metal particles (clusters) dispersed in transparent dielectric matrices have attracted much interest during the last years due to their unusual optical, electrical and mechanical properties.
- The novel physical properties of these systems are due to anomalously high surface to volume ratios of nanostructures and to considerable shift of their energy levels caused by the quantum confinement, occurring when the dimensions of the crystallites are reduced to a size comparable to excitonic radius.
- The fundamental studies of nanostructured materials are currently aimed to probe the quantum confinement effects, either with respect to electrons or phonons.
- To this aim, many spectroscopic investigations have been carried out by means of electron and optical techniques, among them namely photoluminescence and Raman spectroscopy.
- Porous Silicon (p-Si) provides one of the most studied example of nanostructured systems, because it shows very strong confinement effects of both excitons and optical phonons.
- Since 1990 p-Si has been the target of intense experimental and theoretical investigations aimed to correlate its strong light emission at room temperature (in the visible region of spectrum) with its microstructural properties.
- As far as the technological aspects are considered, this system is expected to be well compatible with the existing technology of silicon, and therefore it seems finally possible to integrate on the same monolith both electronic and optoelectronic functions inside the same device.

B-1) : p-Si

SAMPLE PREPARATION

p-Si LAYERS BY ANODIC ETCH OF
DOPED c-Si WAFERS
IN HYDROFLUORIDRIC SOLUTIONS

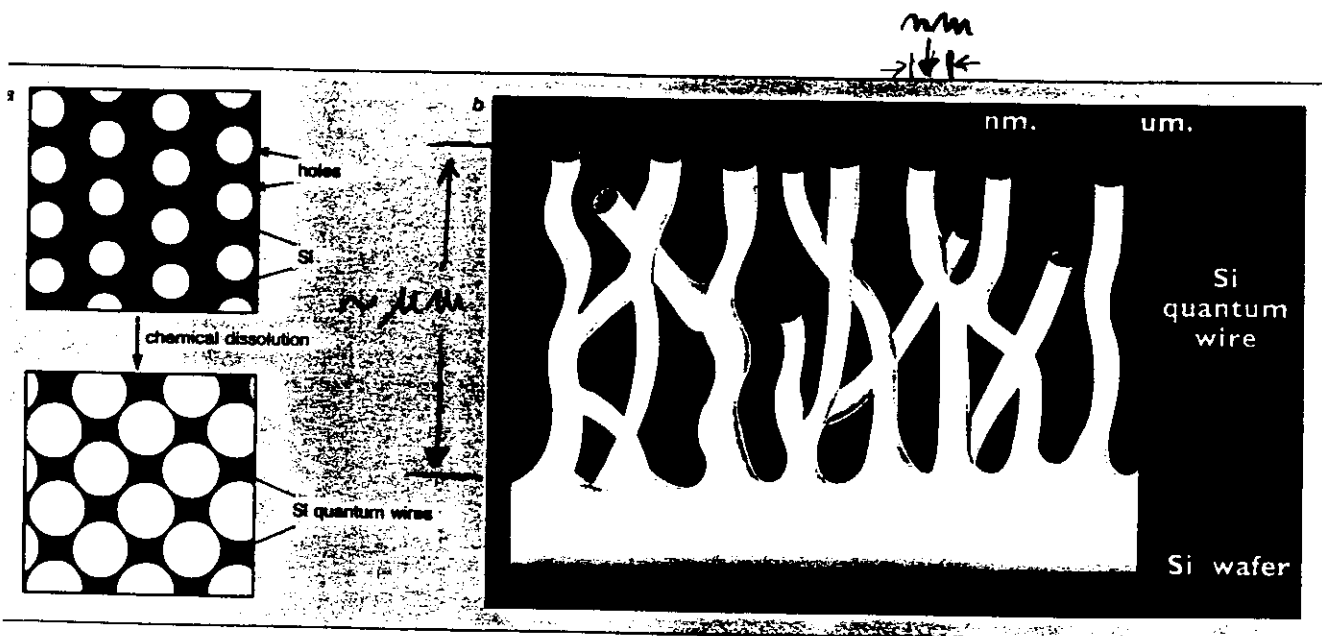


1 - ELECTROCHEMICAL EROSION

2 - CHEMICAL DISSOLUTION

Nanostructures of porous silicon produce multicolour luminescence by a mechanism that still defies explanation

Silicon optoelectronics t the end of the rainbow?

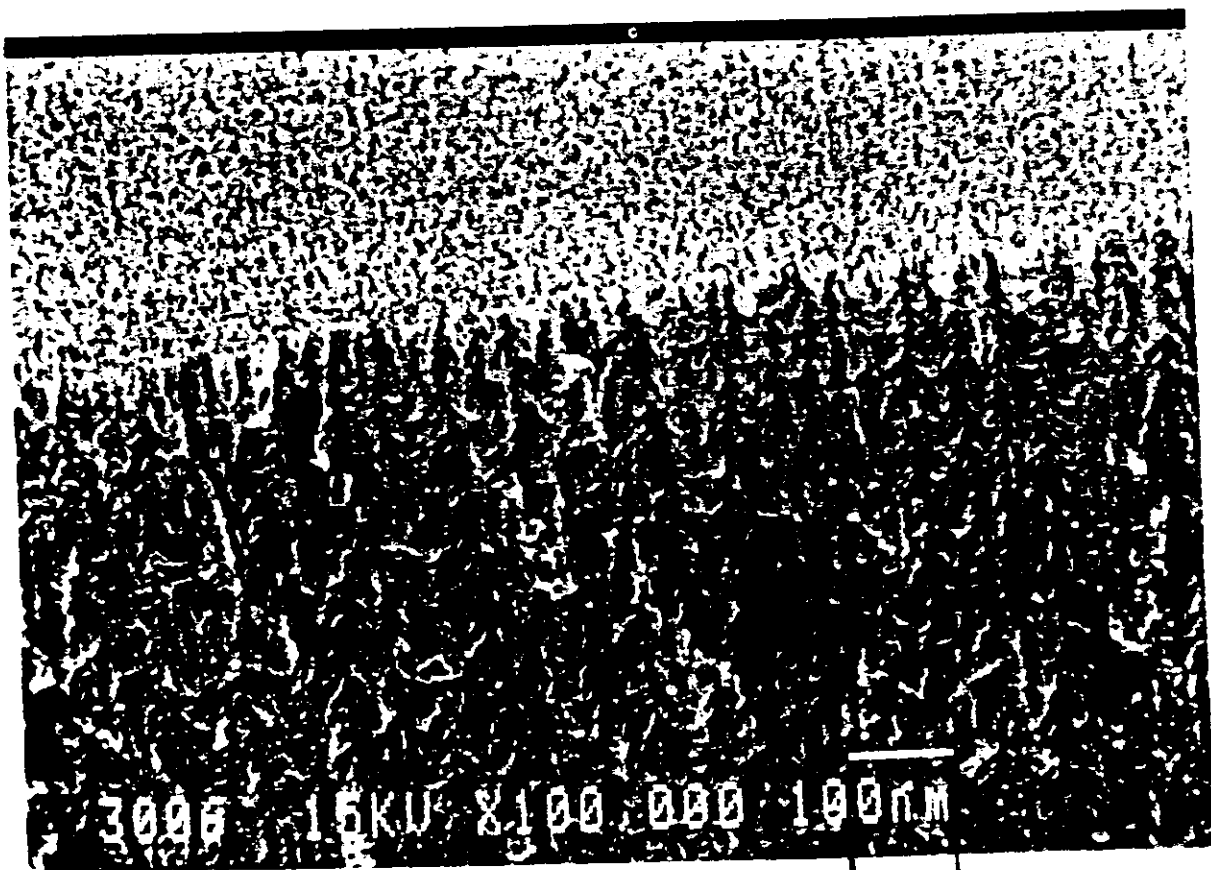


POROUS SILICON MICRO-STRUCTURE

ANALYTICAL ELECTRON MICROSCOPY

T.E.M. (LOW MAGNIFICATION) IMAGES OF
POROUS - SILICON

→ LOW-MAGNIFICATION STRUCTURE OF p-Si
SHOWS COLUMNAR AND RANDOMLY SPACED STRIATIONS



→
100 nm
←

p-Si : HISTORICAL BACKGROUND

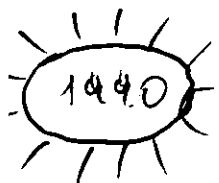
1956 : UHLIR (AT BELL LABS) DISCOVERS p-Si DURING HIS STUDIES ON ELECTROPOLISHING

1970s : WATANABE (AT NTT) USES p-Si AS A DIELECTRIC MATERIAL IN S.O.I. TECHNOLOGY FOR V.L.S.I. Si, AFTER DISCOVERING THAT p-Si FILMS WERE HIGHLY POROUS AND READILY OXIDIZED

THE EXPLORATION OF BOTH STRUCTURAL AND OPTICAL PROPERTIES OF p-Si OCCURS DURING THE 1980s.

1984 : PICKERING (U.K.) REPORTED THE FIRST OBSERVATION OF LOW-TEMPERATURE LUMINESCENCE FROM p-Si, AND CARRIED OUT SOME STRUCTURAL CHARACTERIZATION OF p-Si BUT HE DID NOT INVESTIGATE THE OPTICAL PROPERTIES OF p-Si AT ROOM-TEMPERATURE

MID 1980s : MICROSTRUCTURAL STUDIES OF p-Si



CANHAM OBSERVES EFFICIENT, VISIBLE LIGHT EMISSION AT ROOM-TEMPERATURE FROM FREE STANDING p-Si PILLARS (2-10 μm IN DIAMETER, $\sim 10 \mu\text{m}$ IN LENGTH)

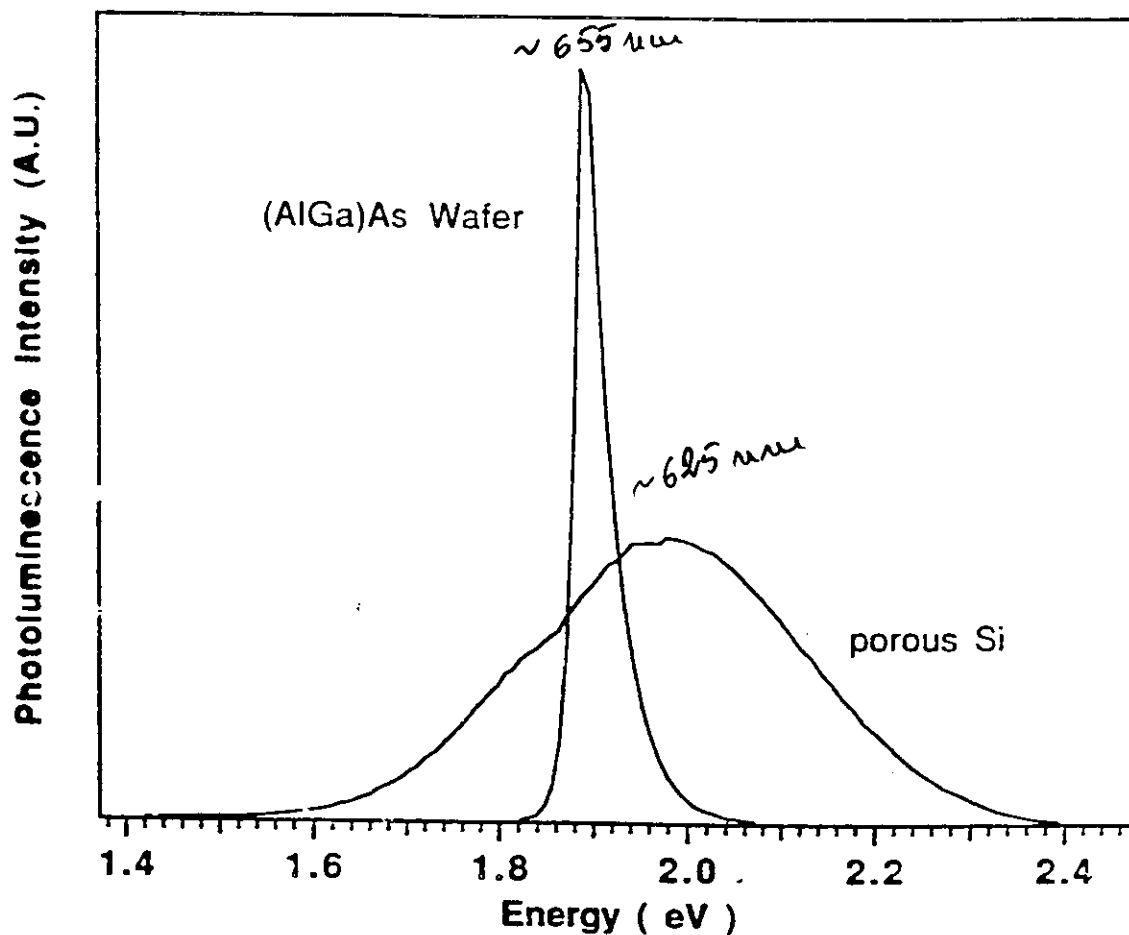


FIG. 1. Photoluminescence spectra from a visible-light-emitting porous Si specimen (sample No. 1) and a commercial (AlGa)As LED at room temperature under the same experimental conditions are shown for intensity comparison. The integrated intensity of the porous Si (sample No. 1) is 3 times stronger than that of the (AlGa)As LED.

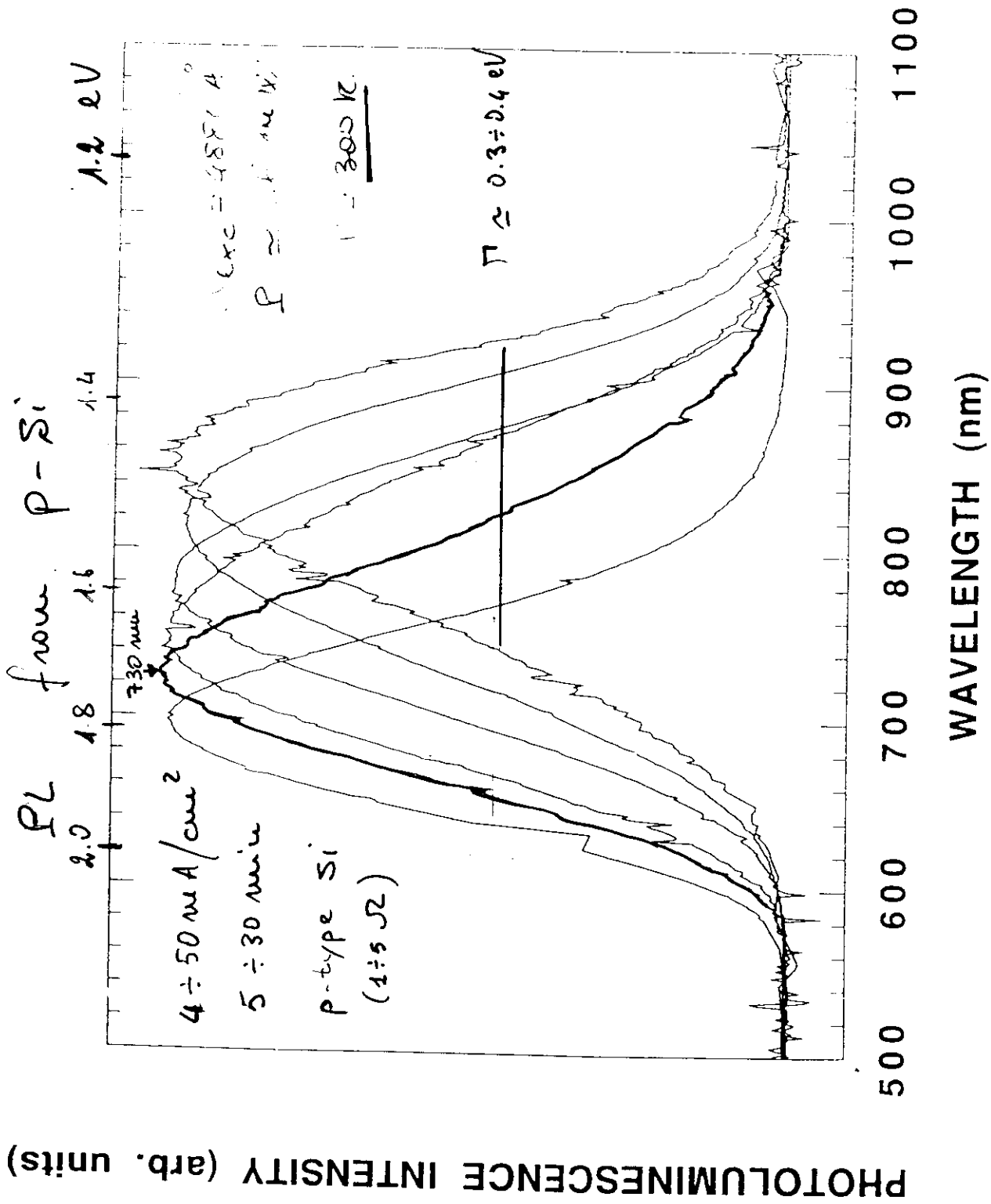
- OPTO-ELECTRONIC APPLICATIONS?
- UNRESOLVED PROBLEMS

p-Si : OPEN PROBLEMS

- QUANTUM CONFINEMENT
- PASSIVATION

THE DIVERSITY OF THE SAMPLES

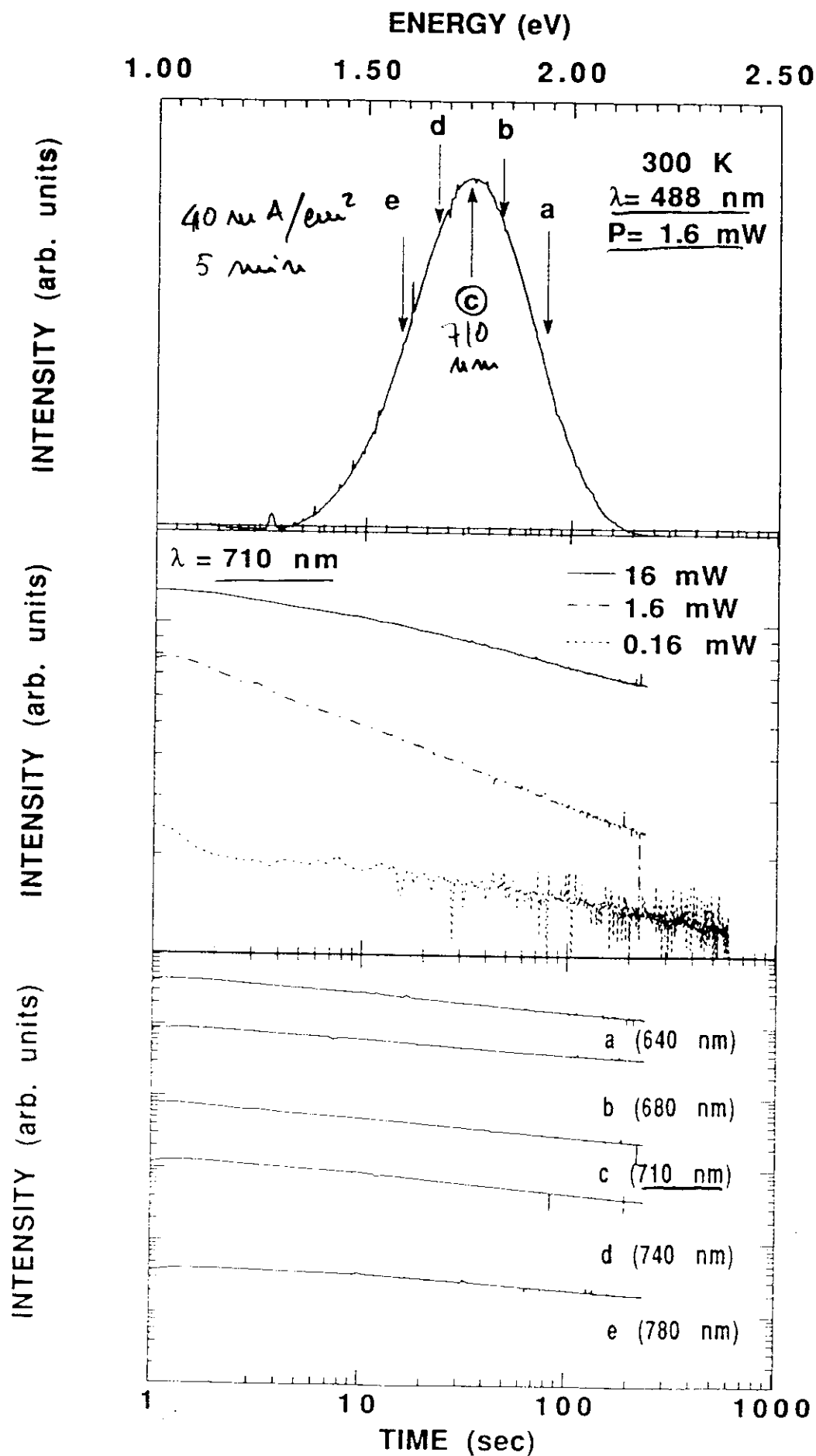
- FRESHLY ETCHED (H-PASSIVATED)
- AGED (O-PASSIVATED)



→ 0.6 μm PL ≈ 1 μm

PL - A p-Si

C-9



DEGRADO
DELLA PL

AGING!

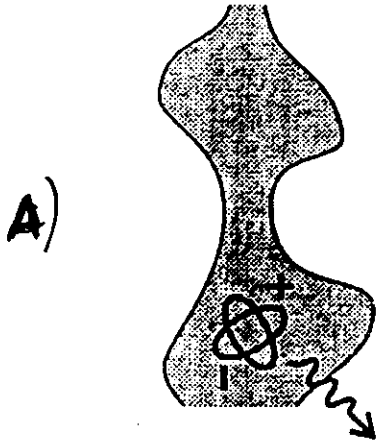
p-Si : SURFACE PASSIVATION

- ROLE OF DANGLING BONDS
 - NON-RADIATIVE DECAY CHANNELS
 - DETRIMENTAL EFFECTS ON THE PL
- H-PASSIVATION OF p-Si SURFACE
 - QUENCHING OF THE NON-RADIATIVE RECOMBINATION OF CARRIERS
 - BENEFICIAL EFFECTS ON THE PL

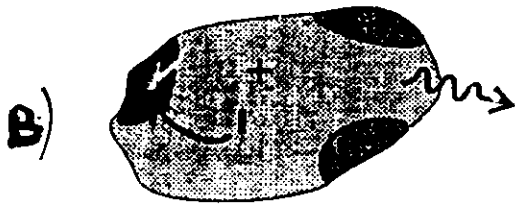
IF THE CARRIERS ARE CONFINED INTO A PERFECTLY PASSIVATED REGION, THEN THE NON-RADIATIVE TRANSITIONS ARE SUPPRESSED AND LUMINESCENCE TURNS OUT ENHANCED!

⇒ SURFACE CHARACTERIZATION OF p-Si LAYER IS A CRUCIAL STEP TO IMPROVE THE RADIATIVE QUANTUM EFFICIENCY TO LEVELS OF INTEREST FOR PRACTICAL APPLICATIONS (LED)

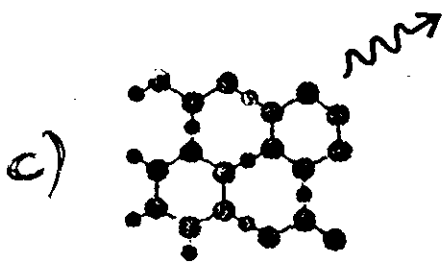
PHOTOLUMINESCENCE IN p-Si: MODELS



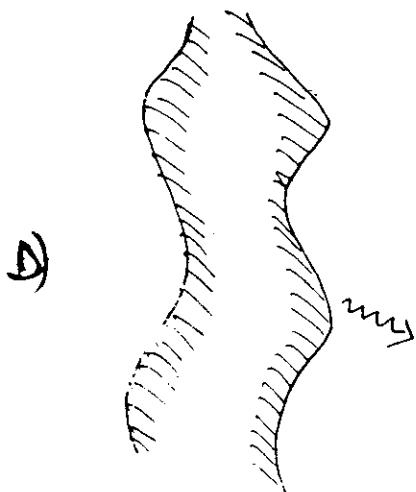
A) "QUANTUM CONFINEMENT":
PL DUE TO RADIATIVE RECOMBINATION
OF EXCITONS LOCALIZED INTO
NANOSTRUCTURES OF c-SILICON
(QUANTUM WIRES OR QUANTUM DOTS)



B) "SURFACE-STATE EMISSION":
PL DUE TO RADIATIVE RECOMBINATION
OF e-h PAIRS TRAPPED INTO
SURFACE STATES DUE TO RANDOM
TERMINATION OF c-Si NANOSTRUCTURE,



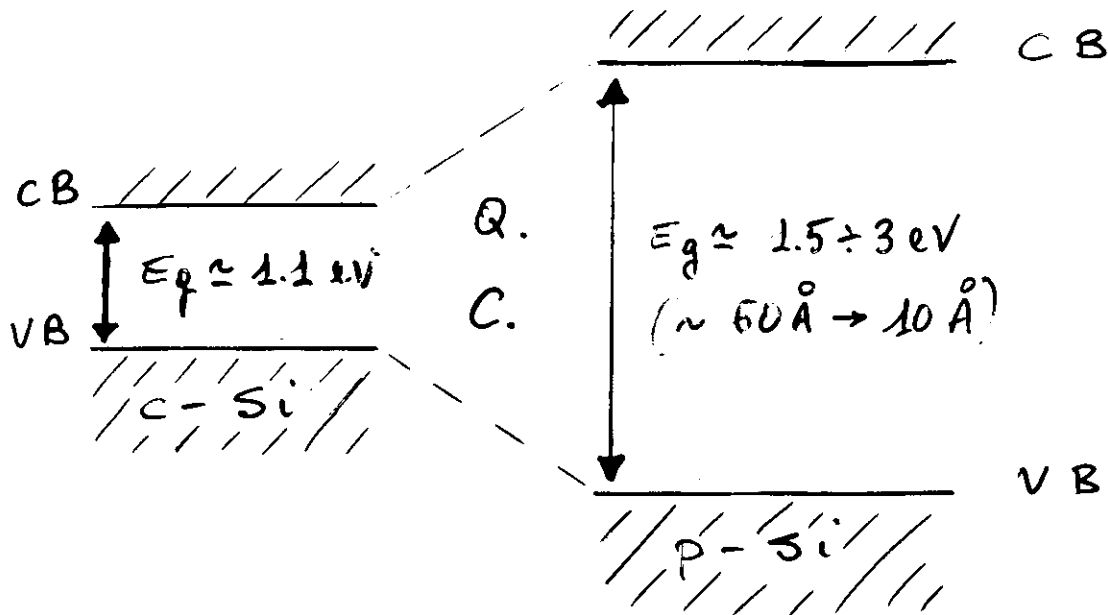
C) "CHEMICAL MODEL":
PL DUE TO RADIATIVE TRANSITIONS
INTERNAL TO SOME CHEMICAL SPECIES
PRESENT IN THE PORE WALLS OF p-Si,
(Polysilanes, Si_3H_8 , siloxanes)



D) "AMORPHOUS MODEL":
ASSUMES THE FORMATION OF AN
a-Si LAYER ON THE TOP OF Si
NANOCRYSTALS, WHERE THE CARRIERS
RECOMBINE.

WHY p-Si DOES EMIT VISIBLE LIGHT?

- QUANTUM CONFINEMENT OF EXCITONS WITHIN THE NANOMETRIC STRUCTURES



POROSITY EFFECTS ON THE BAND-GAP

POROSITY INCREASE



NARROWING OF NANOSTRUCTURES



BROADENING OF THE GAP

i.e.: BLUE SHIFT OF P.L.!

BLUE SHIFT DELLA PL

$\sim 1.4 \text{ eV} \rightarrow 1.6 \text{ eV}$

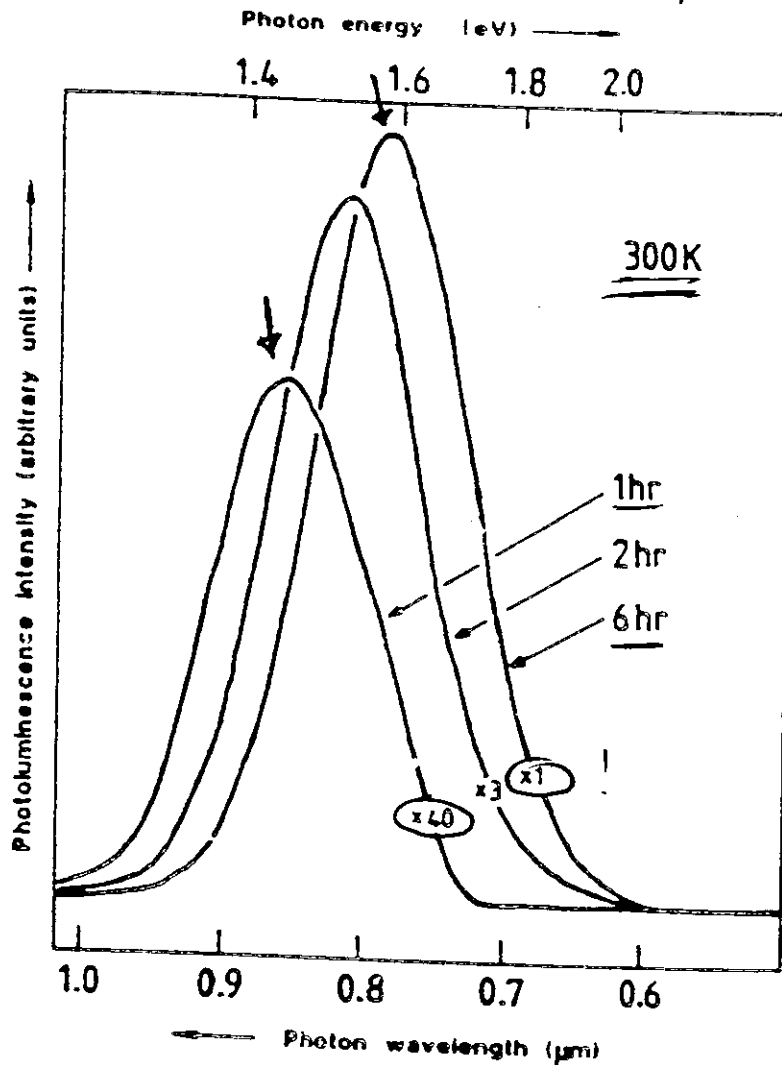
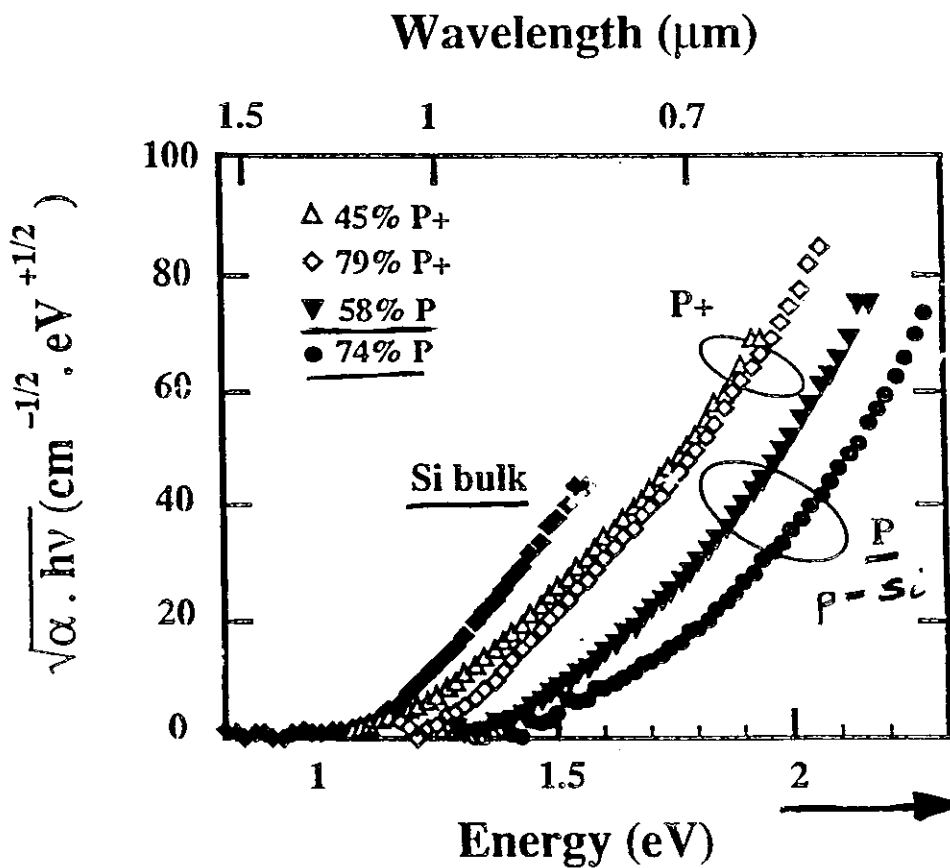


FIG. 3. Room-temperature photoluminescence from the anodized p^- wafer of Fig. 2 after immersion in 40% aqueous HF for the times indicated. Spectra were taken with 200 mW unfocused 5145 Å excitation incident on the sample in air and amplified by the relative gains indicated.

(L.T. CANHAM, A.P.L. 57, 1046 (1990))

OPTICAL ABSORPTION

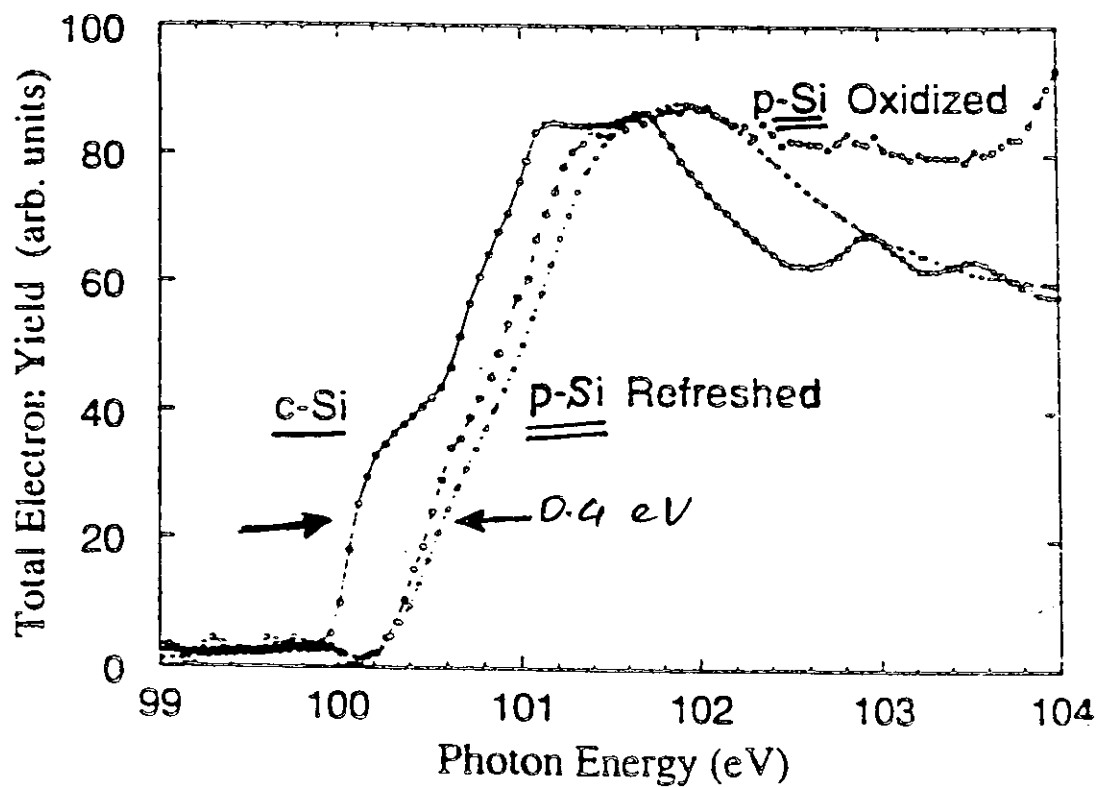
- SPOSTAMENTO DELLO SPICCO
- BAND - EDGE SHIFT!
- HIGHER FOR HIGHER POROSITY



(SAGHES et al., 1992) - 1992

X-RAY ABSORPTION

- Si $L_{2,3}$
- BAND-EDGE SHIFT!



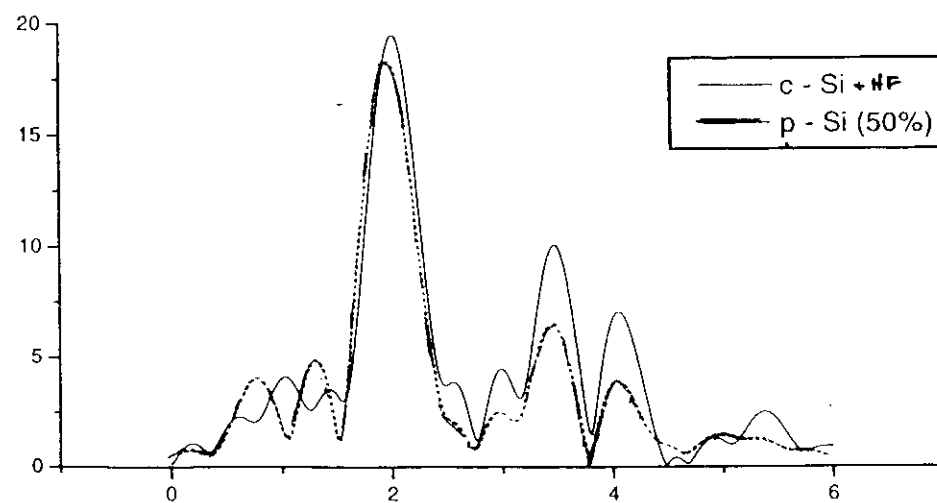
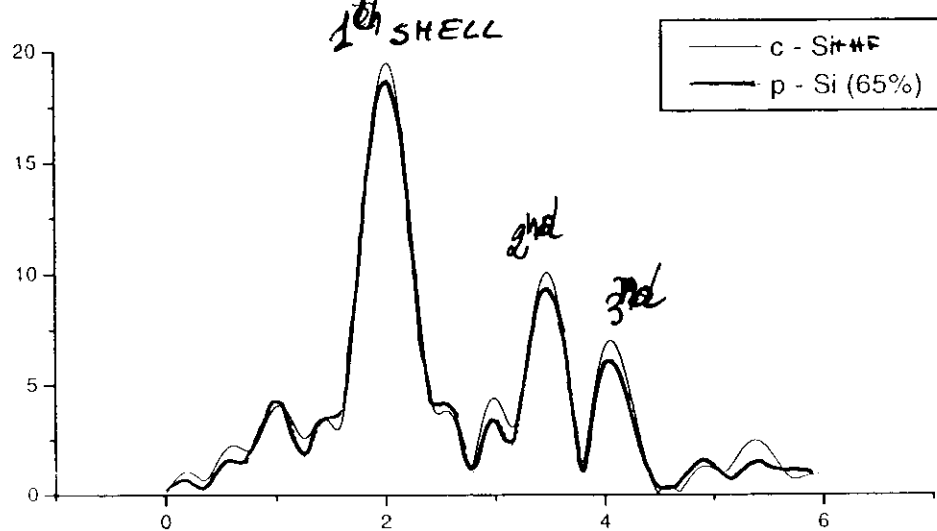
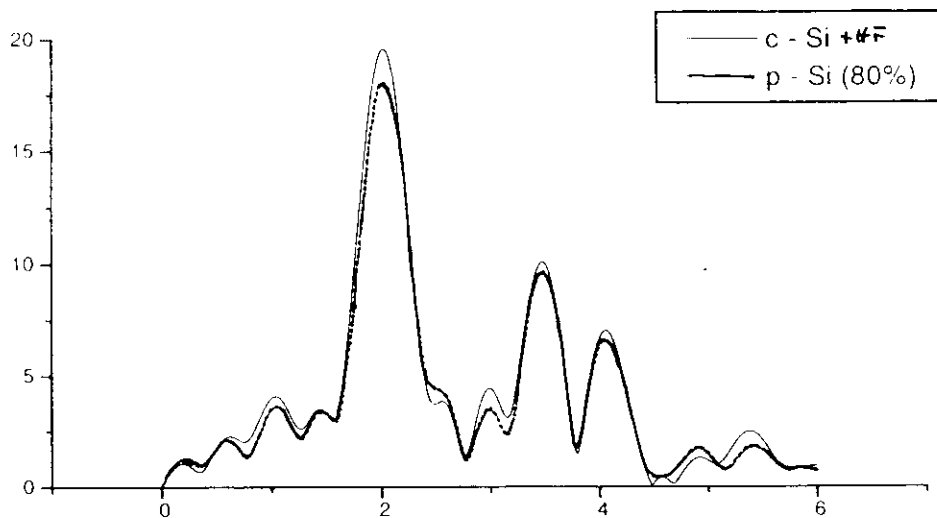
VAN BUREN, BUREN, TROTT, AND BUREN
PHYSICAL REVIEW LETTERS

(VAN BUREN et al., A.P.L. 60, 3013 (1992))

EXAFS

(DALBA, FORTINASSINI, GRISENTI E RUCCA)

Magnitude of Fourier Transform (a.u.)



→ EDGE K OF Si

Interatomic Distance (Å)

~~→ LATER~~

- IL SILICIO POROSO E' ANCORA IN FASE C!

STRUCTURE OF AGED p-Si

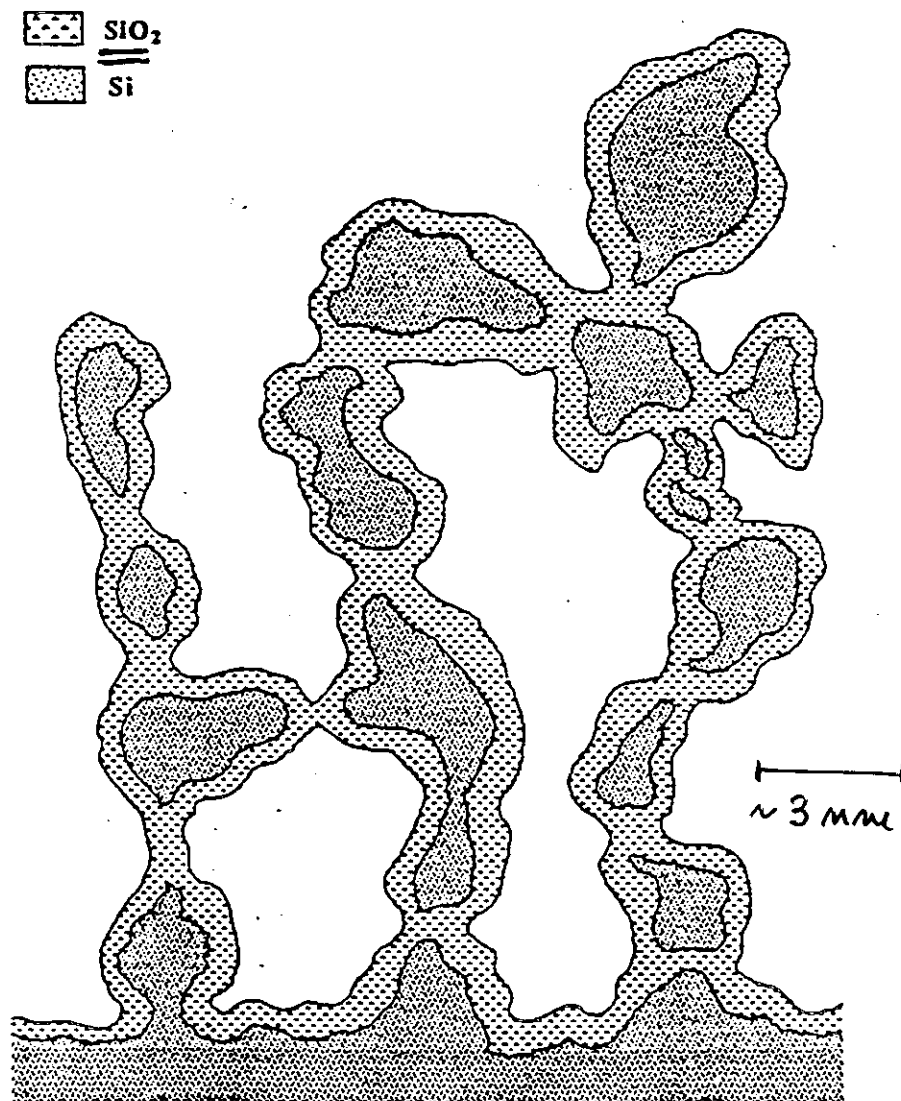
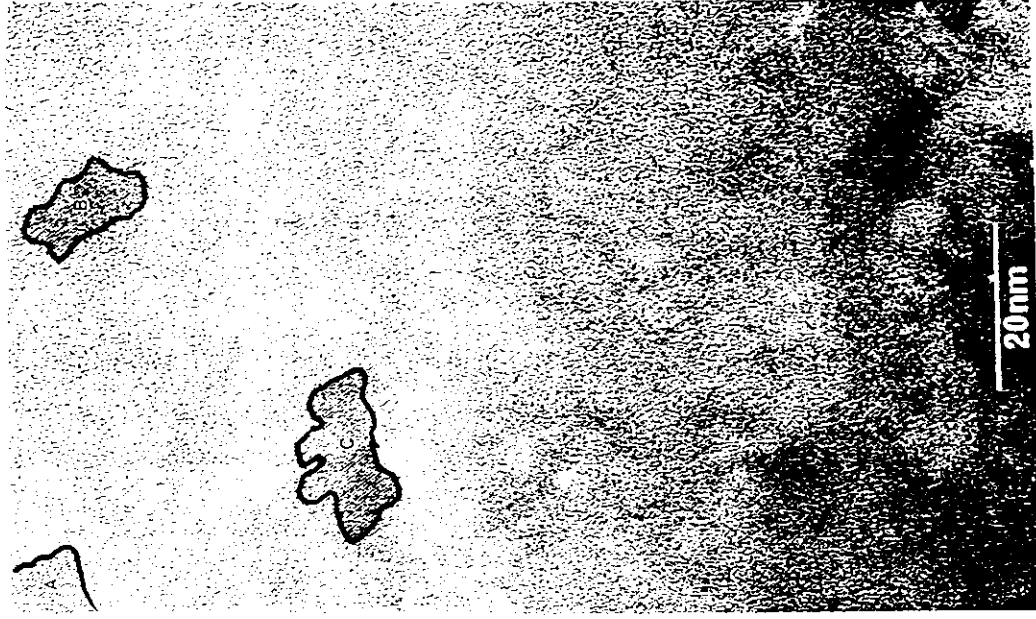
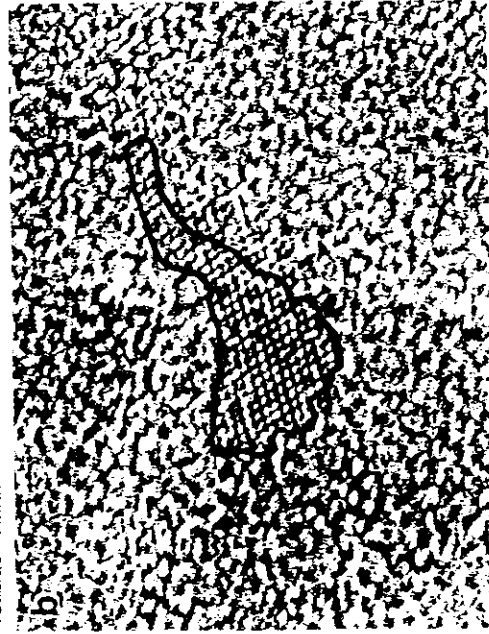
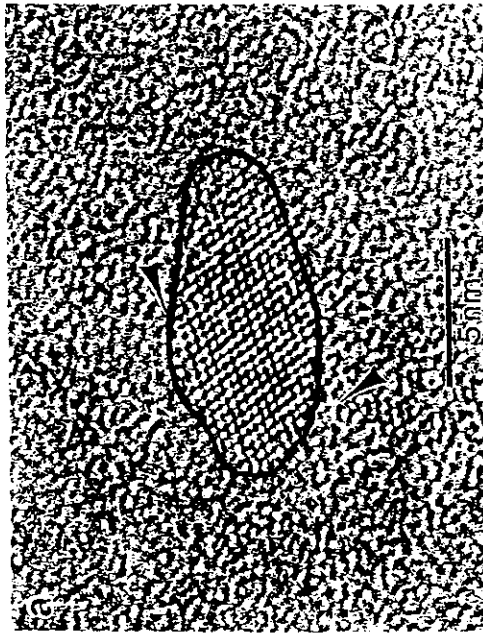


FIG. 9. Schematic representation of the oxidized porous silicon texture for a sample having roughly 70% initial porosity and electro-oxidized up to Q_0 .

PICTURE CONFIRMED BY X-RAY DIFFRACTION
(D. Bellat, S. Billat, G. Dolino, M. Ligeon, F. Muller,
Solid State Commun. 86, 51, 1993)

5 nm



H.R.T.E.M. IMAGES OF P-Si!

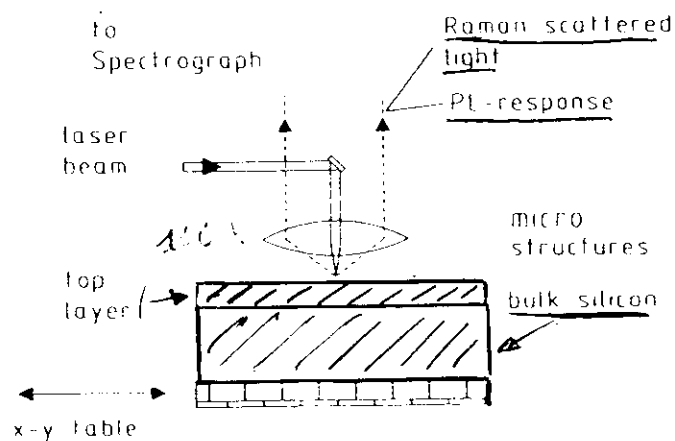
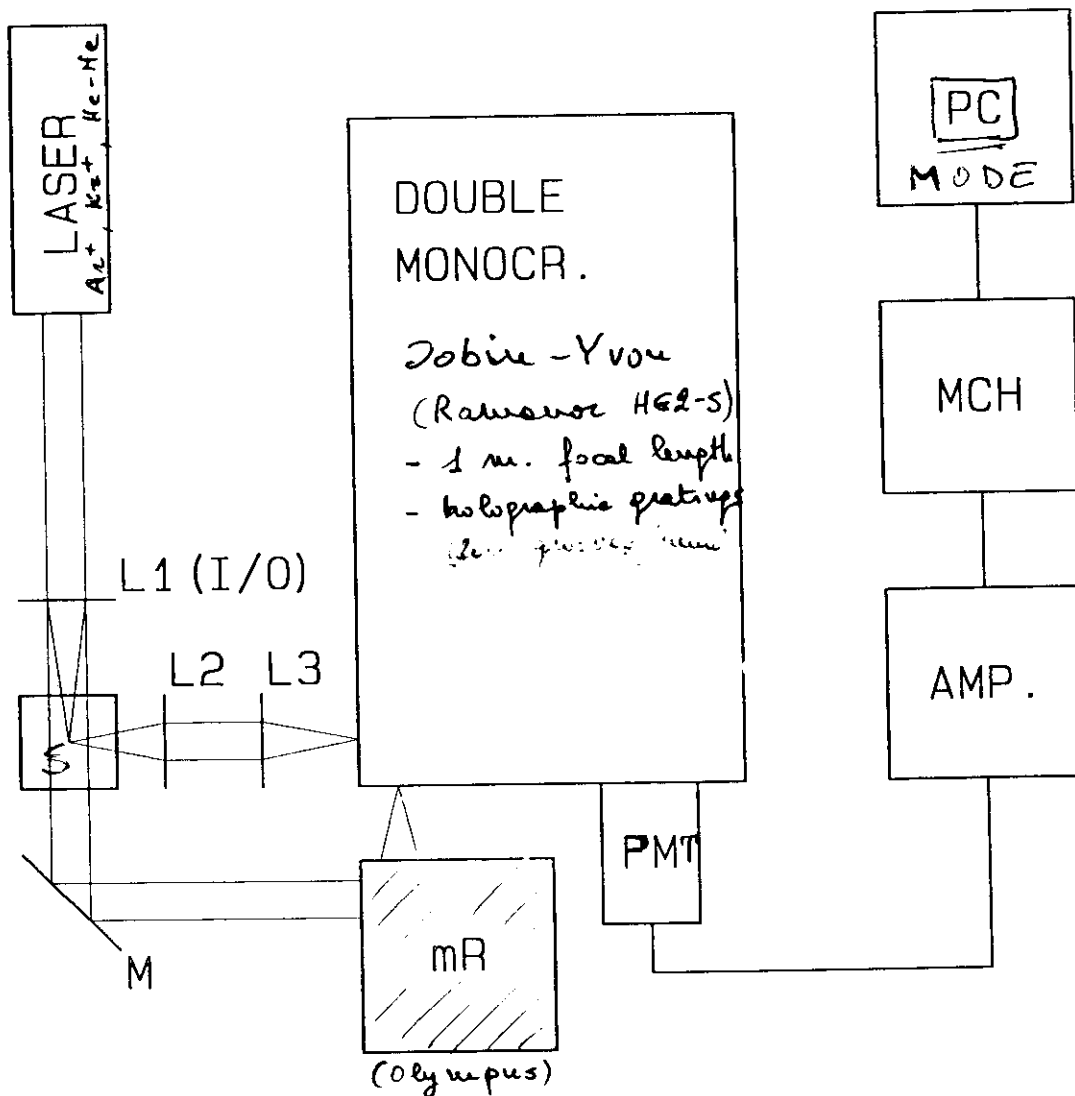
QUESTIONS :

- 1 - NANOCRYSTALS SIZE ?
- 2 - SIZE DEPENDENCE ON THE DEPTH
- 3 - IS IT POSSIBLE TO DETECT THE AMORPHOUS PHASE OVERCOATING THE SURFACE OF p-Si LAYERS ?

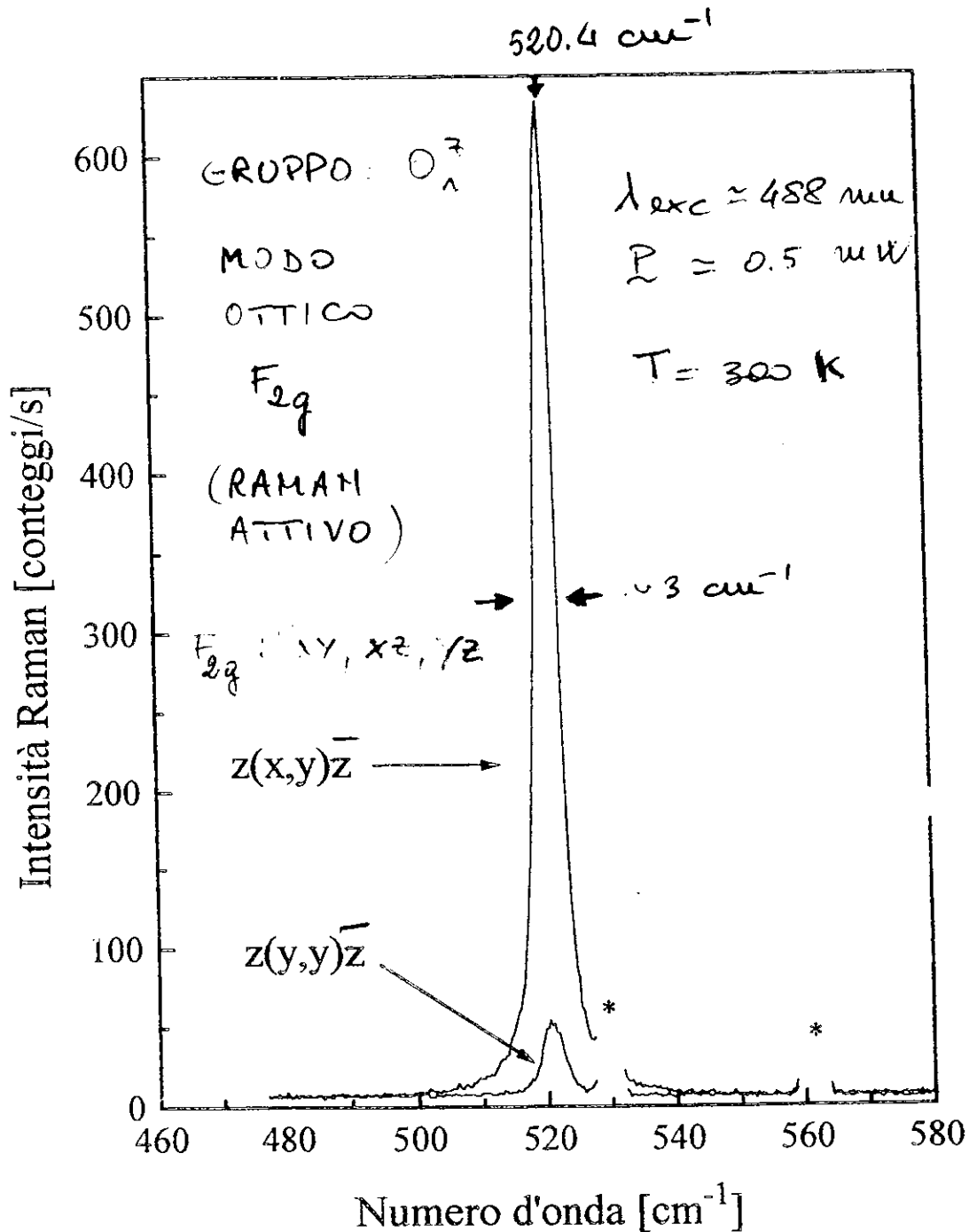
WE HAVE TRIED TO ANSWER BY MEANS OF THE MICROPROBE RAMAN SPECTROSCOPY

- THIS TECHNIQUE IS VERY SENSITIVE TO MICROSTRUCTURAL VARIATIONS OF CRYSTALLINE MATERIALS, SINCE IT PROBES THE VIBRATIONAL DYNAMICS WITH A HIGH-SPATIAL RESOLUTION (i.e.: $\sim 1 \mu\text{m}$)
- VERY RELIABLE TOOL TO STUDY :
 - STRUCTURAL AND MORPHOLOGICAL INHOMOGENEITIES AT SCALE OF MICRONS
 - STRAIN EFFECTS IN FILMS
- WARNING : STRONG SAMPLE HEATING !

RAMAN SET-UP (TRENTO)



SPETTRO MICRO-RAMAN DEL c-Si

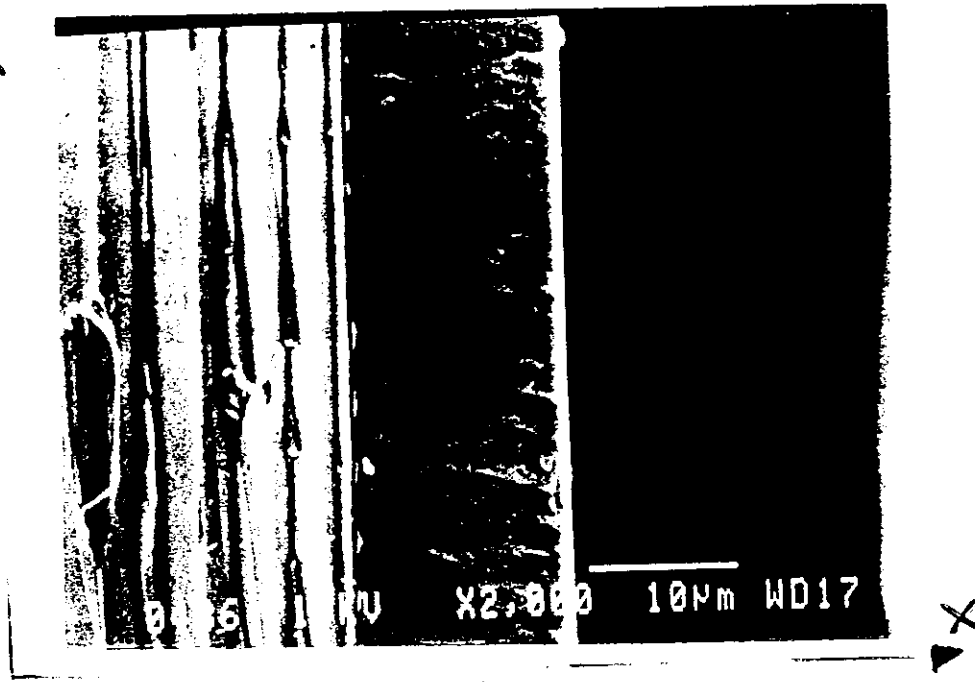


- PICCO STRETTO MOLTO SIMMETRICO!
- FORMA LORENTZIANA.

μ -RAMAN DEPTH-PROFILING OF P-Si

XIAFER CLIVATO E VISTO DI TAGLIO

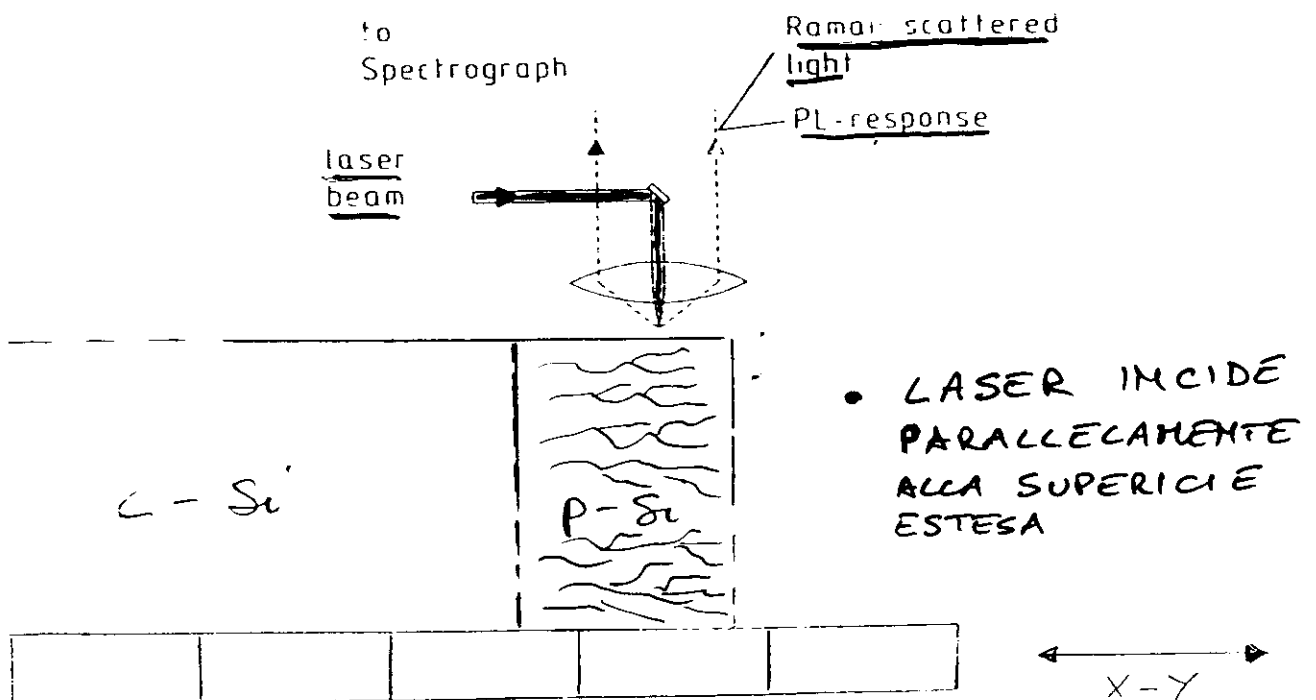
2A



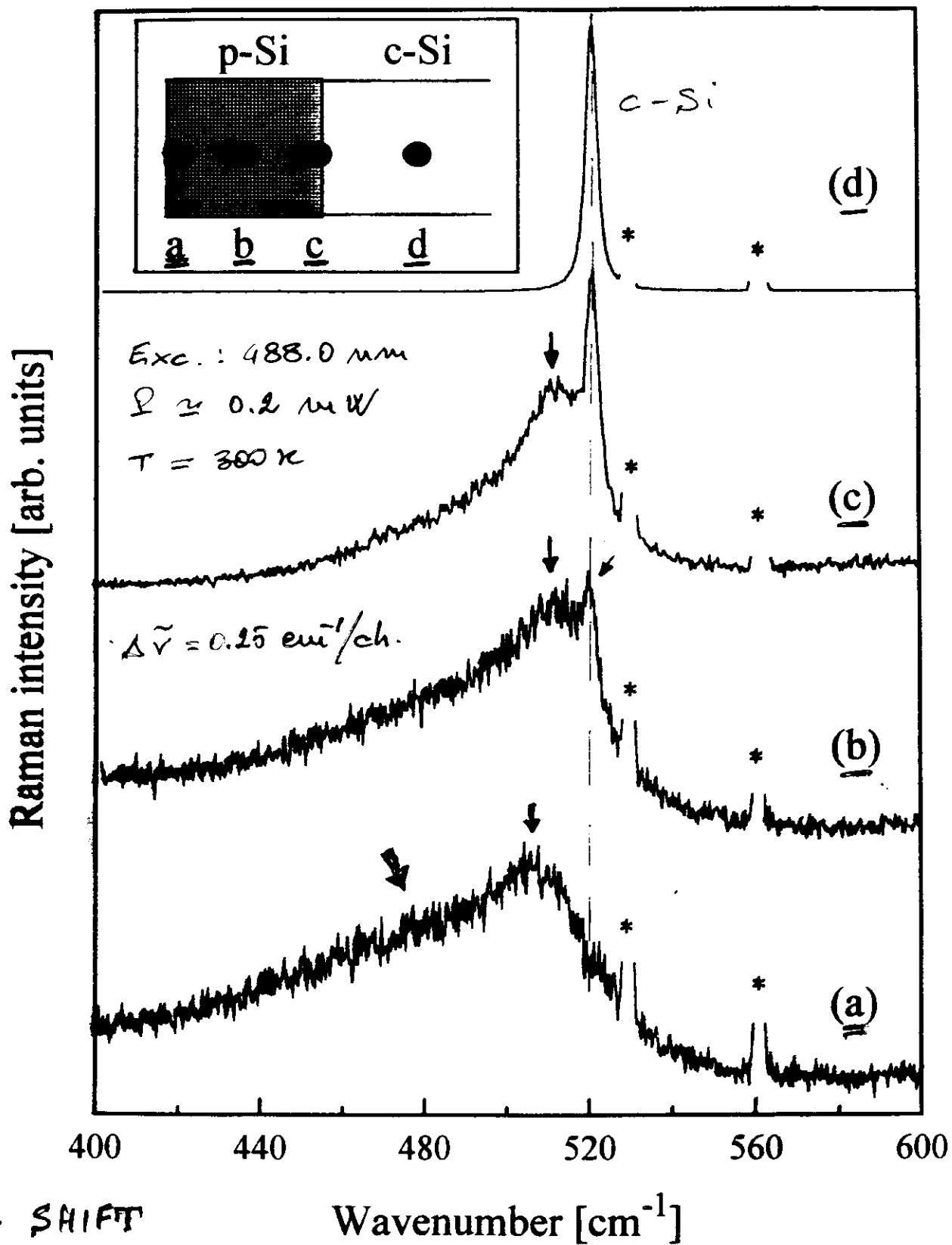
S. # 34

→ 14.8 μ m ←

$\bar{P} \approx 32\%$!



MICRO-RAMAN SPECTRA



- SHIFT
- BROADENING
- ASYMMETRY

PHONON CONFINEMENT MODELS

BASIC ASSUMPTIONS

- Phonon Confinement Models were developed during 80's to account for the observed Raman spectrum of micro-crystalline Silicon [see: Richter et al. (1981), Campbell & Fauchet (1986)].
- As already mentioned, in bulk crystals the phonon eigenstate is a plane wave and the wave vector selection rule for the first-order Raman scattering requires $\mathbf{q} \cong 0$. Thus light scattering experiments probe the centre of the first BZ.
- In contrast, the spatial correlation function of the phonon becomes finite due to its confinement in the microcrystals and hence the wave vector selection rule $\mathbf{q} \cong 0$ for one-phonon processes is relaxed. Therefore in crystalline grains of size L (typically $L \leq 20$ nm) a finite range of the BZ (i.e.: $|\mathbf{q}| \leq 2\pi/L$) becomes accessible to light scattering.
- Since the dispersion curves of optical phonons are not entirely flat over the whole first Brillouin zone, phonon confinement will result both in a peak shift and an asymmetric broadening of first-order Raman spectrum.
- This phenomenological behaviour has been explained by the model proposed by Richter et al. (1981). Their model assumes that the bulk phonon dispersion curves are not affected and no new modes are created due to the size reduction of the crystal.
- Richter's model has been improved by Campbell & Fauchet (1986), and then several works have been reported which show the confinement of optical phonons in different semiconductor crystallites (Ge, C, etc.).

OUTLINE OF THE RICHTER'S MODEL

- Within the model proposed by Richter et al. (1981) the phonon confinement is accounted for by a weight function $W(\mathbf{r}, L)$, where L is the size of nanocrystals with spherical shape.
- The phonon wavefunctions are still described by plane waves with the same lattice periodicity of bulk crystal, but the weight function $W(\mathbf{r}, L)$ acts so that their amplitude turns out negligible or equal to zero at the grain surface.
- Formally the wavefunction of a phonon of wavevector \mathbf{q}_0 in perfect crystal can be written as:

$$\Phi(\mathbf{q}_0, \mathbf{r}) = u(\mathbf{q}_0, \mathbf{r}) \exp(+i\mathbf{q}_0 \cdot \mathbf{r})$$

where $u(\mathbf{q}_0, \mathbf{r})$ is a Bloch function, with the same periodicity as the crystal lattice.

- In contrast, the wave-packet associated to a phonon confined within a spherical nanocrystal of diameter L by the weight function $W(\mathbf{r}, L)$ can be written as:

$$\begin{aligned}\Psi(\mathbf{q}_0, \mathbf{r}) &= W(\mathbf{r}, L) \cdot \Phi(\mathbf{q}_0, \mathbf{r}) \\ &= [W(\mathbf{r}, L) \cdot \exp(+i\mathbf{q}_0 \cdot \mathbf{r})] u(\mathbf{q}_0, \mathbf{r}) \\ &= \Psi'(\mathbf{q}_0, \mathbf{r}; L) \cdot u(\mathbf{q}_0, \mathbf{r}).\end{aligned}$$

- The development of $\Psi'(\mathbf{q}_0, \mathbf{r}; L)$ in series of Fourier is:

$$\Psi'(\mathbf{q}_0, \mathbf{r}; L) = \int_{1st \text{ B.Z.}} C(\mathbf{q}_0, \mathbf{q}) \cdot \exp(+i\mathbf{q} \cdot \mathbf{r}) d^3q,$$

where the Fourier coefficients $C(\mathbf{q}_0, \mathbf{q})$ are given by:

$$\begin{aligned}C(\mathbf{q}_0, \mathbf{q}) &= (1/2\pi) \int \Psi'(\mathbf{q}_0, \mathbf{r}; L) \cdot \exp(-i\mathbf{q} \cdot \mathbf{r}) \\ &= (1/2\pi) \int W(\mathbf{r}, L) \cdot \exp[-i(\mathbf{q} - \mathbf{q}_0) \cdot \mathbf{r}] d^3r\end{aligned}$$

- Now, recalling that in bulk crystals only $\mathbf{q} \cong 0$ phonons give Raman scattering, we can assume this approximation:

$$C(\mathbf{q}_0, \mathbf{q}) \equiv C(\mathbf{0}, \mathbf{q}),$$

and use $C(\mathbf{0}, \mathbf{q})$ in the calculations of Raman line shape.

- Therefore, the first-order Raman spectrum $I(\omega)$ is given by:

$$I(\omega) = \int_{1\text{st B.Z.}} |C(\mathbf{0}, \mathbf{q})|^2 \cdot \Lambda(\omega, \mathbf{q}, \Gamma_0) d^3\mathbf{q}$$

where $\Lambda(\omega, \mathbf{q}, \Gamma_0)$ is a lorentzian curve centred at $\omega(\mathbf{q})$, with a full width at half-maximum (FWHM) of Γ_0 :

$$\Lambda(\omega, \mathbf{q}, \Gamma_0) \propto 1/\{[(\omega - \omega(\mathbf{q}))^2 + (\Gamma_0/2)^2]\}.$$

- In conclusion, within the PCM developed by Richter et al. : the first order Raman spectrum of a nanocrystal is given by the weighted (by the weighting coefficients $|C(\mathbf{0}, \mathbf{q})|^2$) sum of many lorentzian components, all of them having the same FWHM, but each of them being peaked at the energy $\omega(\mathbf{q})$, compatible with the phonon dispersion curves of bulk crystal. The weight of each lorentzian component being defined by the weighting function $W(\mathbf{r}, L)$ throughout the Fourier coefficients $C(\mathbf{0}, \mathbf{q})$.

- Richter et al. assumed a gaussian function $W(\mathbf{r}, L)$ to account for the phonon confinement effects observed in the first-order Raman spectrum of nanocrystalline silicon.

- The model proposed by Richter et al. has been reconsidered and generalized to nanocrystals with non-spherical shapes (i.e.: columns and slabs) by Campbell and Fauchet (1986), who also used three different confinement functions $W(\mathbf{r}, L)$, i.e.: exponential, gaussian and sinc functions, to fit experimental Raman spectra obtained from nanocrystalline silicon films.

OUR ASSUMPTIONS

- We have best-fitted the experimental spectra carried out from our p-Si samples according to the model originally developed by Richter et al. (1981). Therefore we have chosen:

- Shape of silicon nanocrystals: spherical shape.

- Shape of the confinement function: Gaussian function

$$W(r,L) = A \exp (-8\pi^2 r^2/L^2),$$

where L is the diameter of a spherical nanocrystal. In this case, the weighting coefficients are $|C(0,q)|^2 = \exp [-(9L/4\pi)^2]$.

- Phonon dispersion branches: Approximation with an analytical curve (parabola, with numerical coefficients extrapolated from inelastic neutron scattering results).

- Symmetry of the first Briullouin zone: if the first BZ is assumed to be spherical, then the frequencies of the different phonon branches are independent of the direction, so that:

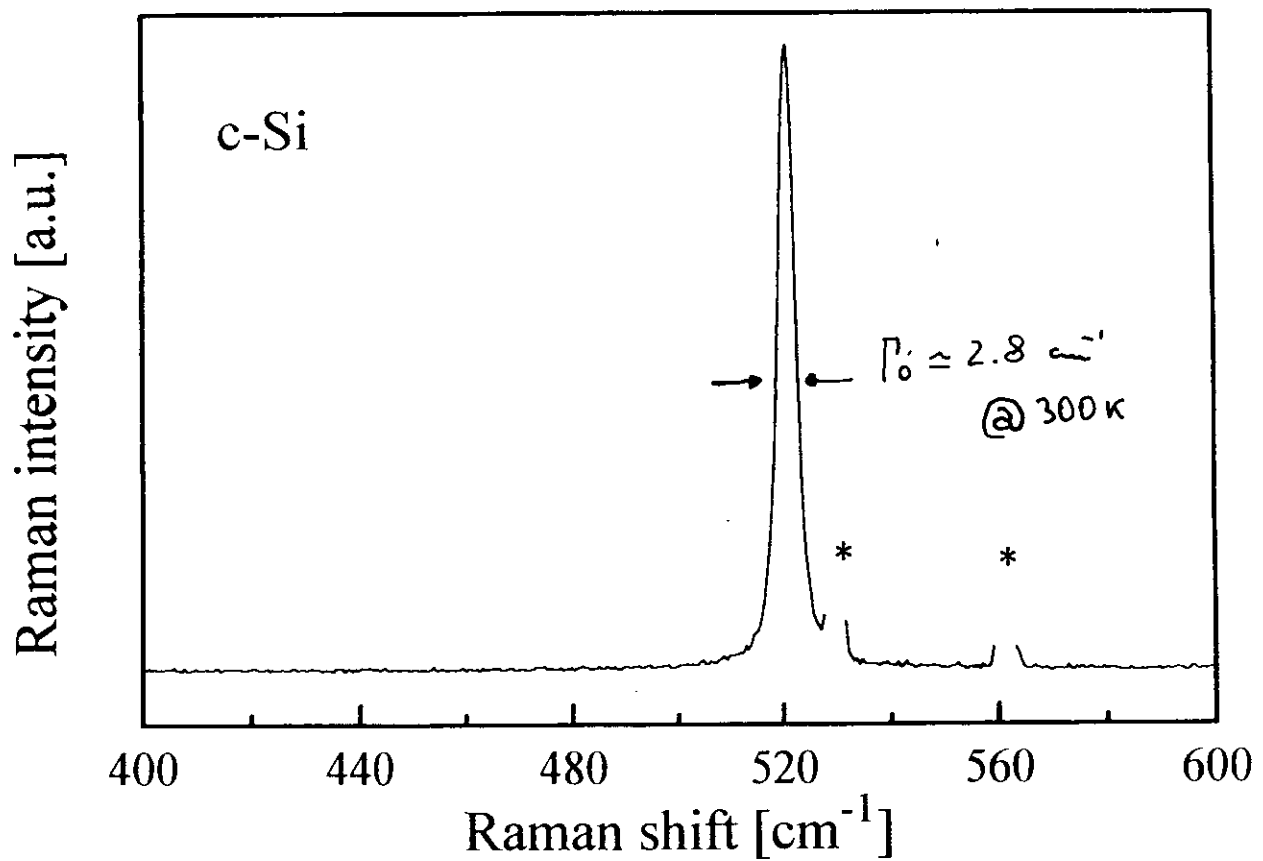
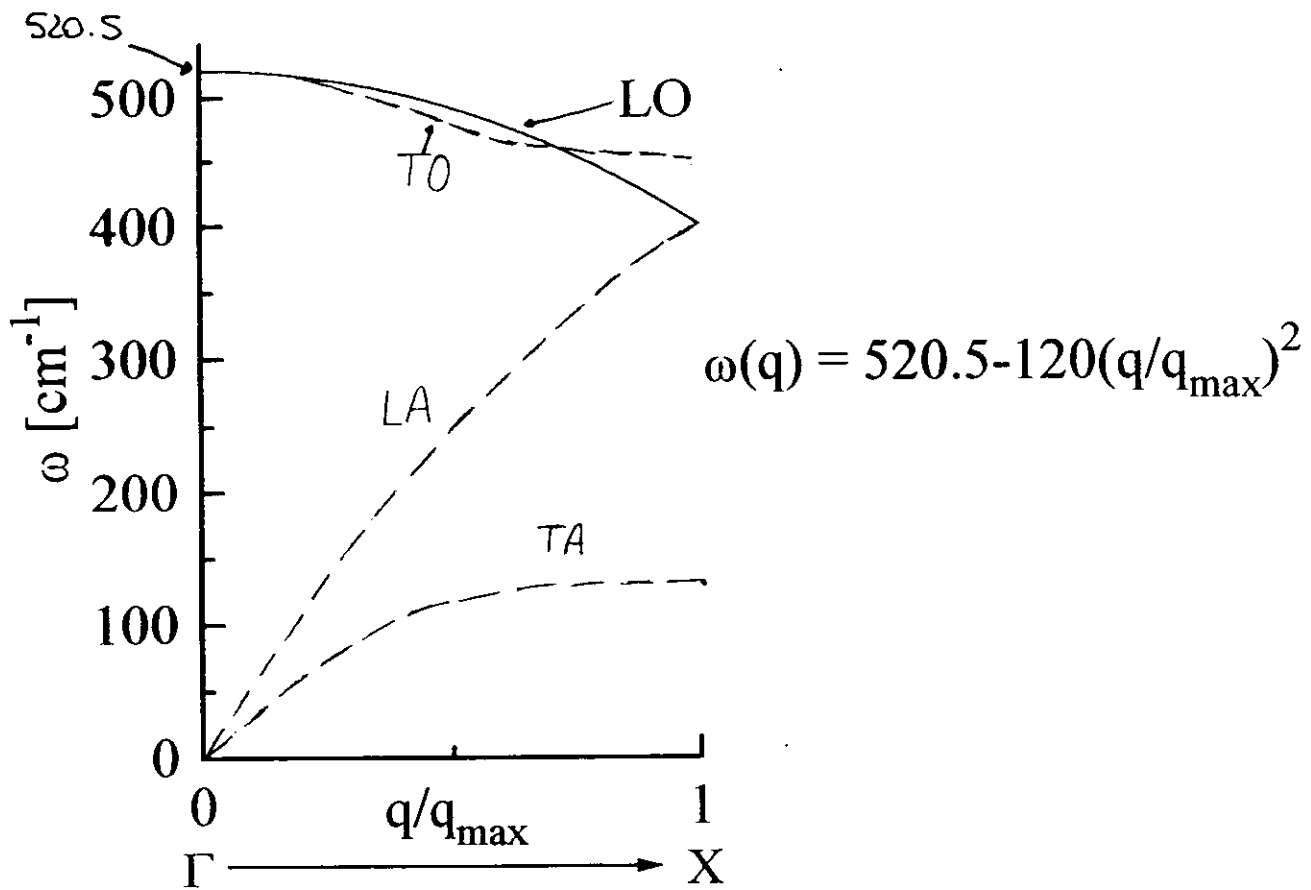
$$\omega(\mathbf{q}) \equiv \omega(q)$$

and the first-order Raman spectrum $I(\omega)$ simply becomes:

$$I(\omega) = \int_{0 \rightarrow q(\max)} |C(0,q)|^2 \cdot \Lambda(\omega,q,\Gamma_0) dq.$$

- Our fit of experimental data was reasonable, but unrealistic, since it assumed an identical size for all p-Si structures. Therefore, in order to improve our fit we introduced a more realistic inhomogeneous distribution of nanocrystal size.

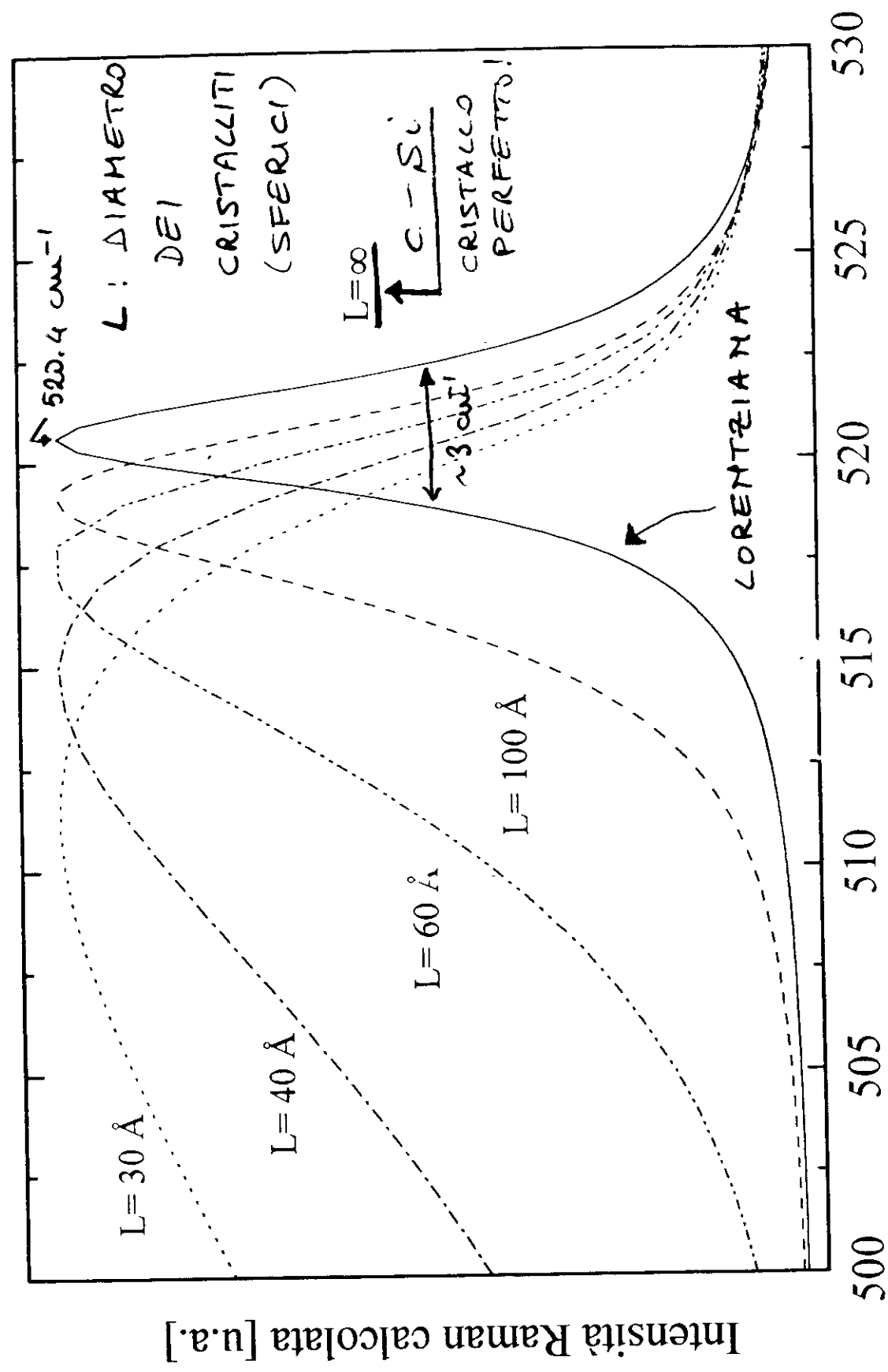
SEMI-CLASSICAL THEORY OF PHONON DISPERSION



* = LINEE DI PLASMA DEL
LASER AD Ar^+

PHONON CONFINEMENT MODEL

SPETTRO RAMAN DEL $\mu\text{C-Si}$ (CALCOLATO)



SPECTRAL EFFECTS OF A INHOMOMOGENEOUS DISTRIBUTION OF NANOCRYSTAL SIZES

- Phonon confinement model developed by Richter et al. (as well as the Campbell and Fauchet one) assumes a homogeneous distribution of the nanocrystal dimensions. This hypothesis seems too drastic in the case of p-Si.
- We can overcome this limitation by introducing in their model an inhomogeneous distribution $P(L)$ of crystal sizes in terms of a gaussian curve, characterized by a dispersion σ :

$$P(L) \propto \exp[-(L-L_0)/2\sigma^2]$$

where L_0 is the mean crystal size.

- The first-order Raman spectrum $I(\omega)$ is now:

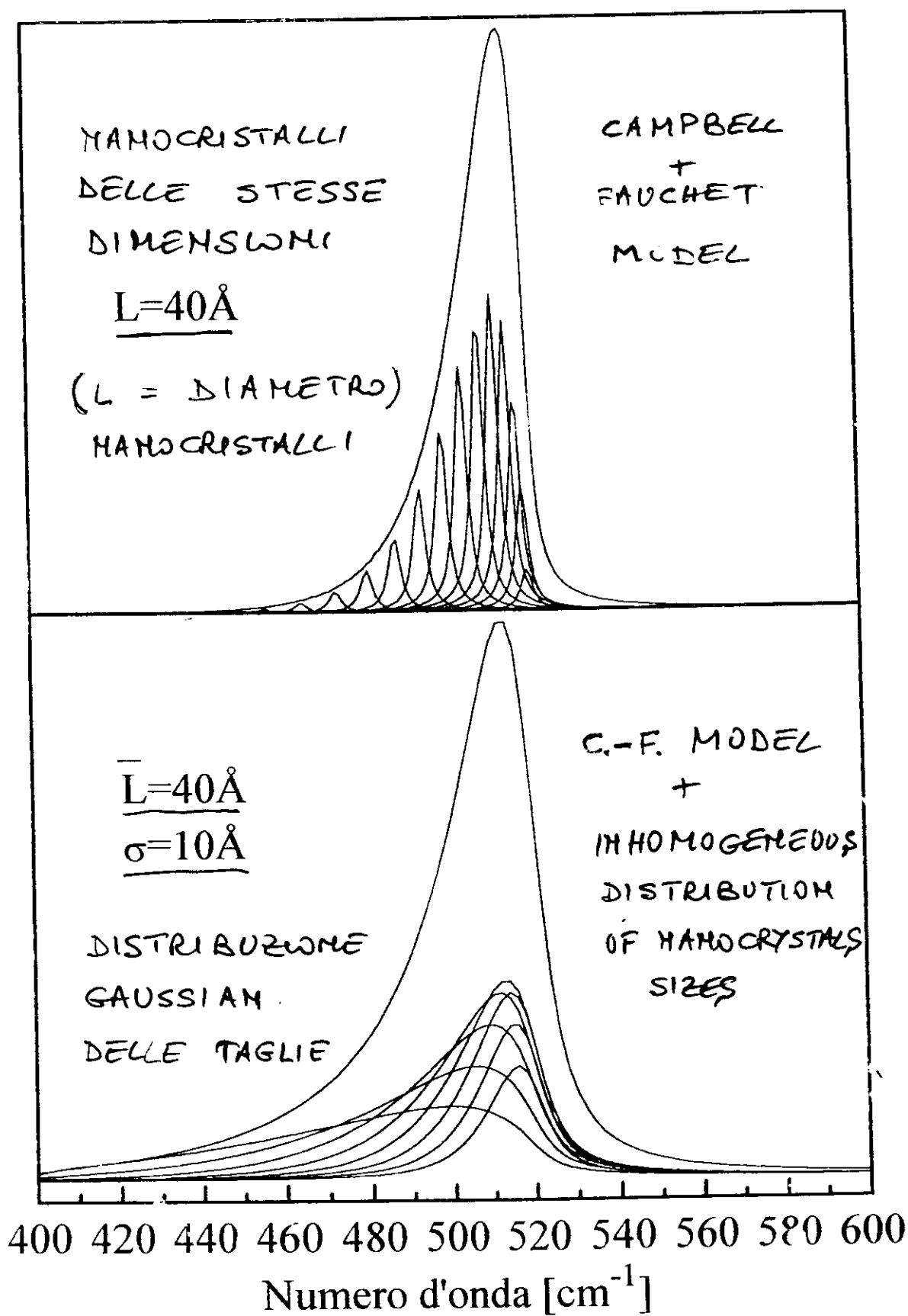
$$I(\omega) \propto \int_{0 \rightarrow q(\max)} q^2 \cdot f(q) \cdot \exp[-(qL_0 f(q)/4\pi)^2] \cdot \Lambda(\omega, q, \Gamma_0) dq$$

where $f(q) = 1 + (q^2 \sigma^2 / 8\pi^2)^{-1/2}$.

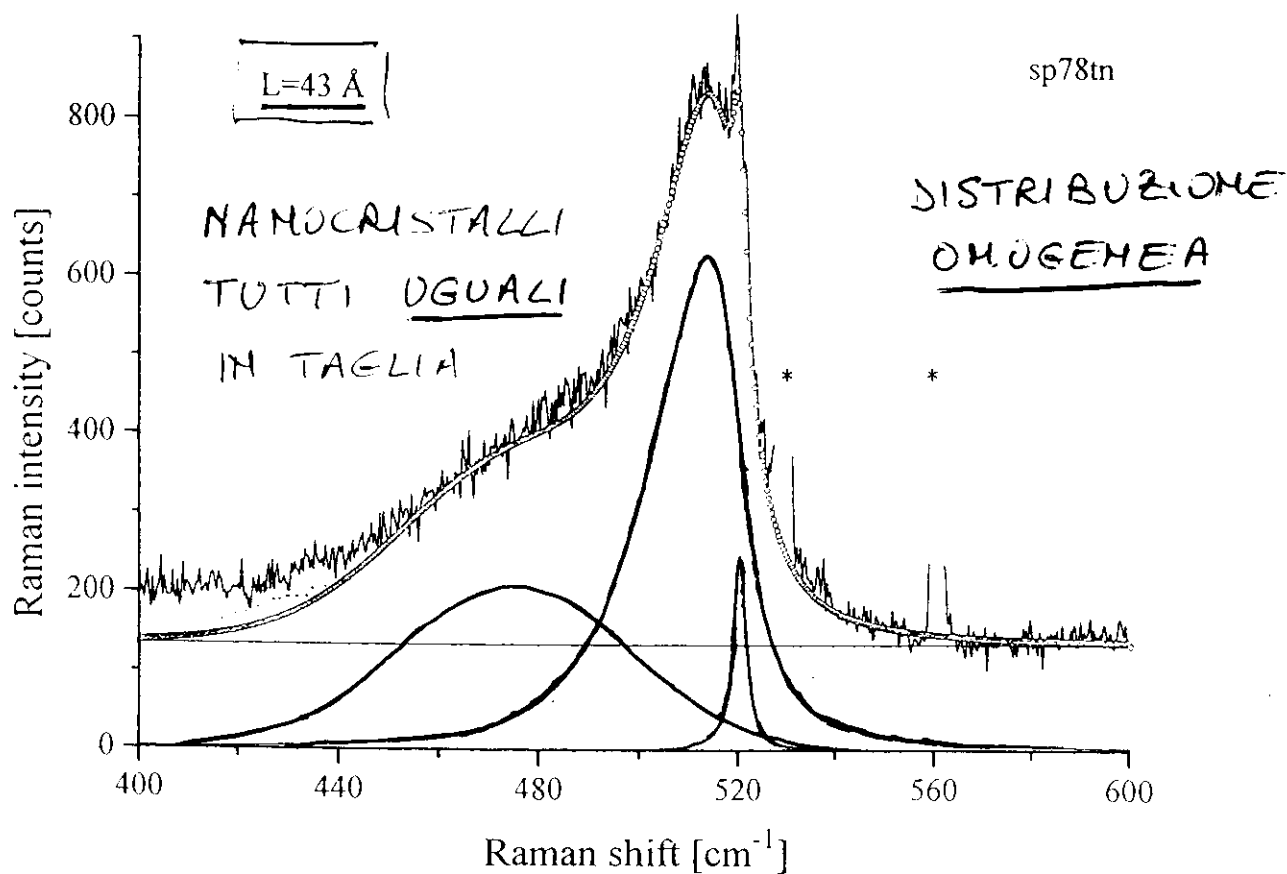
- The main spectral effects due to the inhomogeneous nanocrystals size distribution $P(L)$ are a stronger asymmetry and broadening of the Raman peak of p-Si, with no evidence of any additional shift with respect to Richter model.
- Comparison between results of calculation carried out for:
 - a homogeneous distribution of nanocrystal size L_0 ;
 - an inhomogeneous distribution of nanocrystal size around L_0 .
- Comparison between the two different fits of Raman spectra.

SPETTRO RAMAN DEL Si NANOCRISTALLINO

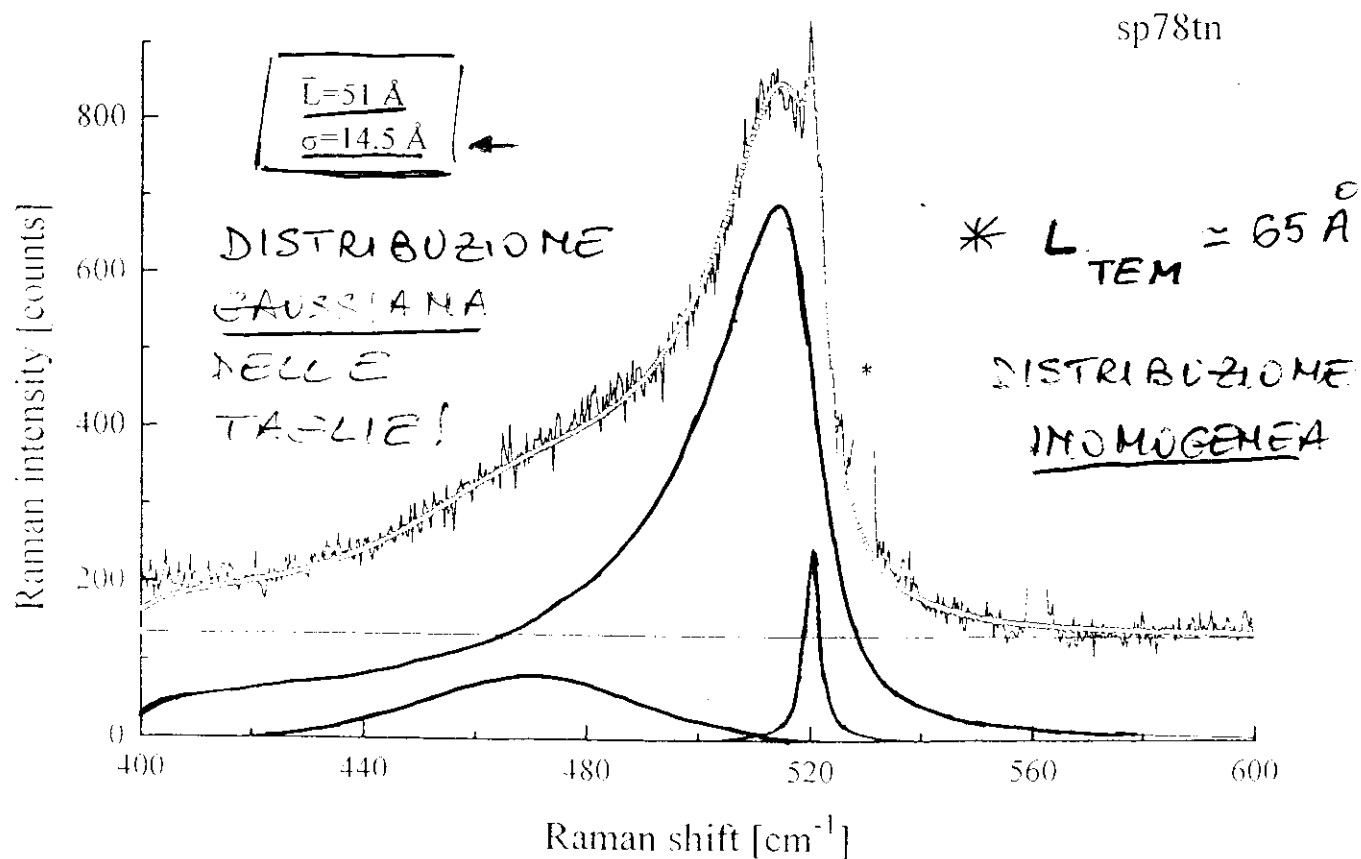
Intensità Raman calcolata [un. arb.]

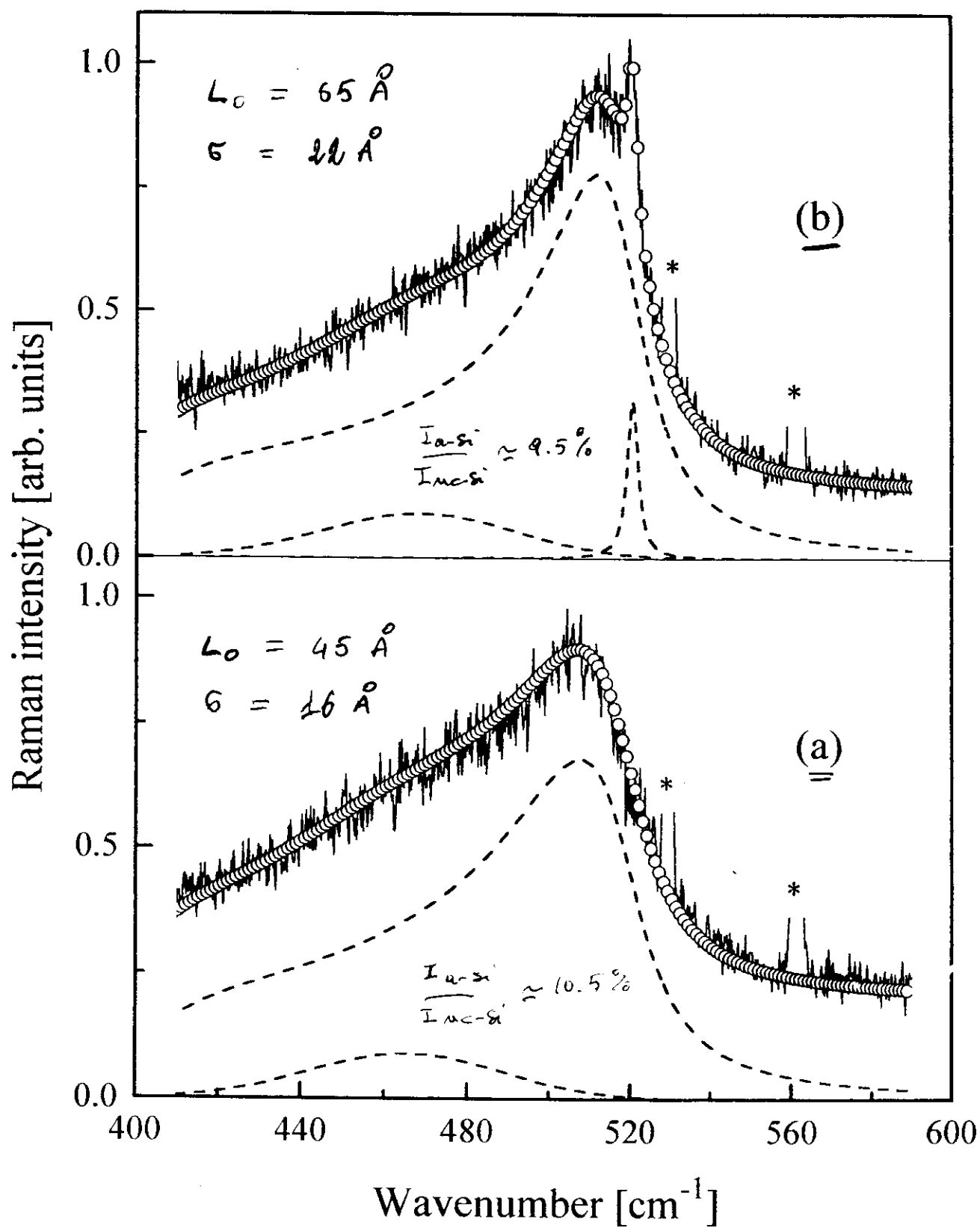


MODELLO DI FAUCHET E CAMPBELL



MODELLO DI TORRIANI E SANTOS





CONCLUSIONS

DEPTH-PROFILE OF RAMAN SCATTERING FROM AGED P-Si (P-TYPE) LAYERS INDICATES:

- NANOCRYSTALLINE STRUCTURE
- PRESENCE OF α -Si COMPONENT AT ANY DEPTH
- DEPTH-DEPENDENCE OF NANOCRYSTALS SIZE (SIZE DECREASE IN THE ORDER OF 30% NEAR THE INTERFACE BETWEEN P-Si AND VACUUM)
- INHOMOGENEOUS SIZE-DISTRIBUTION THROUGHOUT THE CROSS SECTION OF POROUS LAYERS WITH QUITE SMALL DISPERSION
- NANOCRYSTALS SIZE DERIVED BY APPLICATION OF THE PHONON CONFINEMENT MODEL (WITH AN INHOMOGENEOUS DISTRIBUTION OF SIZES) IS IN FAIRLY GOOD AGREEMENT WITH T.E.M. RESULTS



ELSEVIER

Journal of Non-Crystalline Solids 192 & 193 (1995) 253–257

JOURNAL OF
NON-CRYSTALLINE SOLIDS

Light-emitting porous silicon: a structural investigation by high spatial resolution Raman spectroscopy

G. Mariotto ^{a,*}, F. Ziglio ^a, F.L. Freire Jr. ^b^a *Dipartimento di Fisica, Università di Trento, Via Sommarive 14, 38050 Povo, TN, Italy*^b *Departamento de Física, Pontifícia Universidade Católica do Rio de Janeiro, Caixa Postal 38071, 22452-970 Rio de Janeiro, RJ, Brazil*

Abstract

The structure of light-emitting porous silicon layers, prepared by anodization of p-type wafers, has been investigated as a function of depth by microprobe Raman spectroscopy. The depth-profiles of the Raman scattering from aged samples, several micrometres thick, were carried out in the region of the optical phonons for crystalline silicon. The Raman data indicate the presence of both a predominant nanocrystalline phase and of an amorphous silicon component at any depth within the porous layers. A quantitative analysis of the experimental spectra is carried out in the frame of phonon confinement models, by assuming both a spherical shape for the nanocrystals and an inhomogeneous distribution of their sizes. When the probing laser spot approaches the region near the interface with vacuum, a remarkable reduction of the average size of the nanocrystals is found, with a substantially unchanged a-Si component.

1. Introduction

Since the pioneering work of Canham [1], light-emitting porous silicon (p-Si) has been the subject of both theoretical and experimental research aimed at clarifying the relationships between its structural, electronic and dynamical properties. Many experimental investigations of p-Si currently address the relationship between the optical properties of this material and its structure. Following an initial paper by Tsu et al. [2], where a correlation was derived between Raman and photoluminescence (PL) spectra, Raman scattering has been extensively used as a probe of p-Si microstructure, with some controversial results [3–5]. In fact, while Tsu et al. [2] found

that the PL in anodically etched samples originates from extremely small structures, of the order of 2–3 nm in size, which also cause phonon confinement, Perez et al. [3] provided a direct evidence for an amorphous silicon (a-Si) component in light-emitting p-Si structures. Both optical and structural properties of p-Si samples, fabricated under diverse conditions, were systematically studied by Lockwood et al. [4] and, independently, by Reshina and Guk [5]: a variety of results was observed, with no apparent correlation between the Raman and PL spectra and the preparation conditions.

In a different approach, aimed at probing the structural and compositional homogeneity of p-Si layers, micro-measurement techniques can be used. So far, depth profiles for both Raman scattering and PL have been carried out independently for anodically etched n-type silicon wafers by two groups [6,7]. Both studies revealed the presence of important

* Corresponding author. Tel: +39-461 881 501. Telefax: +39-461 881 696. E-mail: mariotto@science.unitn.it.

structural inhomogeneities in p-Si, which strongly affect the optical properties of this material.

In the present work, the microstructure of light-emitting p-Si layers, obtained from p-type Si (100) wafers, has been investigated by high spatial resolution Raman spectroscopy. Depth-profiles for the Raman scattering, recorded from the cleaved edge in the spectral region of the optical phonons for crystalline silicon (c-Si), reveal the presence of both amorphous and nanocrystalline Si phases at any depth within the porous layers. An evaluation of the typical sizes of the nanocrystalline structures is obtained using a phenomenological model based on the spatial confinement of phonons.

2. Experimental procedures

Porous silicon samples were prepared by the anodic etching of p-type ($\rho \sim 3 \Omega \text{ cm}$) silicon (100) wafers using a $\text{HF-C}_2\text{H}_5\text{OH-H}_2\text{O}$ (1:2:1) solution in a custom-built cell. The details of the electrochemical cell are reported elsewhere [8]. The current source was an EG&G PAR (model 273 A) current generator. A current density of 25 mA/cm^2 and an etch time of 600 s were used to prepare the samples. The thickness of the porous layers was determined by optical microscopy, and their porosity, P was evaluated by weight loss measurements carried out immediately after the anodization. For the Raman scattering depth profiles, the samples were cleaved.

Room-temperature Raman measurements were carried out using a microprobe set-up consisting of an Olympus microscope (model BH-2) with a 100 X objective coupled to a 1 meter focal length double-pass monochromator (Jobin-Yvon, Ramanor model HG2-S) equipped with holographic gratings (2000 line/mm) for the analysis of the scattered radiation. The sample was excited by means of the 488.0 nm line from an Ar^+ ion laser and, after passing through the monochromator, the scattered light was detected by a cooled GaAs photomultiplier tube operated in photon counting mode.

The laser spot area at the sample surface was approximately $5 \mu\text{m}^2$ with a power density of $\sim 5 \times 10^3 \text{ W/cm}^2$ in order to minimize the heating effects. Under these irradiation conditions the heating of the sample was negligible [8]. The instrumen-

tal band pass was $\sim 1.5 \text{ cm}^{-1}$ at 488.0 nm, and the spectral resolution 0.25 cm^{-1} . The wavenumbers of two plasma lines at 529.5 cm^{-1} and at 560.6 cm^{-1} , falling within the spectral region investigated, were used for the energy calibration. The probe beam was positioned in turn over different, apparently homogeneous regions of the cleaved wafer edge, and a Raman spectrum was recorded at each step, thus obtaining Raman scattering depth-profiles of several p-Si layers.

3. Results

Typical experimental Raman spectra of a low-porosity ($P \sim 32\%$) p-Si layer ($\sim 15 \mu\text{m}$ thick),

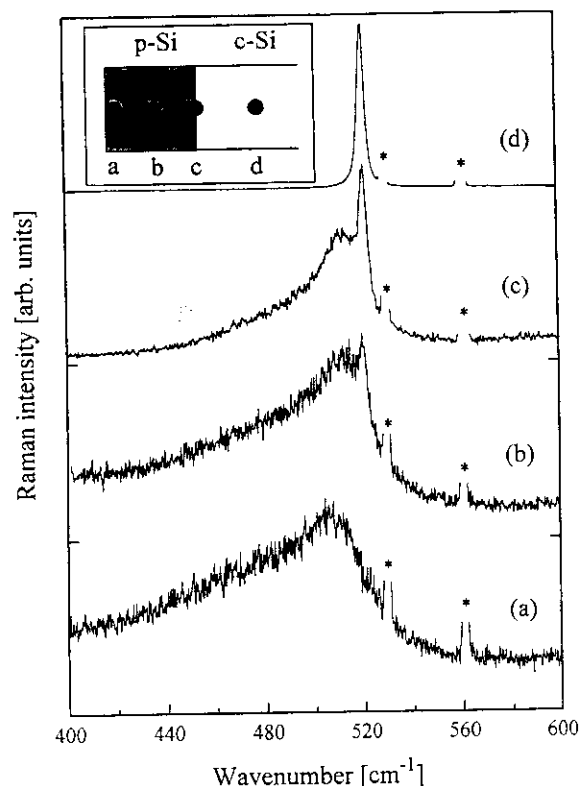


Fig. 1. Experimental micro-Raman spectra for a low-porosity ($P = 32\%$) layer ($15 \mu\text{m}$ thick) aged in air for 2 months. The spectra, excited at different depths within the cross-section of the wafer by means of the 488.0 nm line, were measured at room temperature in the region of the optical phonons for c-Si. The asterisks (*) label the position of two plasma lines used as energy standards. The position of the probing laser spot, for each spectrum, is shown in the inset.

aged in air for 2 months, are plotted in Fig. 1. The first-order Raman scattering of c-Si (spectrum (d)), shown for comparison, consists of a single, highly symmetric line peaked at 520.4 cm^{-1} with an observed full width at half maximum (FWHM) of 3.4 cm^{-1} . Spectrum (c) clearly shows two distinct components: a c-Si-like peak and a broad asymmetric band, shifted to lower energy with respect to the c-Si phonon peak. This reflects the heterogeneous structure of the sample region probed, which was situated just at the p-Si/c-Si interface (see the inset of Fig. 1).

The spectra excited at different depths within the porous layer (Fig. 1(a) and (b)) mainly consist of this broad asymmetric band, peaked at lower energy with respect to the Raman peak for c-Si. The characteristics shown by these spectra are typical manifestations of the spatial confinement of phonons, a well recognized effect in microcrystalline silicon ($\mu\text{c-Si}$) with a grain size smaller than 20 nm [9,10]. They undoubtedly indicate the nanocrystalline structure of the porous layer. However, a detailed discussion of the depth evolution of the Raman scattering should include at least two additional factors: the first concerns the minor but not insignificant c-Si-like component present in spectrum (b). This scattering can be considered as the signature of large crystallites surviving the electrochemical etching process within the porous layer, far from the substratum. The second point concerns the presence of extra-scattering in the region below 500 cm^{-1} (spectra (a) and (b)). The spectral characteristics of this excess scattering correlate well with the Raman spectrum of a-Si, which shows a broad symmetric band centered at about 480 cm^{-1} [11].

4. Discussion

To derive more quantitative information about the occurrence of structural inhomogeneities and the relative abundance of the different components throughout the porous layer, the different micro-Raman spectra were analyzed in terms of specific contributions from amorphous (a-Si) and nanocrystalline (nc-Si) phases. To achieve this a Gaussian line, centered at 470 cm^{-1} with a FWHM of 55 cm^{-1} , was used for the a-Si component. The scattering contribution from the nc-Si component was evalu-

ated using a phenomenological model based on the spatial confinement of phonons.

Phonon confinement models to account for the experimental observations for $\mu\text{c-Si}$ films were developed during the 1980s [12,13]. Through a detailed analysis of the first order Raman scattering, they provide the size and the shape of the crystalline grains. These models assume a homogeneous size-distribution for the crystallites, but a more realistic approach would adopt an inhomogeneous distribution of the nanocrystal sizes. In this way, the observed spectral intensity can be fitted as a function of the crystallite size, L , through the following relationship, recently introduced by dos Santos and Torriani [14] to model Raman spectra from $\mu\text{c-Ge}$ films:

$$I(\omega) \propto \int_0^\infty I_L(\omega) P(L) dL, \quad (1)$$

where $I_L(\omega)$ is the first-order Raman scattering from phonons confined within nanocrystals with size L , as calculated by Campbell and Fauchet [13], and $P(L)$ is the crystallite size distribution function, i.e., a Gaussian distribution curve around the mean value, L_0 , with a dispersion, σ . Very good fits to the present experimental Raman spectra were obtained both by assuming a Gaussian curve as the weighting function for the phonon confinement within the nanocrystals [13] and by considering that the p-Si structure consists of spherical nanocrystallites. This approximation is supported by the results of an accurate analysis of the Raman scattering from strongly emitting p-Si films, which provided clear indications that the local structure in p-Si is more like a sphere than a rod [15].

The results of the above fitting procedure are shown in Fig. 2, where the experimental Raman spectra obtained from two different depths within the porous layer (noisy continuous lines) and their best fits (circles) are plotted together with the different components (dashed lines). Here, the background signal, mainly due to p-Si luminescence, is accounted for by a constant straight line. The fitting parameters for both the a-Si and the nc-Si components are reported in Table 1.

The analysis of the Raman scattering profile for aged p-Si layers indicates the presence at any depth of a predominant nc-Si component together with an a-Si phase. No similar evidence for such an amor-

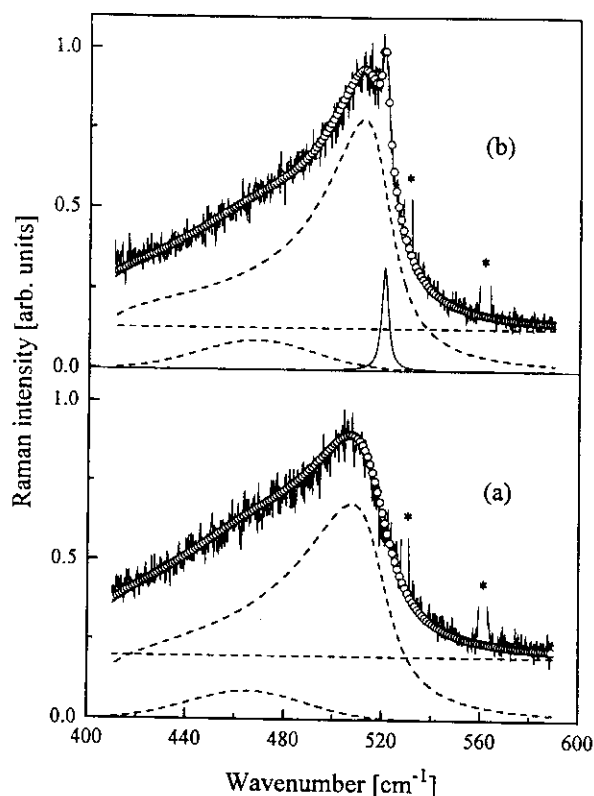


Fig. 2. Experimental Raman spectra ((a) and (b) of Fig. 1) and their best fits (circles). The details of the fitting procedure are described in the text and the parameters are given in Table 1. The different spectral components are also plotted (dashed lines), including the luminescence background in terms of a constant straight line. The asterisks (*) label the positions of the plasma lines used as energy standards. Finally, the Lorentzian curve (continuous line) used to fit of the c-Si-like component occurring in the spectrum near the bulk (top panel) is peaked at 520.4 cm^{-1} with a FWHM of 3.4 cm^{-1} .

Table 1

Parameters used to interpolate the Raman spectra of Fig. 2. (Amorphous silicon (a-Si) component, peak position, ω_0 and FWHM, Γ ; nanocrystalline silicon (nc-Si) component, mean size of crystallites, L_0 , and crystallite size dispersion, σ .) The integrated-intensity ratio of Raman scattering between the a-Si and the nc-Si components is assumed to be a measure of the relative abundance of these phases

Spectrum	a-Si		nc-Si		Intensity ratio (%)
	ω_0 (cm^{-1})	Γ (cm^{-1})	L_0 (nm)	σ (nm)	
near substrate	470 ± 6	55 ± 10	6.5 ± 0.7	2.2 ± 0.3	9.5 ± 0.5
near vacuum	470 ± 6	55 ± 10	4.5 ± 0.5	1.6 ± 0.2	10.4 ± 0.5

phous component was reported for n-type p-Si, where only a top layer, identified as containing silicon and oxygen, has been observed by energy dispersion spectroscopy [7]. The results of the present analysis show a remarkable reduction in the characteristic sizes of the nanocrystals, of the order of 30%, when the probe laser spot approaches the surface region near the vacuum, where a comparatively negligible increase of the a-Si component is found. In this case, however, the a-Si phase seems to be less abundant than that detected by Perez et al. [3].

5. Conclusions

In this paper high spatial resolution Raman spectroscopy has been used to gain insights concerning the structure of thick p-Si layers, obtained from p-type Si wafers, with regard to both the phases present and the characteristic sizes of the nanocrystallites. The results indicate that an a-Si component is present at any depth within the cross-section of the porous layers, in addition to the predominant nanocrystalline phase. The depth dependence of the nanocrystals size has been analyzed using a phenomenological model based on the spatial confinement of phonons. A considerable reduction of the nanocrystalline size is found from the analysis of spectra excited at the p-Si/vacuum interface, where a substantially unchanged a-Si component is present.

The authors are grateful to Professor O. Bisi and Dr L. Pavesi for many valuable discussions and helpful suggestions. They also thank Dr M. Ceschini for the preparation of the samples, and Dr. E. Zanghellini for his assistance during the measurements. One of the authors (G.M.) also acknowledges partial support from the Conselho Nacional de Desenvolvimento Científico e Tecnológico – CNPq (Brazil).

References

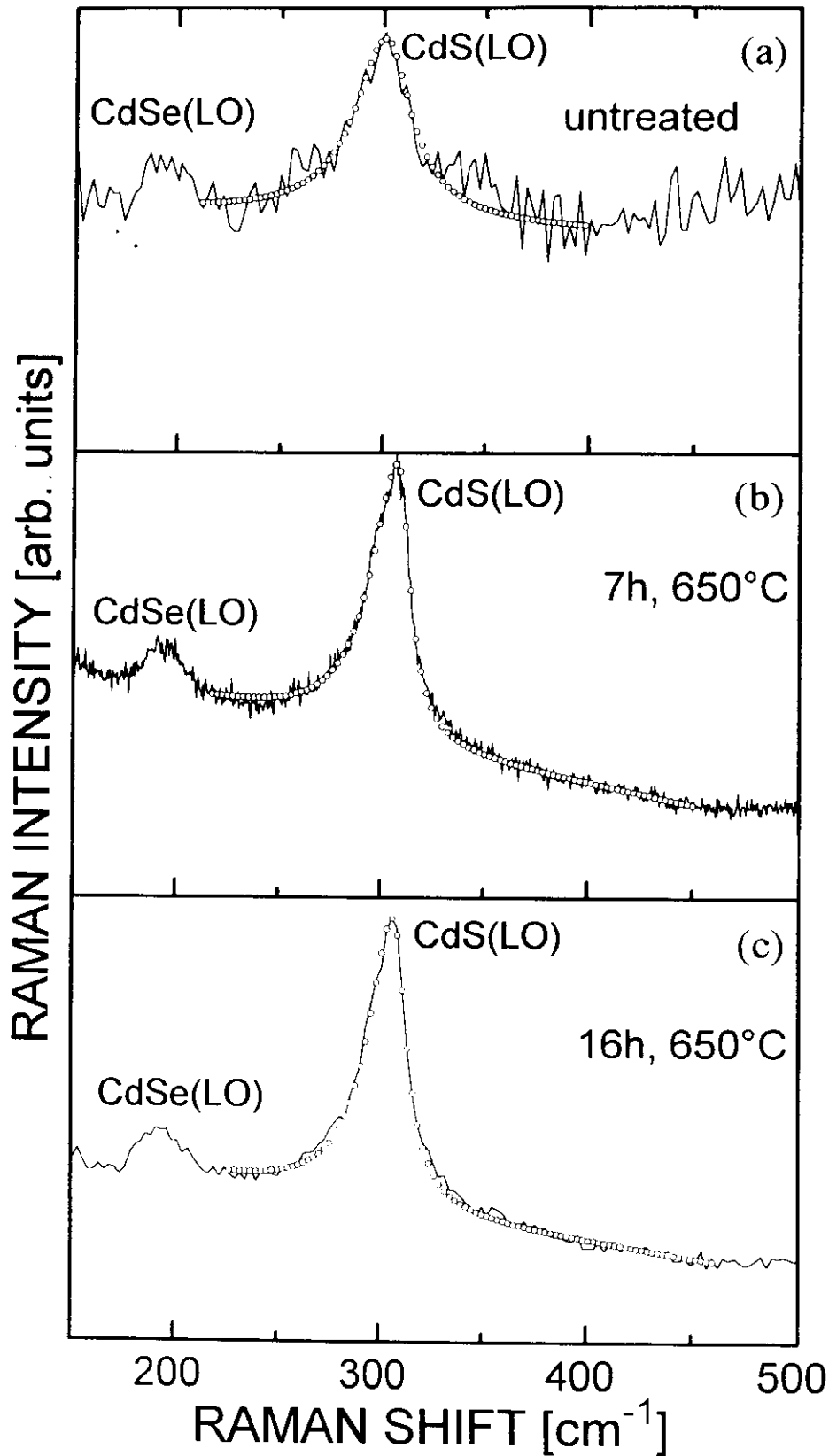
- [1] L.T. Canham, Appl. Phys. Lett. 57 (1990) 1046.
- [2] R. Tsu, H. Shen and M. Dutta, Appl. Phys. Lett. 60 (1992) 112.
- [3] J.M. Perez, J. Villalobos, P. McNeil, J. Prasad, R. Cheek, J. Kelber, J.P. Estrera, P.D. Stevens and R. Glosser, Appl. Phys. Lett. 61 (1992) 563.
- [4] D.J. Lookwood, G.C. Aers, L.B. Allard, B. Bryskiewicz, S.

- Charbonneau, D.C. Houghton, J.M. McCaffrey and A. Wang, *Can. J. Phys.* 70 (1992) 1184.
- [5] I.I. Reshina and E.G. Guk, *Semicond.* 27 (1993) 401.
- [6] K. Inoue, O. Matsuda, K. Maehashi, H. Nakashima and K. Murase, *Jpn. J. Appl. Phys.* 31 (1992) L997.
- [7] F. Kozlowski and W. Lang, *J. Appl. Phys.* 72 (1992) 5401.
- [8] L. Pavesi, M. Ceschini, G. Mariotto, E. Zanghellini, O. Bisi, M. Anderle, L. Calliari M. Fedrizzi and L. Fedrizzi, *J. Appl. Phys.* 75 (1994) 1118.
- [9] J.F. Morange, G. Kanellis and M. Balkanski, *Solid State Commun.* 32 (1979) 805.
- [10] Z. Iqbal, S. Veprek, A.P. Webb and P. Capezzuto, *Solid State Commun.* 37 (1981) 993; Z. Iqbal and S. Veprek, *J. Phys. C15* (1982) 337.
- [11] J.E. Smith Jr., M.H. Brodsky, B.L. Crowder, M.I. Natham and A. Pinczuk, *Phys. Rev. Lett.* 26 (1971) 642.
- [12] H. Richter, Z.P. Wang and L. Ley, *Solid State Commun.* 39 (1981) 625.
- [13] I.H. Campbell and P.M. Fauchet, *Solid State Commun.* 58 (1986) 739.
- [14] D.R. dos Santos and I.L. Torriani, *Solid State Commun.* 85 (1993) 307.
- [15] Z. Sui, P.P. Leong and I.P. Herman, *Appl. Phys. Lett.* 60 (1992) 2086.

INTRODUCTION

- The effects of spatial confinement of optical phonons have been widely studied by Raman spectroscopy in nanostructured crystalline semiconductors, and size-dependent shifts and broadenings of first-order Raman peak have been usually observed.
- The case of semiconductor quantum dots (Ge, Si, CdS(Se), etc.), obtained under a large variety of experimental conditions (deposition techniques and post-deposition treatments).
- In contrast to many studies focused on confined optical phonons, acoustic phonons confined in semiconductor nanostructures have been studied only occasionally because of the difficulties in carrying out significant Raman spectra in the very low-energy region down to few wavenumbers far from the Rayleigh line and the less remarkable spectral effects of spatial confinement of acoustic phonons.
- In a pioneering paper of 1986 Duval et al. have shown that very low-frequency Raman spectroscopy constitutes a very powerful technique for the study of confinement effects of acoustic phonons and a reliable tool to determine the crystal size in nanometric range for insulator and semiconductors.
- To our best knowledge, only few reports on the confinement effects of acoustic phonons have been concerned with Ge and Si quantum dots.
- The confinement effects of acoustic phonons have been studied much more successfully in metal particles, especially in silver clusters, precipitated into transparent dielectric matrices (crystals and glasses). This is favoured by the very strong enhancement of the low-frequency Raman scattering, due to resonant excitation of the visible light with the surface plasmons of the metal.

Raman scattering spectra of $\text{CdS}_x\text{Se}_{1-x}$ doped glasses after different heat-treatments showing the changes of the CdS LO phonon modes. It was concluded that the heat-treatment causes a change of the position and the width of the LO modes but no change in the composition of nanocrystals.



K.E. LIPINSKA -
KALITA, G. MAROTTA
and E. ZAMBELLI
PHIL. MAG. B 54
(1995)

RAMAN SPECTRA FROM Ge MICROCRYSTALS

N.M. DUSYUK et al., JETP LETT. 47, 298 (1988)

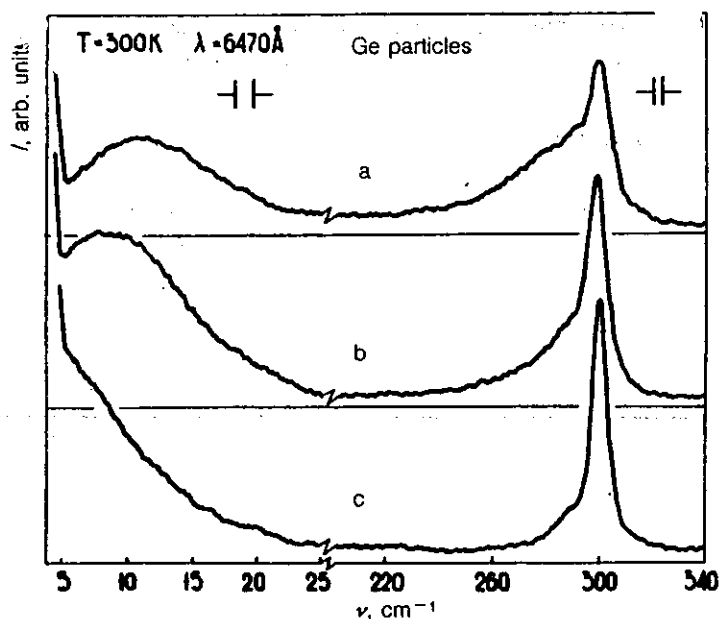


FIG. 2. Spectra of the Raman scattering by natural acoustic vibrations of Ge microscopic crystals and of the scattering by optical phonons of these crystals. d , T : a—80 Å, 320 °C; b—110 Å, 360 °C; c—300 Å, 500 °C. The substrate is silicon.

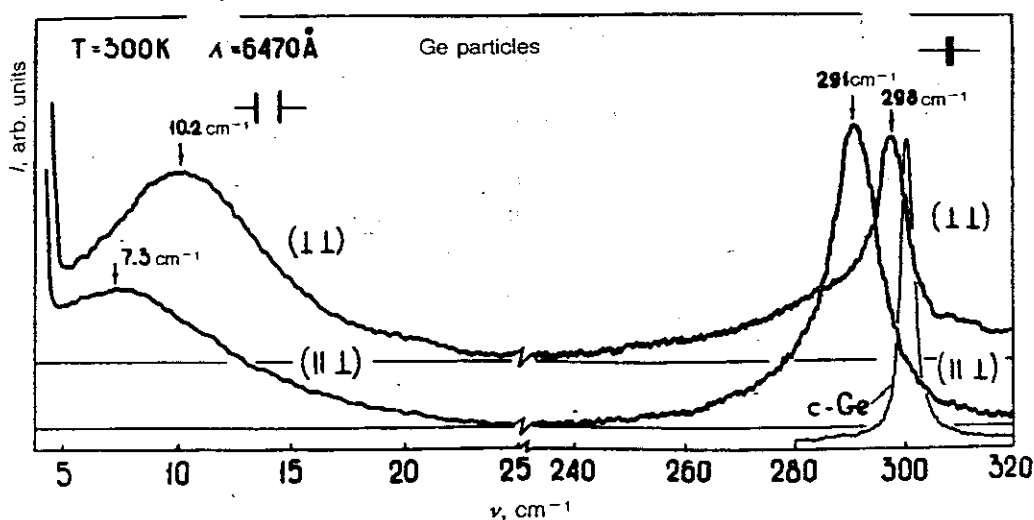


FIG. 3. Polarization dependence of the Raman spectra of Ge single crystals. $d = 130$ Å, $T_s = 380$ °C, fused quartz substrate. Shown for comparison is the spectrum of the Raman scattering by a mixed $LO-TO$ phonon in crystalline Ge.

RAMAN SCATTERING FROM ACOUSTIC PHONONS CONFINED IN SILICON NANOCRYSTALS

M. FUJII et al.
P.R. B54, R8373
(1996)

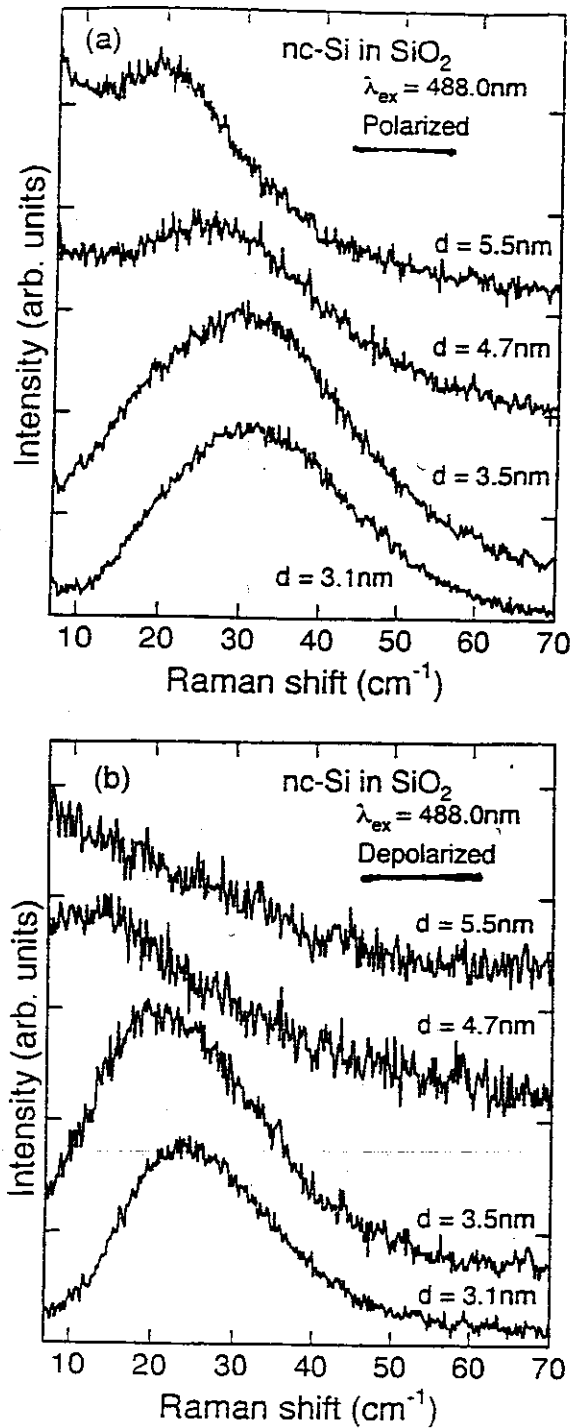
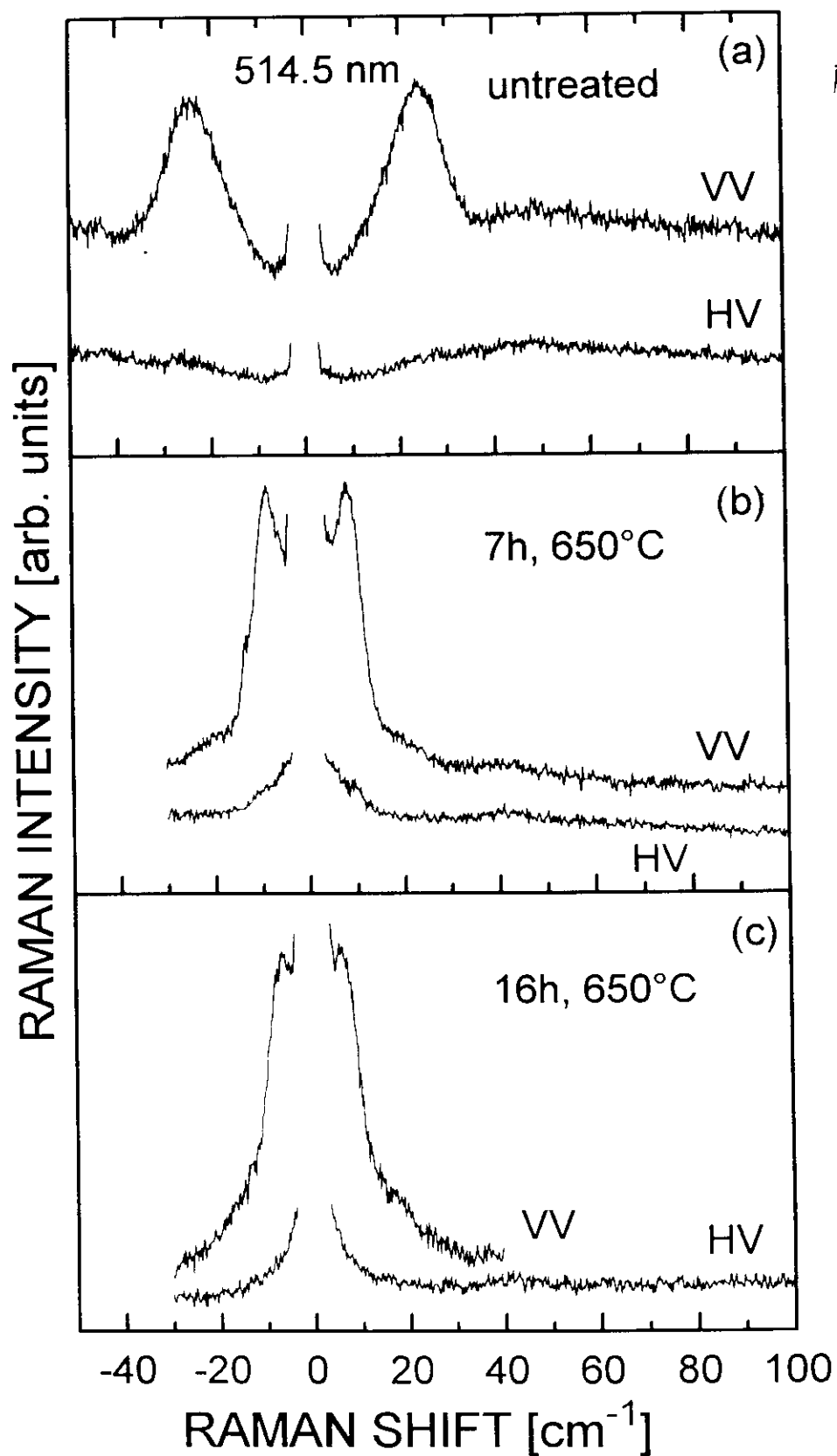


FIG. 2. Size dependence of (a) polarized and (b) depolarized Raman spectra of Si nanocrystals embedded in SiO_2 matrices.

Stokes- and anti-Stokes low-frequency Raman scattering of $\text{CdS}_x\text{Se}_{1-x}$ doped glasses after different heat-treatments. The latter led to different nanocrystallite diameters (ϕ). The excitation line was 514.5 nm.



K E. LIPINSKA -
KALITA et al
PHIL. MAG. B 71,
547 (1995)

Optical properties of metal colloid composites

Both linear and non-linear optical properties of metal colloid-containing composites are usually described by the Mie theory, developed for small, non-interacting spherical particles into a transparent dielectric medium.

The linear response of composite systems containing metal colloids with diameter $< \lambda/20$ (λ = wavelength of light) is given in terms of the absorption coefficient α :

$$\alpha(\omega) = (18 \pi n_d^3 / \lambda) \cdot p \epsilon_2 / [(\epsilon_1 + 2n_d^2)^2 + \epsilon_2^2]$$

where:

$\epsilon(\omega) = \epsilon_1 + i\epsilon_2$ is the dielectric function of metal colloids;

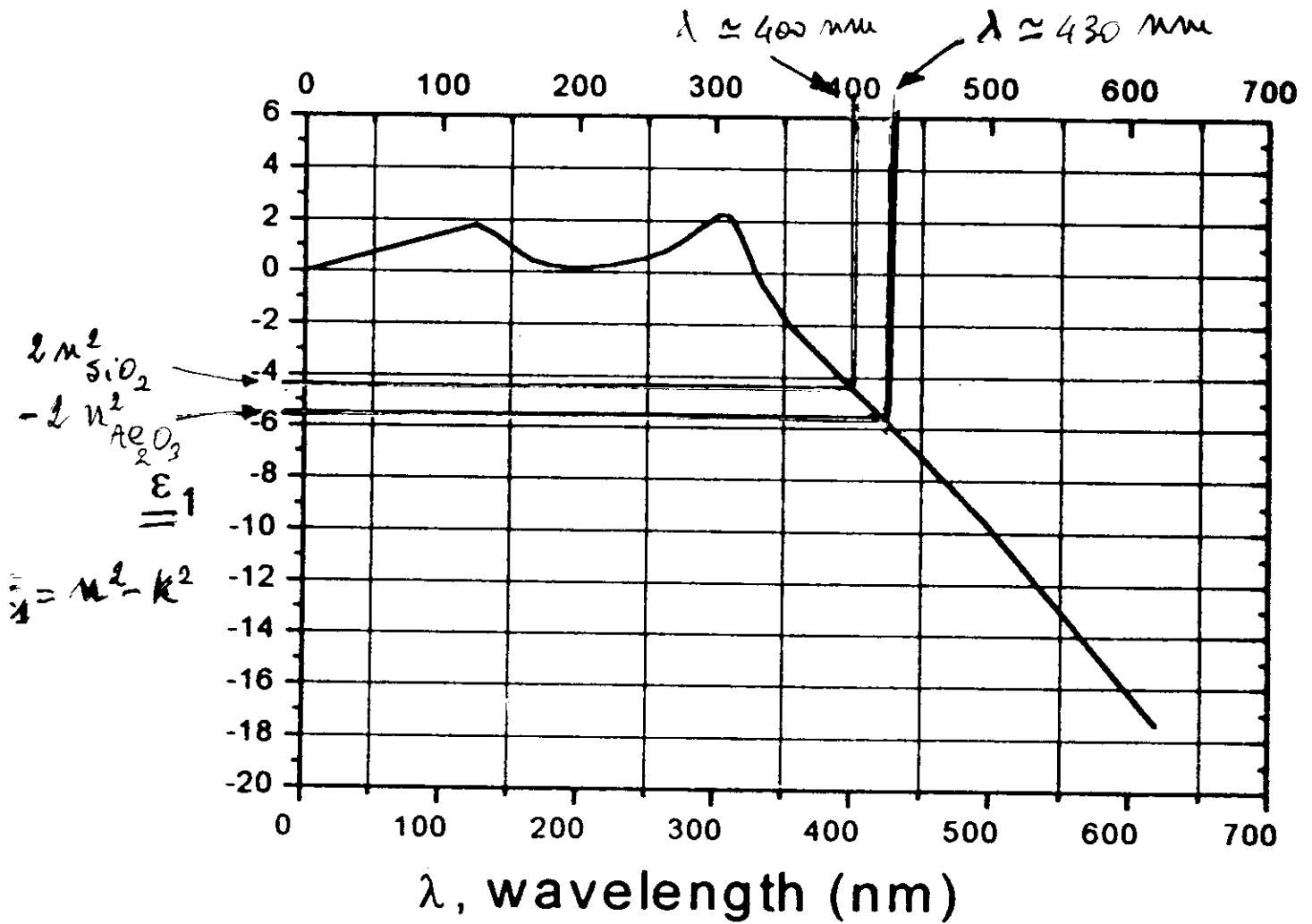
p is fractional volume occupied of the metal particles;

n_d is the refraction index of the dielectric host.

The absorption spectrum is expected to exhibit a peak at the surface plasmon resonance frequency ω_{sp} , where:

$$\epsilon_1(\omega_{sp}) + 2 n_d^2 = 0$$

SURFACE PLASMON RESONANCE ENERGY OF Ag CLUSTERS IN V-SiO₂ AND α -Al₂O₃



Value of ϵ_1 for bulk Ag as a function of photon wavelength (nm)

$$\rightarrow \boxed{\epsilon_1(\omega_{sp}) + \epsilon_d = 0}$$

$$\epsilon(\omega) = \epsilon_1(\omega) + i\epsilon_2(\omega)$$

$$\epsilon_1 = n^2 - k^2 \quad \epsilon_2 = 2nk$$

Ag in	n_d	λ_{sp} (nm)	E (eV)
SiO ₂	1.49	~ 400	~ 3.1
Al ₂ O ₃	1.66	~ 430	~ 2.9

Synthesis of metal clusters

Some of the experimental methods currently used are:

- Doping of melted dielectric matrices with a proper metal in small percents (the most ancient method used to color the glasses, since several centuries);
- Vapour deposition (metal gas-phase evaporation and deposition on the dielectric substrate);
- Sputtering deposition (metal bombardment by energetic ion beams with metal atoms sputtering and deposition over the substrate);
- Co-sputtering deposition (both metal and dielectric materials are bombarded, with simultaneous formation of the composite material consisting metal nanoclusters embedded into the dielectric matrix).

Metal cluster fabrication by ion implantation

Several experimental methods are currently exploited to synthesize metal colloids in transparent dielectric matrices.

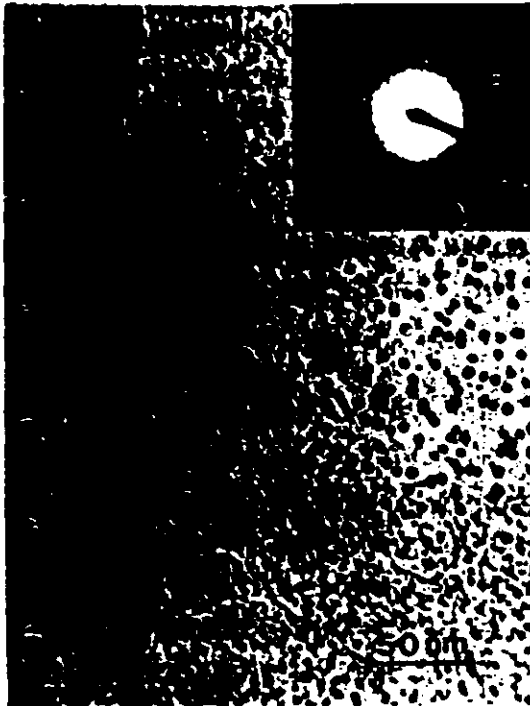
Ion implantation provides a suitable route for the fabrication of quantum structures either in glasses and in crystalline substrates.

Nanoclusters of noble metals (Cu, Ag and Au) can be precipitated in fused silica (v-SiO_2) as well as in sapphire ($\alpha\text{-Al}_2\text{O}_3$) by ion implantation.

Typical experimental conditions:

- Ion beam energy in the range of 0.1 - 1 MeV;
- = Implanted doses from 10^{16} to 10^{17} ion/cm².

TEM MICROGRAPH

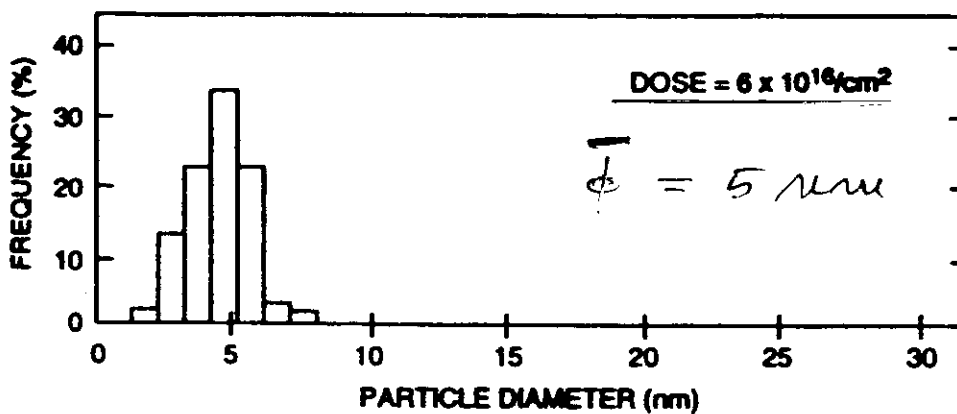
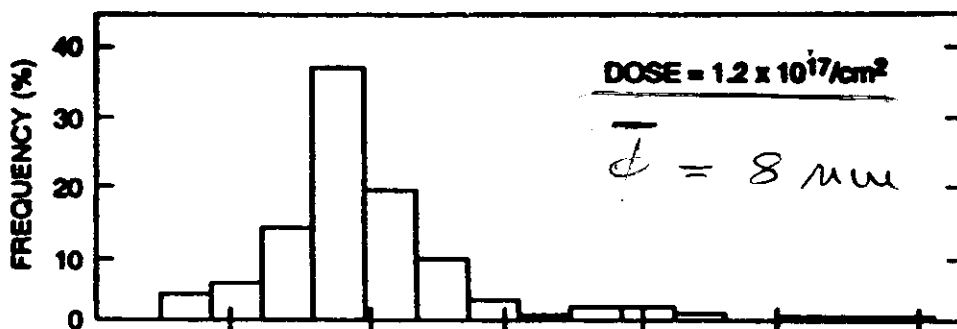


Ag CLUSTERS
IN $v\text{-SiO}_2$

1.8 MeV
 $1.6 \times 10^{16} \text{ cm}^{-2}$

50 nm

SIZE DISTRIBUTION OF Ag CLUSTERS



Advantages and limits of ion implantation

- + Good control of the colloid precipitation process (depth within the substrate, particle size and size distribution) obtained by varying the implantation parameters (energy, current density and implanted dose), and the substrate temperature during the ion implantation.
- + Metal composites made by ion implantation have much higher metal clusters concentrations than in melt glass composites, and exhibit effective nonlinear susceptibilities $\chi_{\text{eff}}^{(3)}$ up to several hundred times larger than those of materials obtained by conventional methods.
- Radiation damage: the number of ions at the substrate surface is of the order of 10^{16} ion/cm², this causes a substantial bond breaking and the formation of defects either at the surface or within the implanted layer.
- Some of the produced defects are optically active and, therefore, they may have detrimental effects on the performances of optical devices.

Sample preparation

Commercial samples of sapphire (Meller Optics) and of fused silica (Hereus) were cut in rectangular platelets (typical dimensions $5 \times 5 \text{ mm}^2$).

Ion implantation was carried out at room temperature with 300 KeV- Ag^+ in Porto Alegre.

Current density was of $1 \text{ }\mu\text{A}/\text{cm}^2$, in order to restrict the thermal effects during the implantation.

Ion fluences ranged between 1 to $10 \times 10^{16} \text{ ion}/\text{cm}^2$.

Two different sets of samples (one for each substrate) were prepared, and no post-implantation treatment was carried out on them.

As-implanted samples showed a clear coloration even at low implanted doses, and this fact provides the first evidence of Ag-colloid precipitation in both substrates.

Experimental methods

All measurements were done in air at room temperature.

Rutherford Backscattering Spectrometry (RBS)

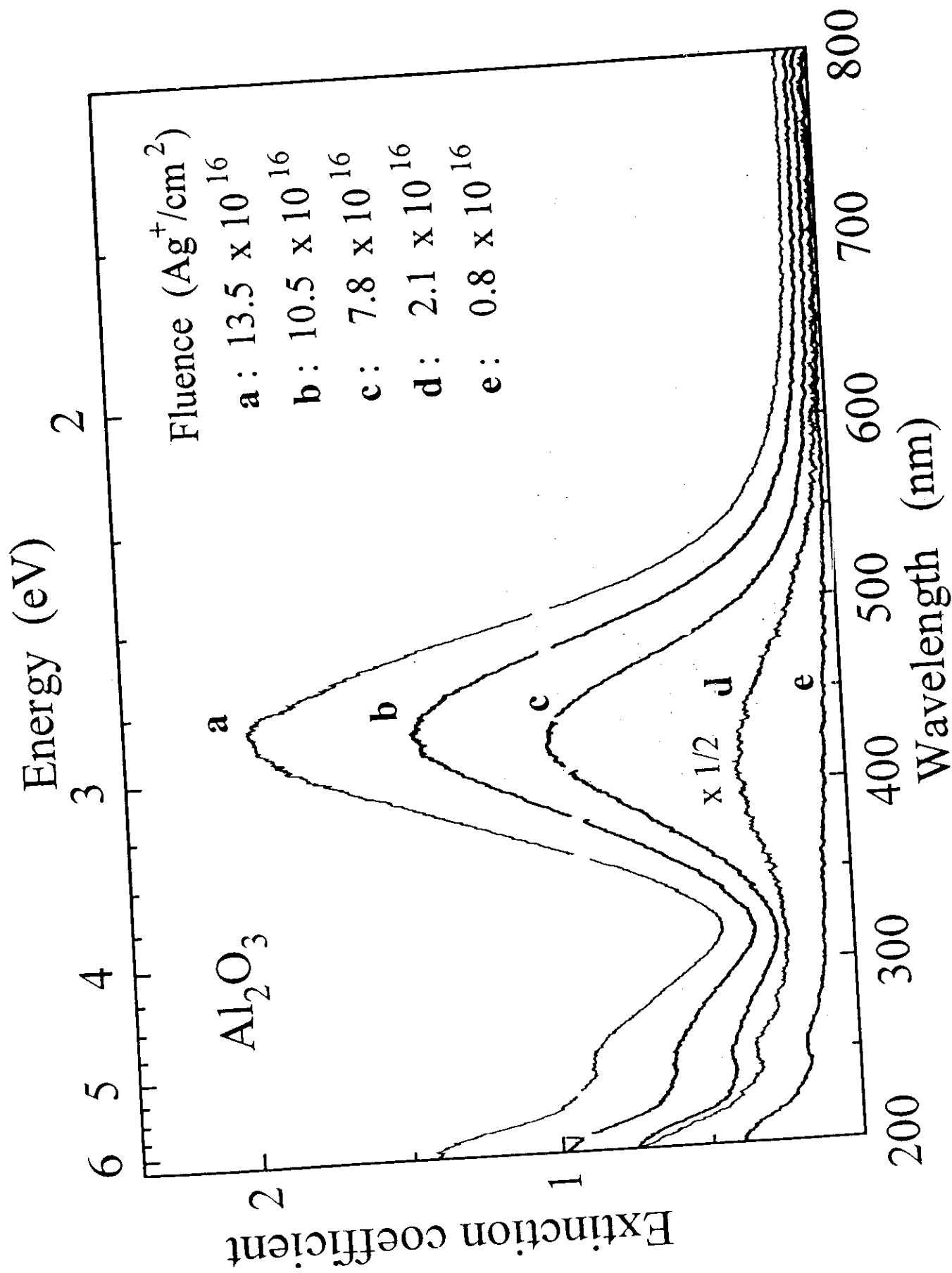
RBS analyses were performed at PUC-RIO using 2.0 MeV-He²⁺ particles and the scattering angle was 165°.

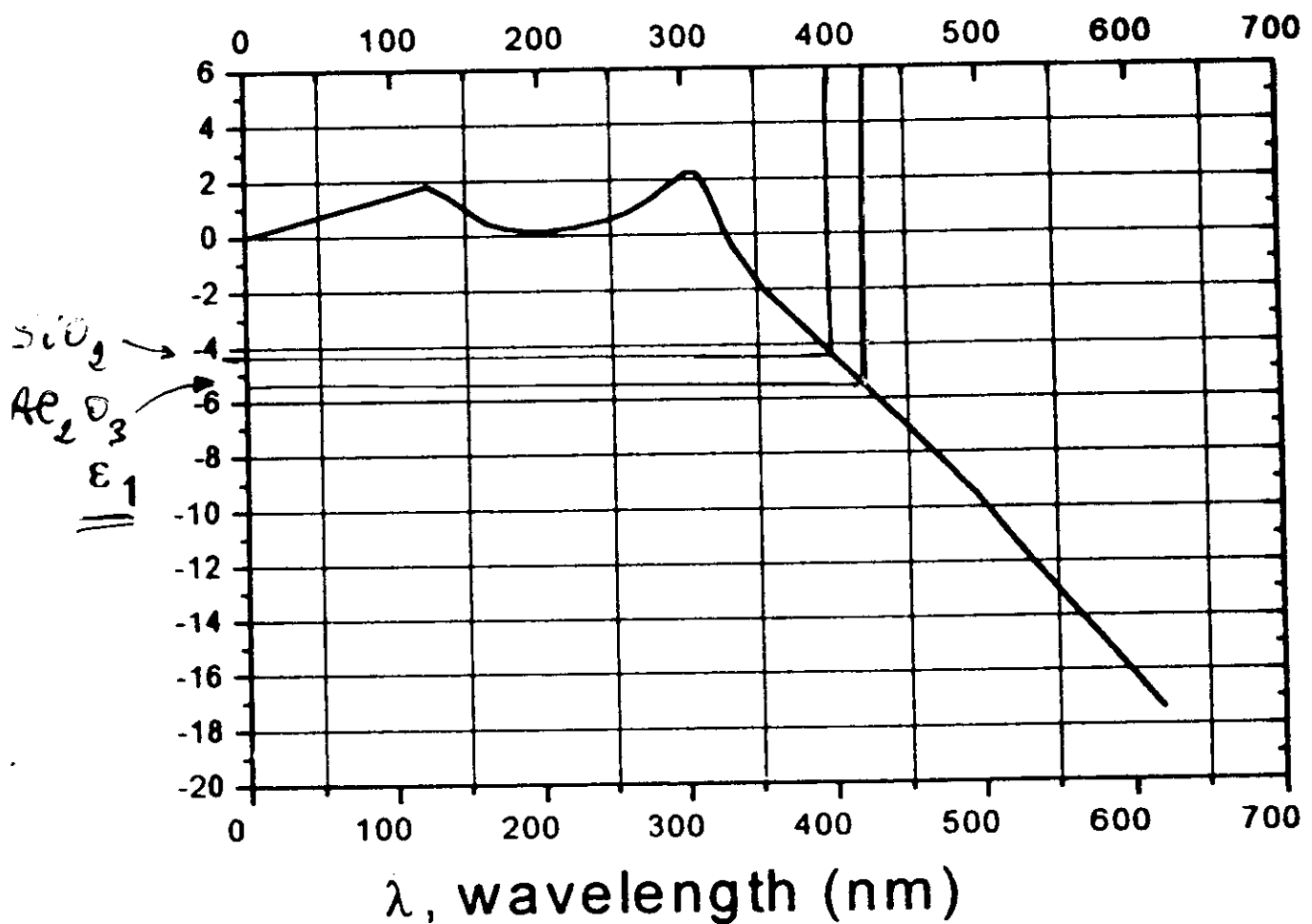
Optical Absorption Spectroscopy (OAS)

Optical absorption spectra in the range 200 - 900 nm were recorded with a double beam spectrophotometer (Cary 14). A virgin sample was used as reference.

Raman scattering spectroscopy (RSS)

Low-frequency Raman scattering spectra were carried out at 90° using a standard equipment consisting of a 1 meter focal-length double-monochromator (Jobin-Yvon, mod. Ramanor HG2-S), equipped with holographic gratings (2000 lines/mm) and a cooled photon counting system was employed to detect the filtered radiation.





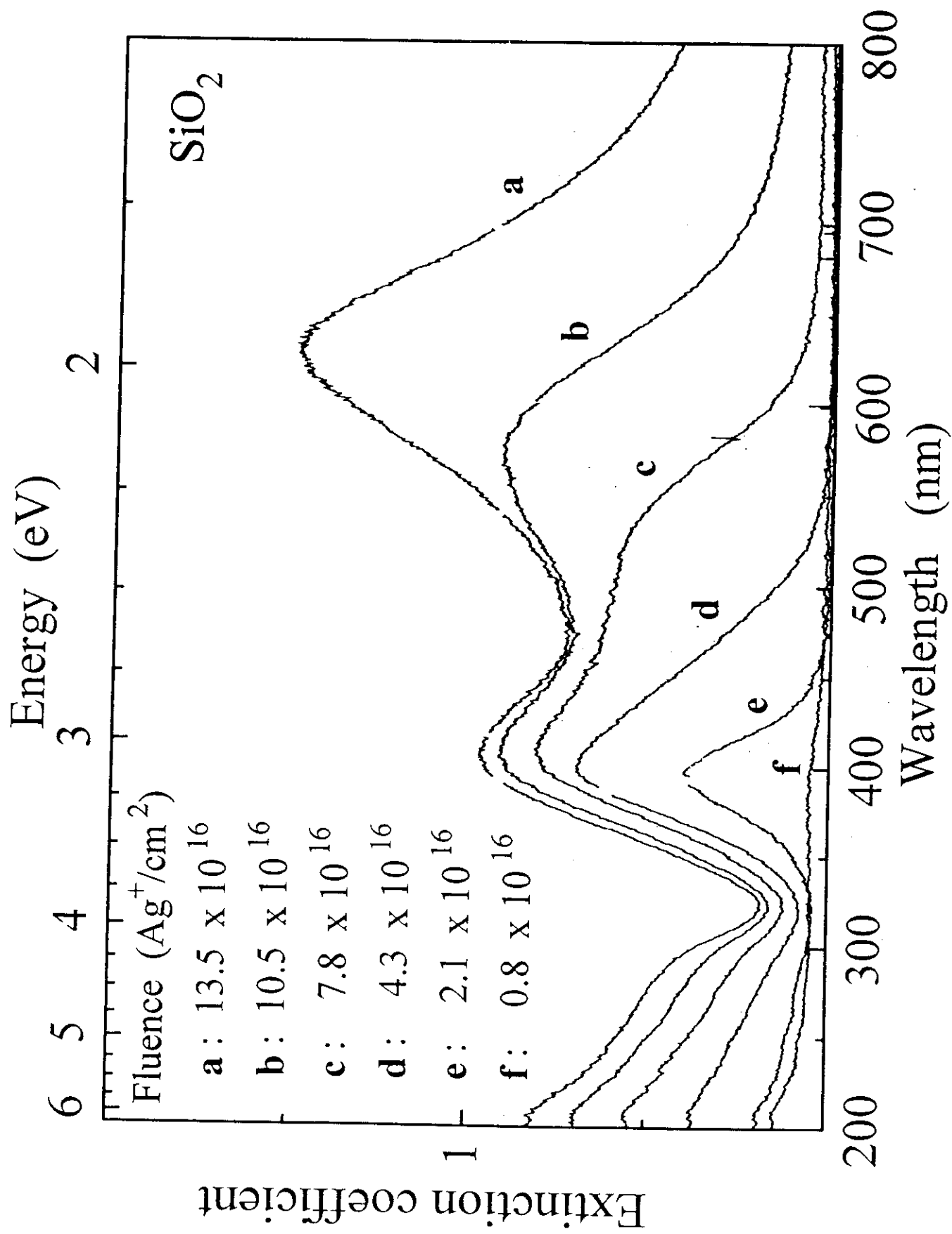
Value of ϵ_1 for bulk Ag as a function of photon wavelength (nm)

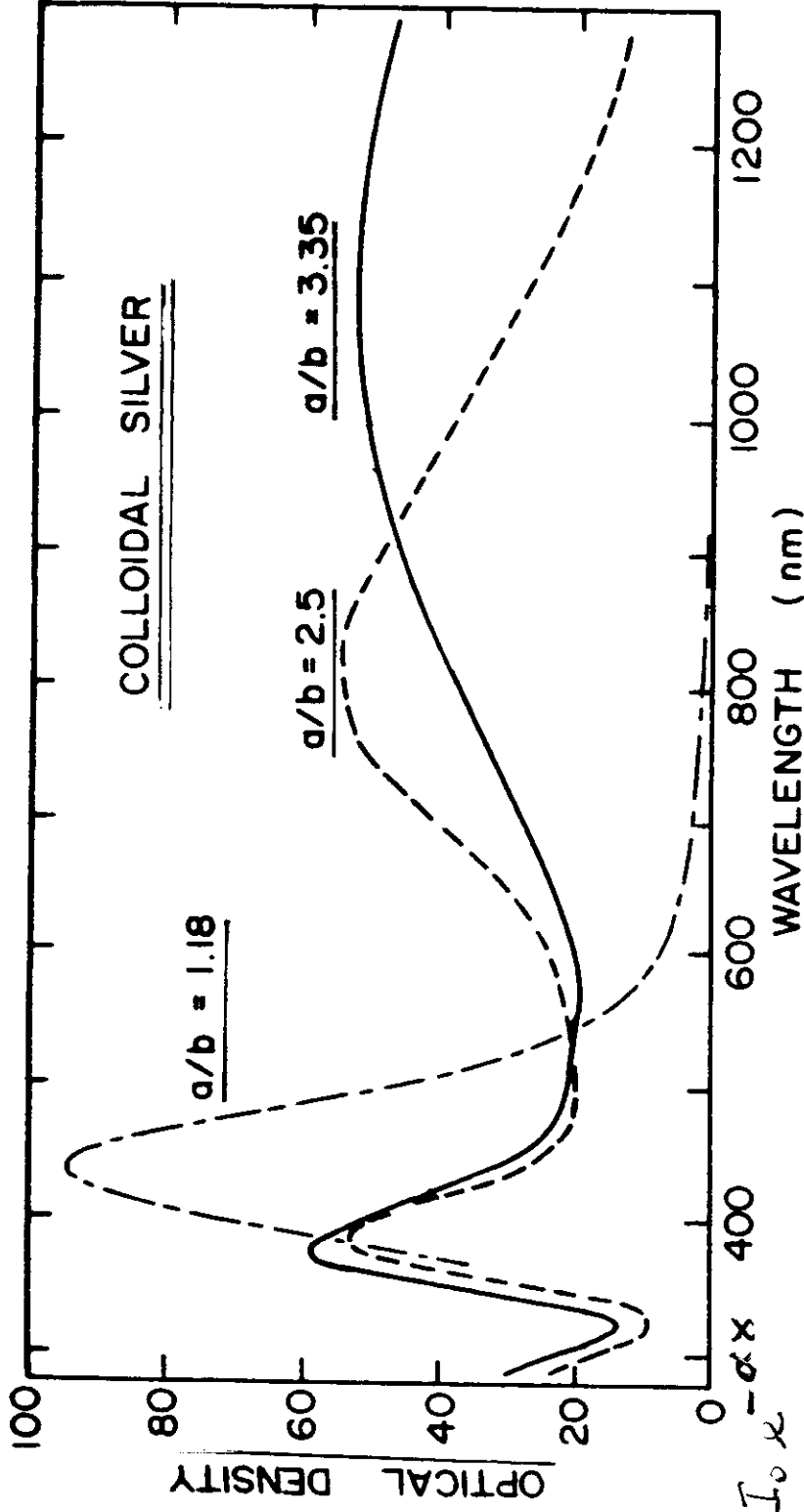
$$\lambda_{sp}(\text{SiO}_2) \approx 400 \text{ nm}$$

$$\lambda_{sp}(\text{Al}_2\text{O}_3) \approx 430 \text{ nm}$$

$$\alpha(\omega) = \frac{18\pi}{\lambda} \cdot n_d^3 \cdot \underline{\underline{p}} \cdot \frac{\epsilon_2}{(\epsilon_1 + 2n_d)^2 + \epsilon_2^2}$$

$$\underline{\underline{\alpha(\omega) \propto p}}$$



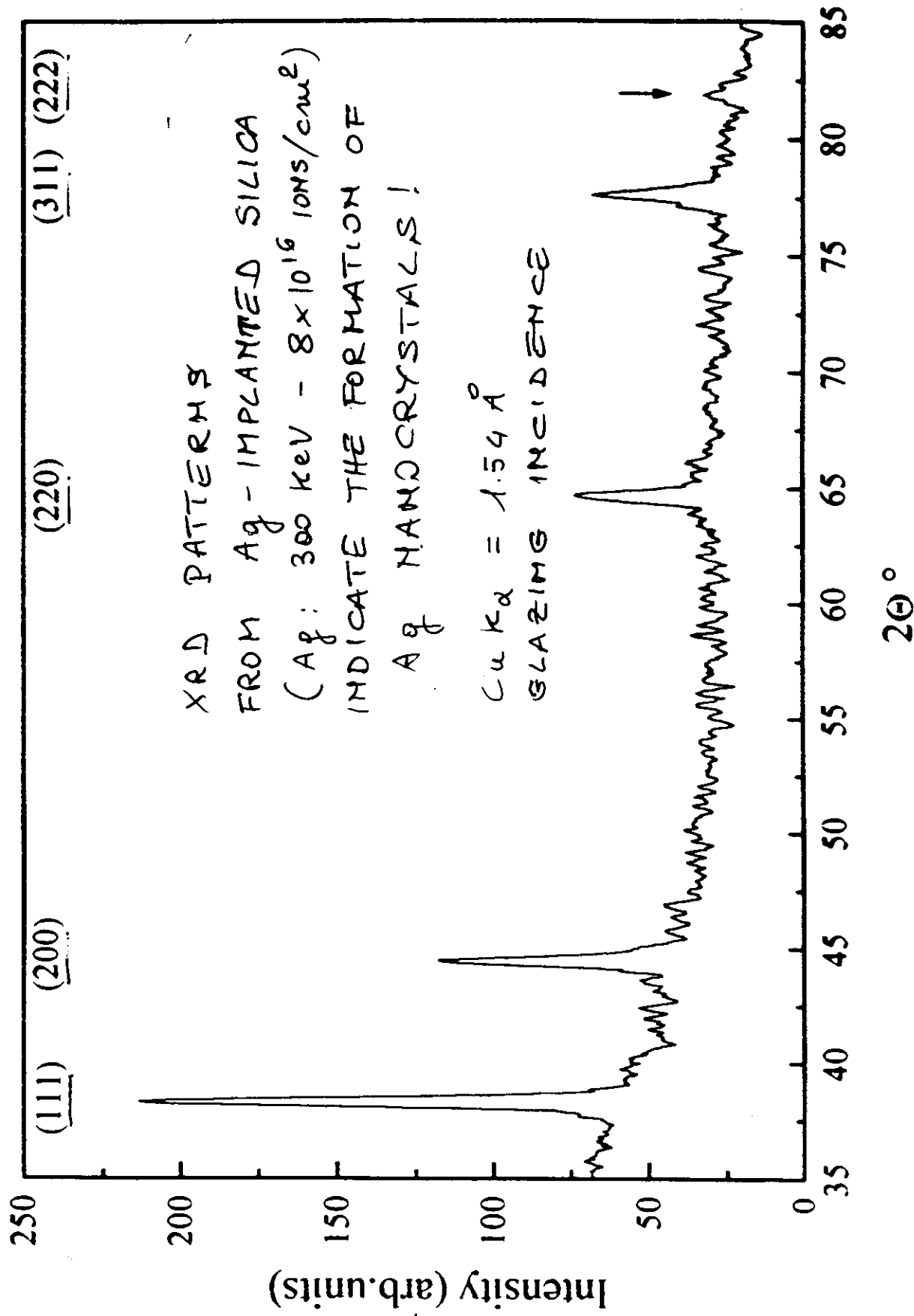


- $I(x) = I_0 e^{-\alpha x}$
- $O.D. = \alpha \times \log e$

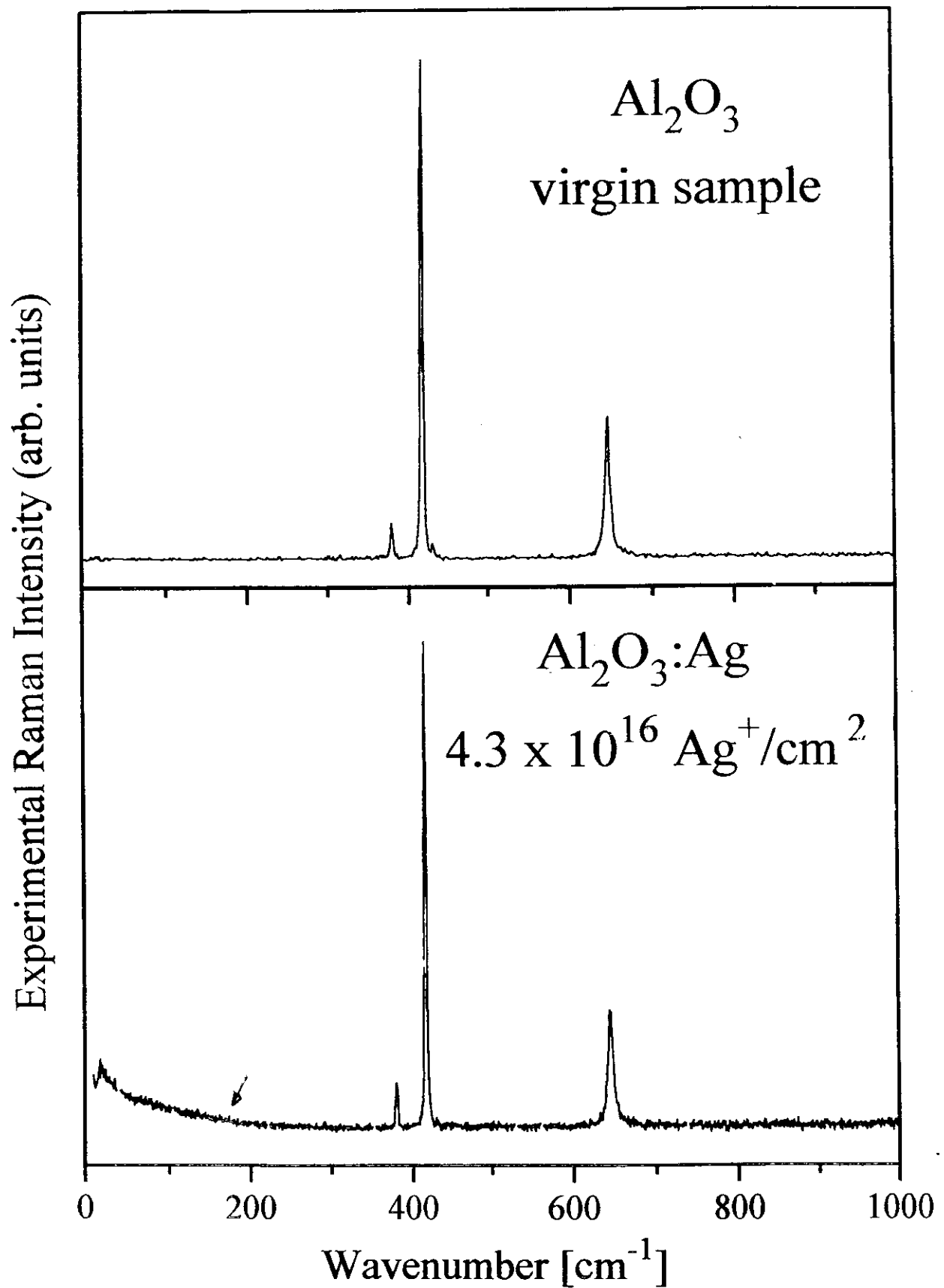
ABSORPTION SPECTRUM OF Ag CLUSTERS

WITH NON-SPHERICAL SHAPE

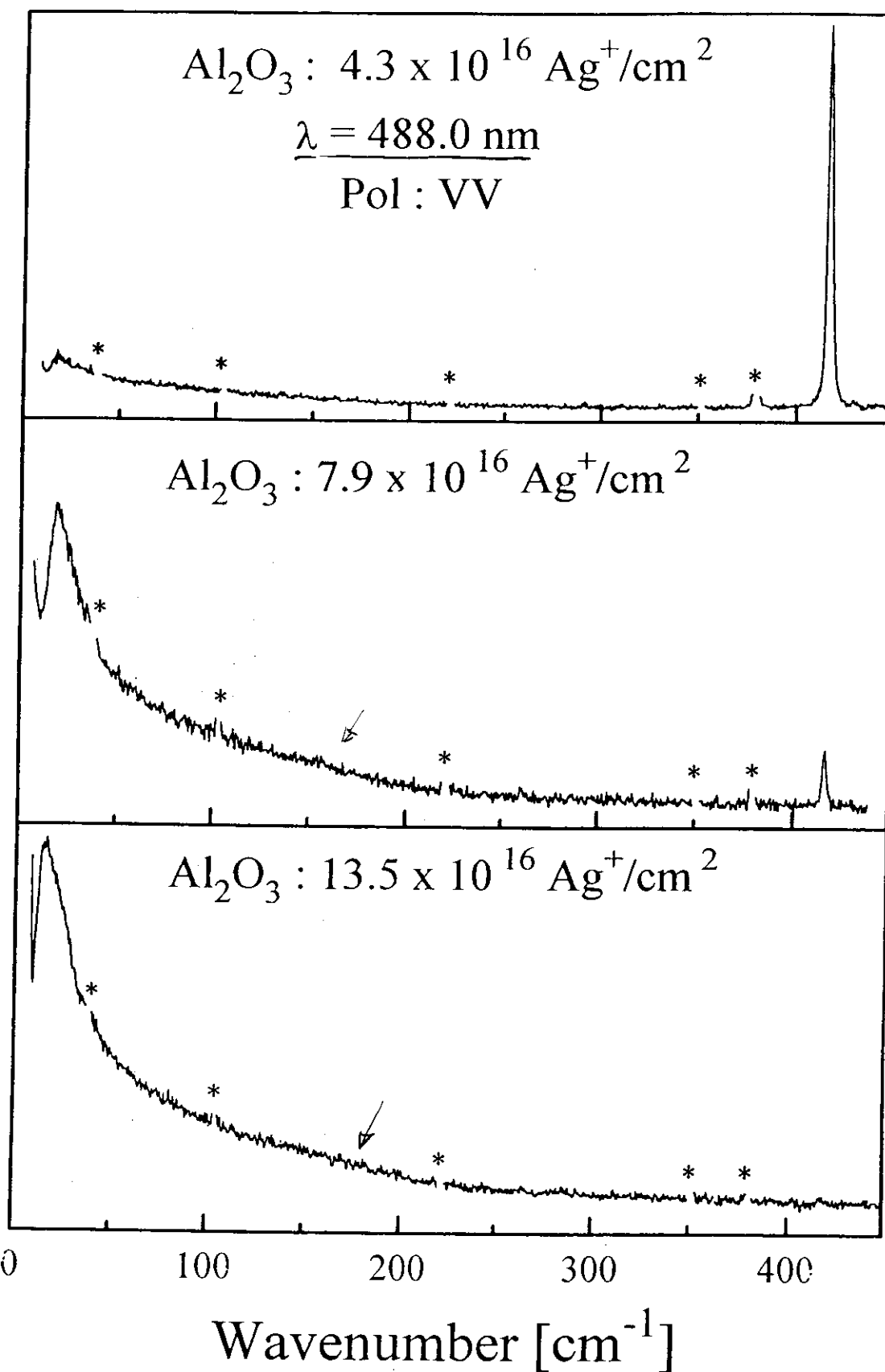
- ASPECT RATIO : $\frac{a}{b}$



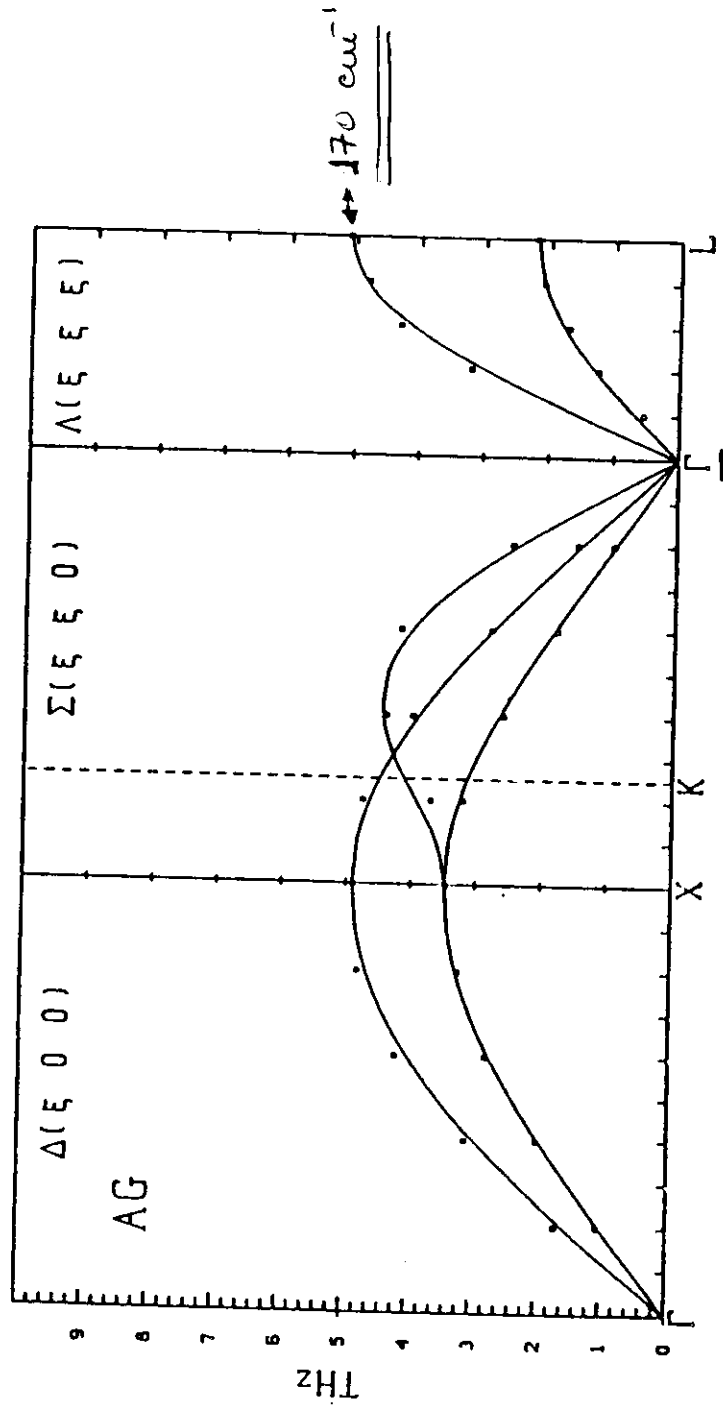
RAMAN SPECTROSCOPY ON $\text{Al}_2\text{O}_3:\text{Ag}$



Experimental Raman intensity [arb. units]



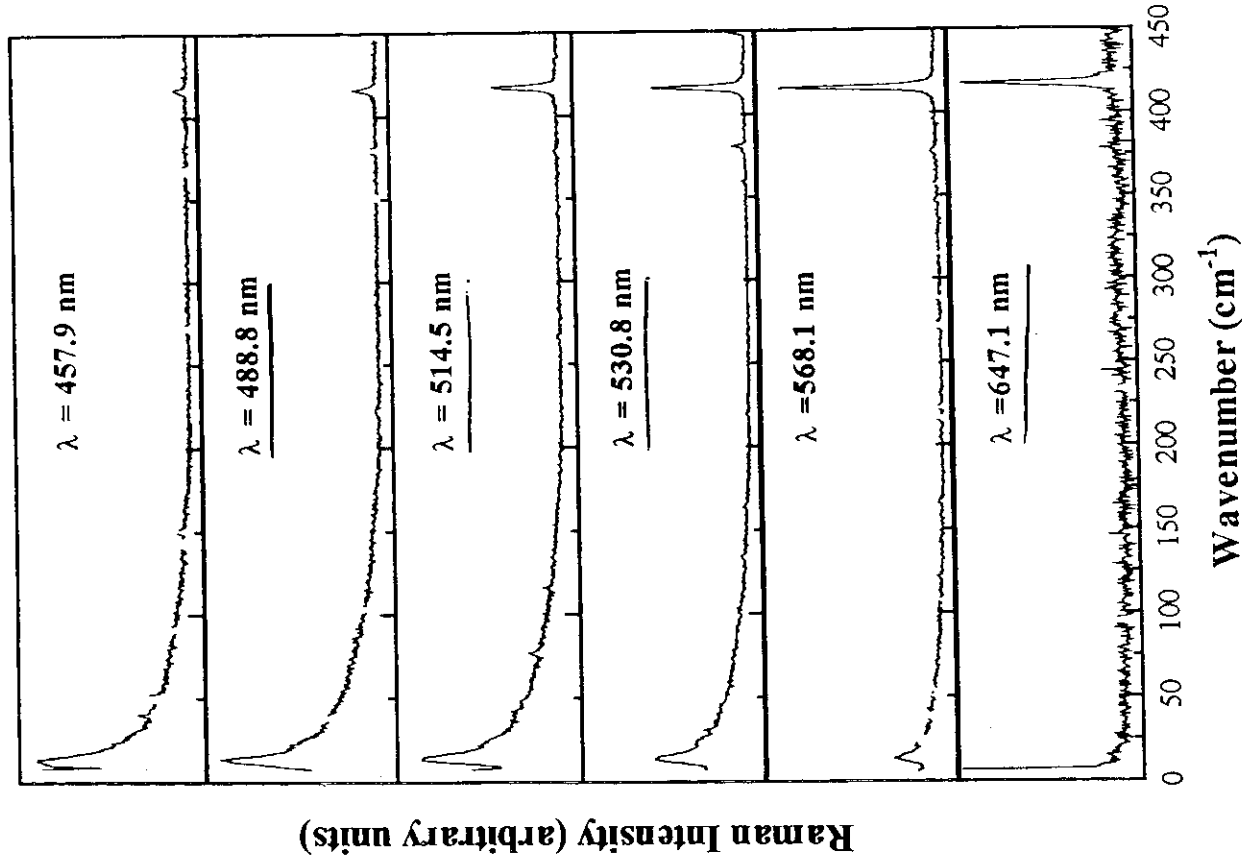
A_g DISPERSION CURVES (CALCULATED)



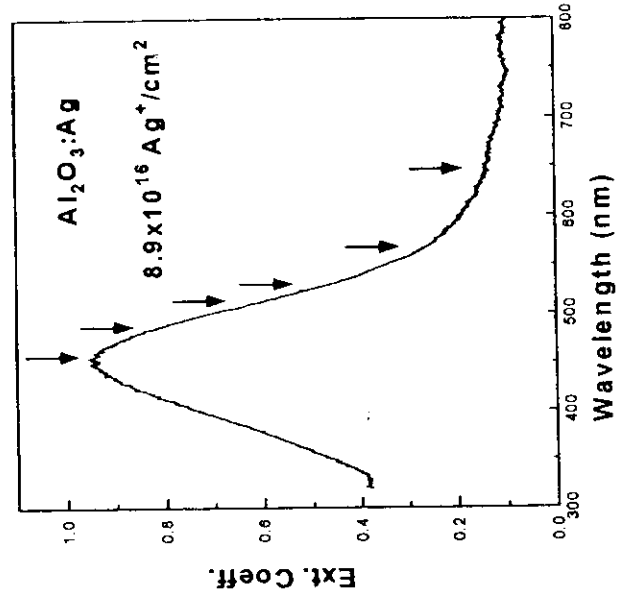
CURVE OF DISPERSIONS FROM N. A. KRESS, W. KRESS (1985)

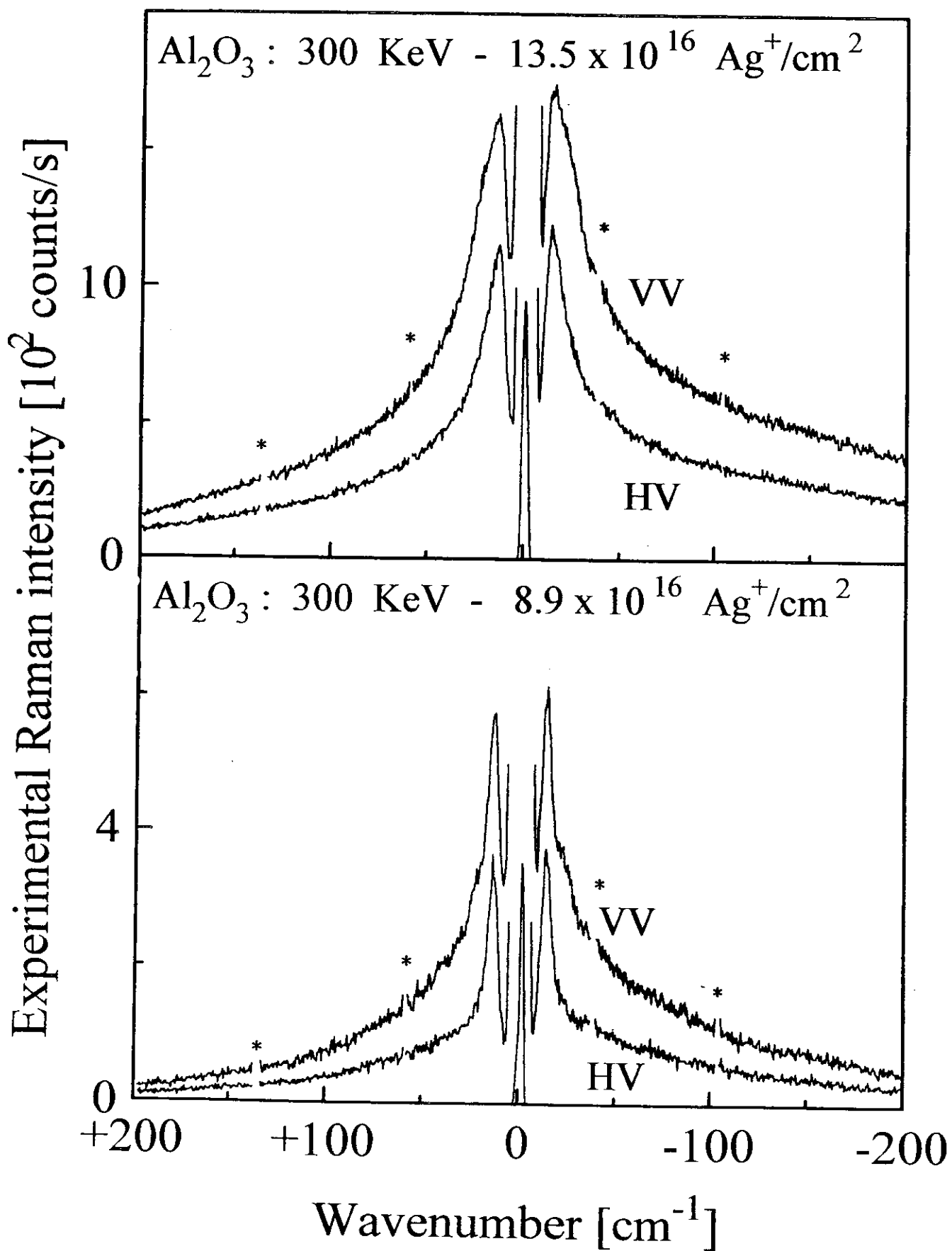
• C.S. JAYANTHI, H. BILZ, W. KRESS (1985)

$\text{Al}_2\text{O}_3 : 8.9 \times 10^{16} \text{ Ag}^+/\text{cm}^2$

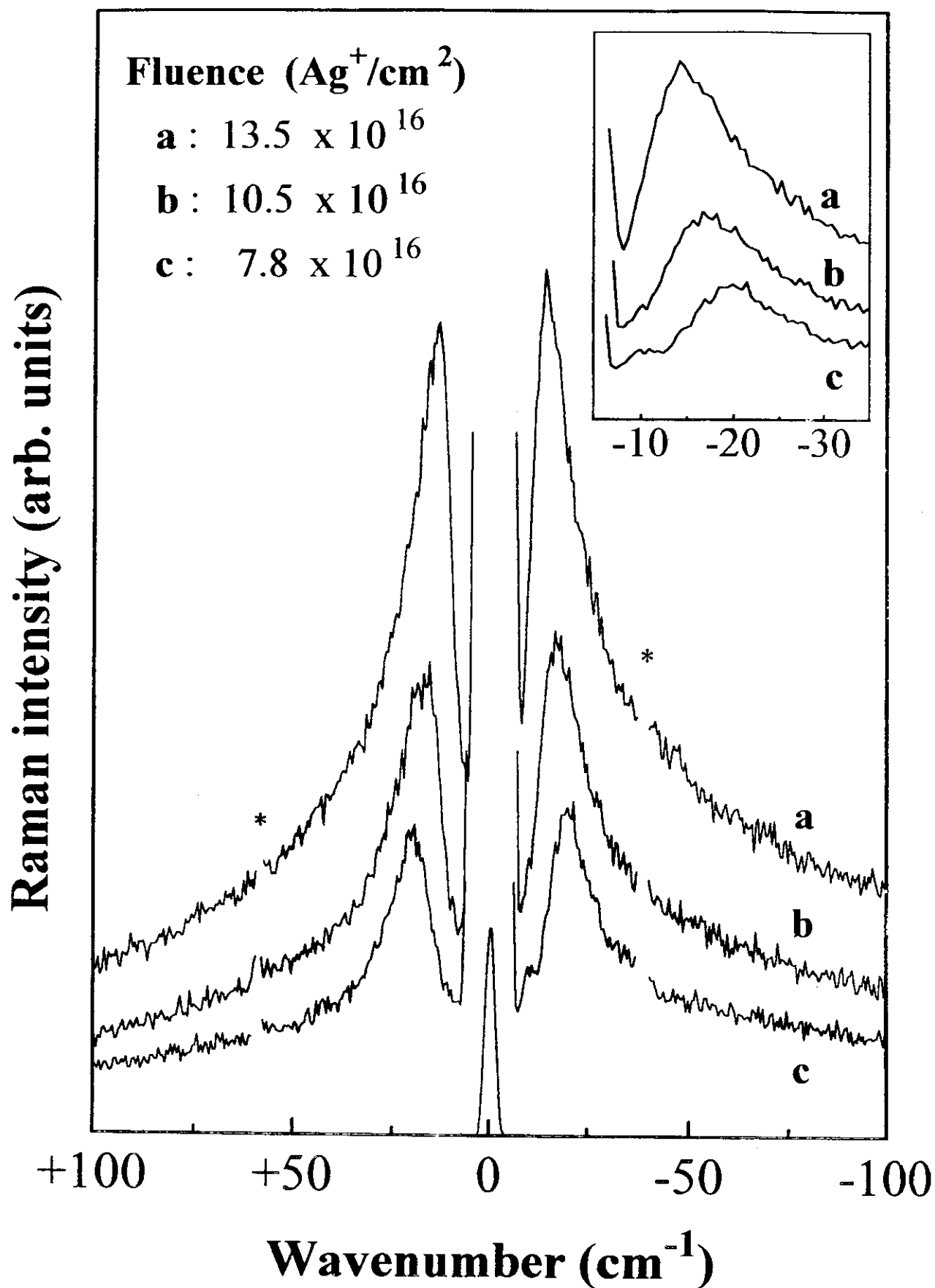


CARATTERE RISONANTE
DEL LOFIRS



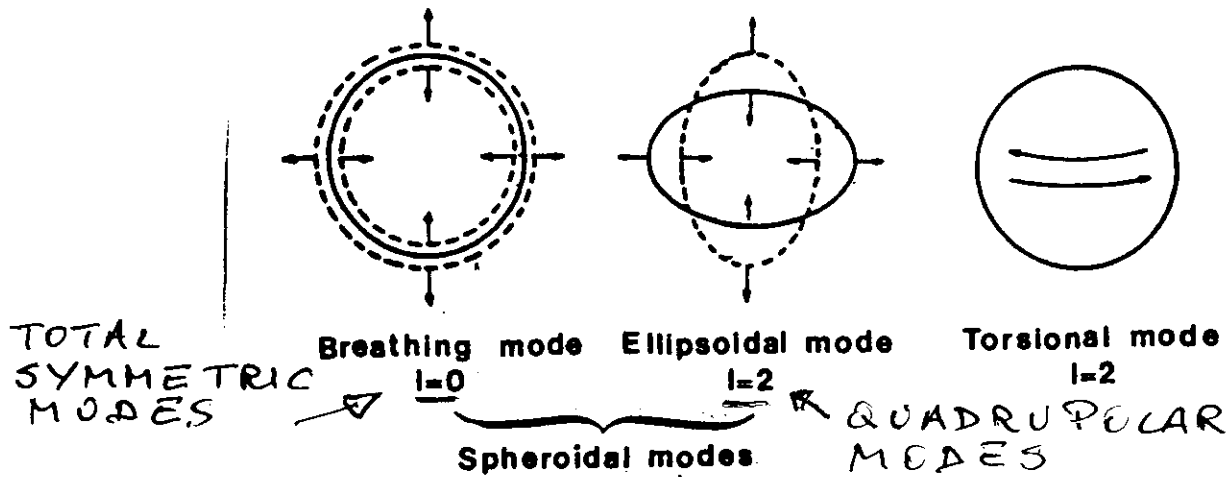


HV



DISCUSSION OF RAMAN DATA.

- LOFIRS IS A SERS EFFECT AND IS DUE TO ACOUSTIC VIBRATIONAL MODES OF A_g COLLOIDAL PARTICLES IN TRANSPARENT HOSTS
- LAMB THEORY: VIBRATIONAL DYNAMICS OF A SPHERICAL BODY (EIGENVALUES + EIGENMODES)



Vibrational modes of a spherical particle.

- ONLY SPHEROIDAL $l=0$ AND $l=2$ MODES ARE RAMAN ACTIVE
- MODES $l=0$ GIVE POLARIZED SPECTRA (VV)
MODES $l=2$ GIVE DEPOLARIZED SPECTRA (HV)
- THE ENERGY OF THESE VIBRATIONAL MODES SCALE WITH THE INVERSE RADIUS (R) OF THE SPHERE
- R CAN BE CALCULATED IF THE LONGITUDINAL AND TRANSVERSE SOUND VELOCITIES ARE KNOWN
- SOUND VELOCITIES IN A_g : $v_l = 3652 \text{ m/s}$
 $v_t = 1660 \text{ m/s}$

$$\omega_{l=0} = 0.9 \cdot \frac{v_l}{2R}$$

$$\omega_{l=2} = 0.85 \cdot \frac{v_t}{2R}$$

$$\omega_{l=0} \propto v_l$$

$$\omega_{l=2} \propto v_t$$

FROM LAMB'S THEORY

$$\omega_s^0 = A_0 \frac{v_e}{2Rc} \quad (l=0)$$

$$\omega_s^2 = A_2 \frac{v_e}{2Rc} \quad (\underline{l=2})$$

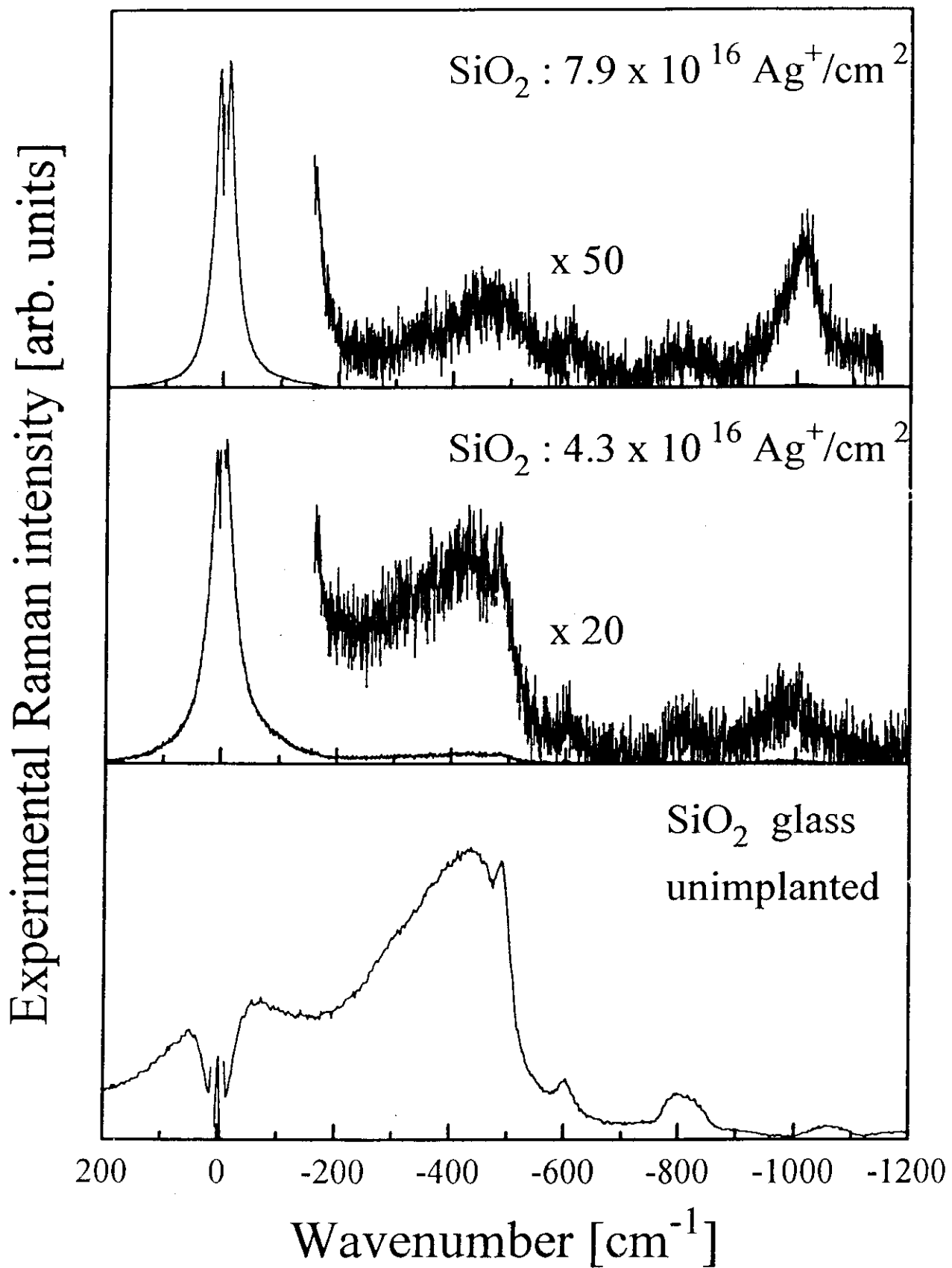
A_0, A_2 DEPEND ON THE RATIO v_e/v_e

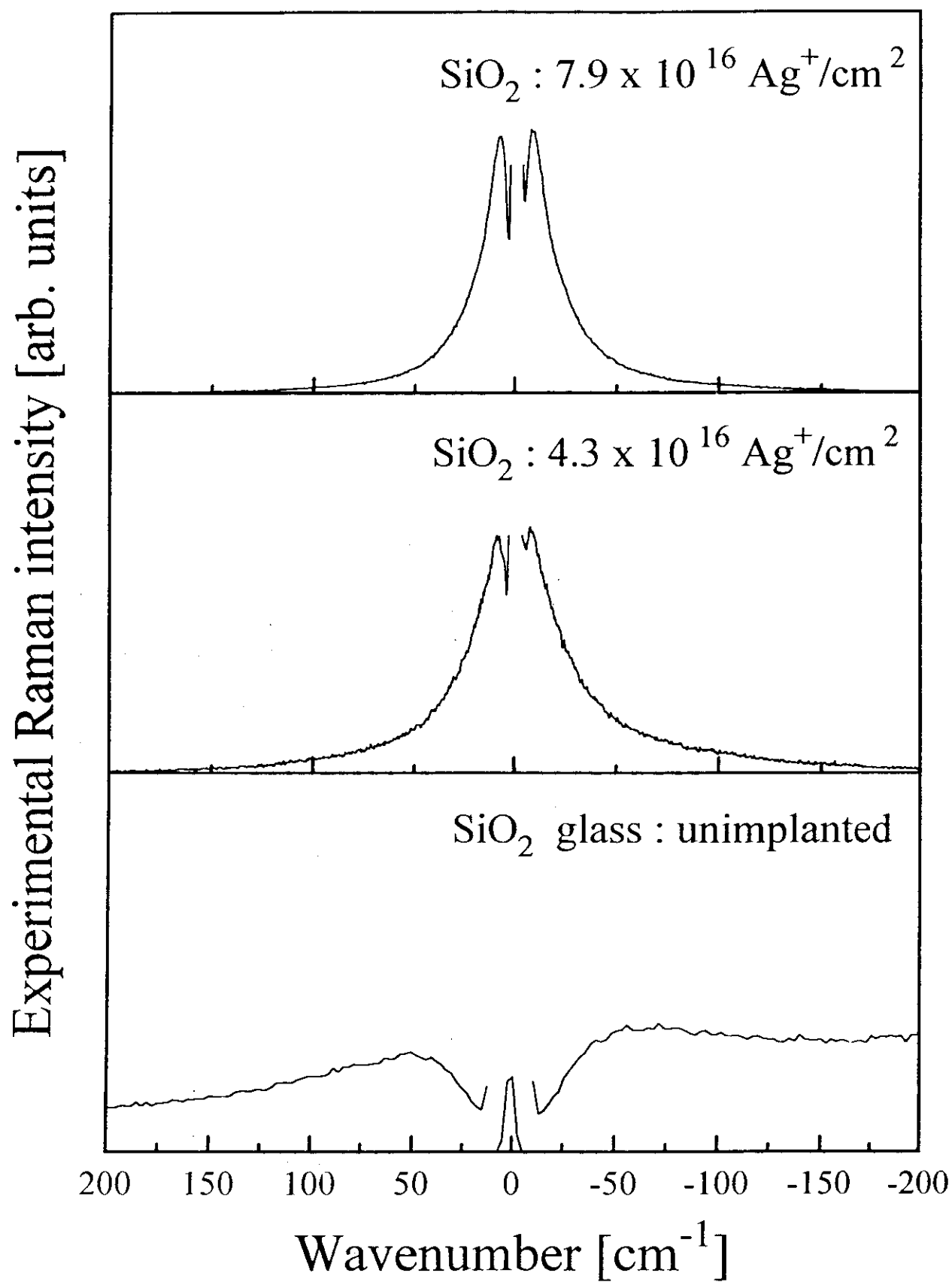
FOR A_f : $A_0 = 0.89$, $A_2 = 0.85$

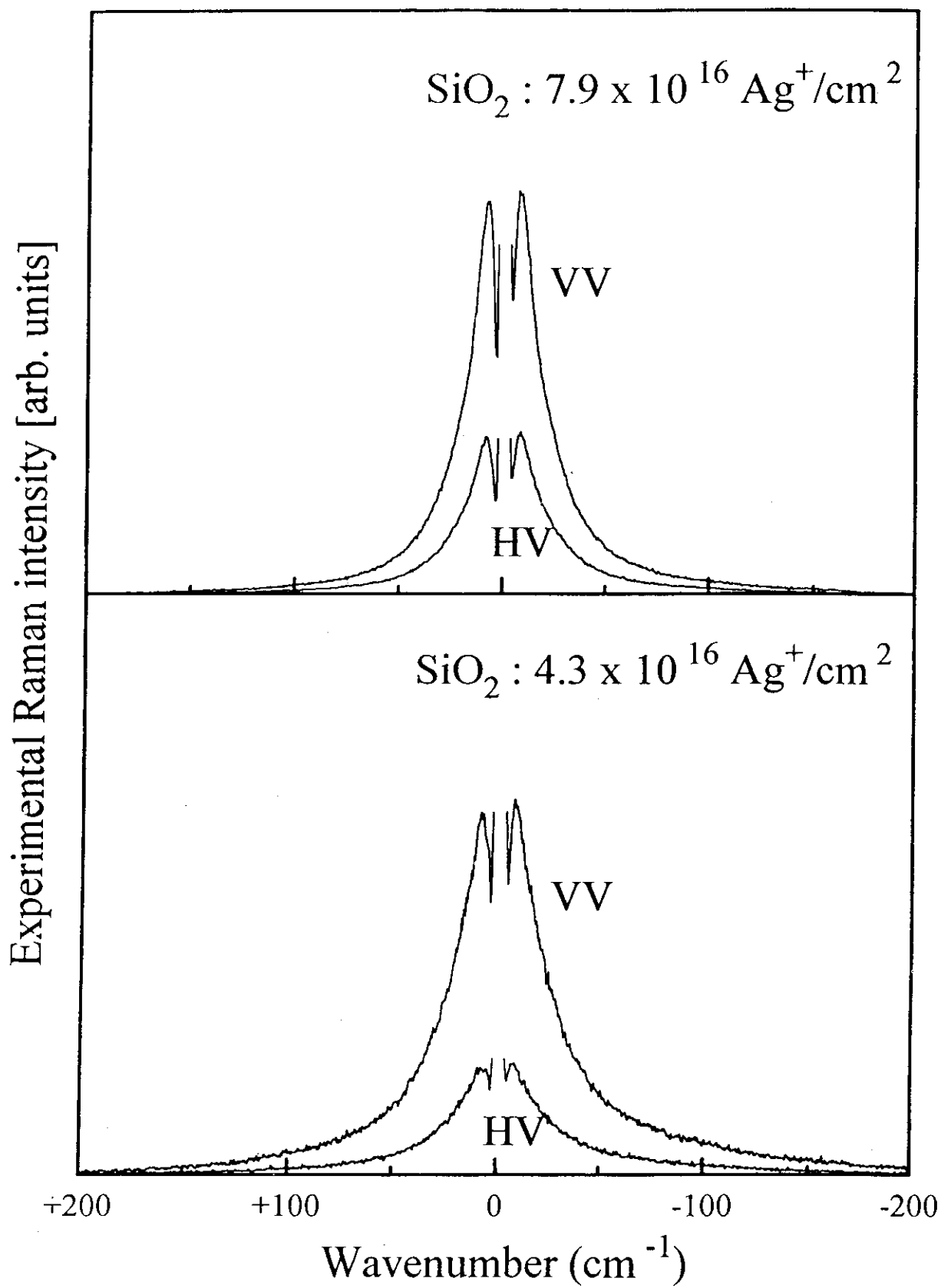
LO FIRST SPECTRA OBTAINED IN HV POLARIZATION CAN BE USED TO DERIVE AN EVALUATION OF THE A_f NANOCUSTER SIZE

DOSE ($\mu\text{u}/\text{cm}^2$)	ω_s^2 (cm^{-1})	$\phi = 2R$ (nm)
7.8×10^{16}	20.2	2.3
10.5×10^{16}	17.2	2.7
13.5×10^{16}	13.6	3.5

RAMAN SPECTROSCOPY ON SiO_2/Ag







$\text{SiO}_2 : 4.3 \times 10^{16} \text{ Ag}^+/\text{cm}^2$

Raman intensity [arb. units]

— : VV

— : HV

◦ : HV x 3.3

$$S = 0.30$$

$$S = \frac{I_{HV}}{I_{VV}}$$

+200

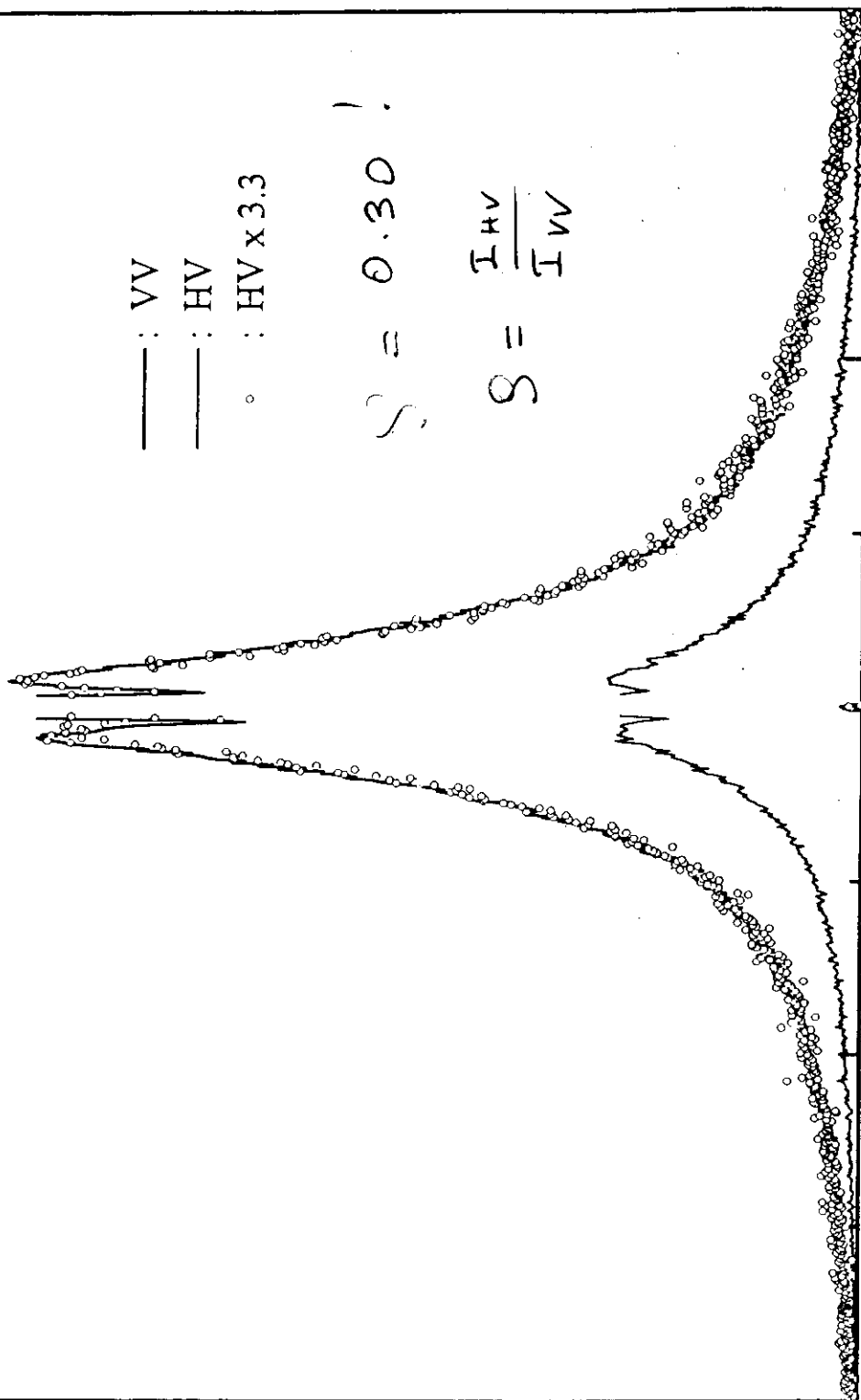
+100

0

-100

-200

Wavenumber [cm^{-1}]



Summary

RBS : Silver ion profiles in implanted substrates.

Single-mode distribution of Ag ions in $\alpha\text{-Al}_2\text{O}_3$;

$R_p \pm \Delta R_p = 85 \pm 30$ nm, for all ion fluences in $\alpha\text{-Al}_2\text{O}_3$;

Bi-modal distribution of Ag at highest fluences in v-SiO₂.

OAS: Shape of Silver clusters.

Some shift of Ag surface plasmon resonance in $\alpha\text{-Al}_2\text{O}_3$;

No apparent shift of the peak position in v-SiO₂;

Ag particles in $\alpha\text{-Al}_2\text{O}_3$: spherical shape, size of 2÷3 nm;

Strong clustering of Ag colloids may occur in v-SiO₂.

RSS: Silver cluster size from the LoFIRS peak energy.

Scattering by acoustic phonon confined in Ag particles;

Main contribution from spheroidal $l=2$ vibrational modes;

Shift of low-frequency peak with the dose in $\alpha\text{-Al}_2\text{O}_3$;

No dose-dependence of the peak position in v-SiO₂;

Ag-particle diameter of 2.4 - 3.6 nm in $\alpha\text{-Al}_2\text{O}_3$;

Bigger size of Ag colloids in v-SiO₂, estimated in ~ 6 nm.

SILVER CLUSTER FORMATION IN IMPLANTED Al_2O_3 SINGLE CRYSTALS

F.L. Freire Jr., N. Broli** and G. Mariotto**

* Departamento de Física, PUC-Rio, Rio de Janeiro, 22452, Brazil
** INFN and Dipartimento di Fisica, Università di Trento, 38050, Italy

ABSTRACT

Single crystals of sapphire were implanted at room temperature with 300 keV-Ag⁺. The metal precipitate was characterized by a multitechnique approach including RBS, optical absorption and Raman spectroscopy. RBS measurements were used to determine the depth-profiles of the implanted ions. Ag depth profiles, derived from RBS are in good agreement with the results predicted by Monte Carlo simulations. Linear absorption spectroscopy has been used to characterize the effects of the ion fluence on the optical properties of the metal colloids in the UV-Vis region. The broad absorption band due to the surface plasmon resonance shows an appreciable red-shift when the fluence of bombarding ions increases. Raman scattering from acoustic vibrations of the silver clusters progressively shifts toward the laser frequency with increasing implantation dose. From low-frequency Raman spectra an evaluation of the average size of metal aggregates was derived.

INTRODUCTION

Dielectric solids, either glasses or crystals, containing metallic or semiconductor dots with nanometer sizes show interesting non-linear optical properties and constitute potentially attractive candidates for applications in integrated optics. In fact, both dielectric and quantum confinement effects give rise to a strong enhancement of the non-linear optical constants of these composite materials [1]. The usual approaches to the fabrication of metal clusters, in glasses or crystalline oxides, include techniques based either on ion-exchange or on ion-implantation [2-5]. Much of the appeal in using implantation lies in the inherent non-equilibrium nature of the process and in the advantages over the other techniques for modifications of surfaces and near-surface properties. In fact, this technique has been used extensively in the past years for synthesizing nonlinear optical materials consisting of metal quantum dots in transparent dielectrics and some basic features of metal nanoclusters in silica have been illustrated in a recent review [6]. Ion-implantation is less often used to create nanocluster composites in crystalline materials due to the extensive damage (substantial bond-breaking and defect formation) at the surface and within the implanted layer) which entails prolonged annealing steps to recover the crystal structure. Recently, the formation of colloidal Ag and Au nanoclusters in Al_2O_3 crystals has been inferred from the analysis of optical and vibrational spectra [2,7].

Here, we report on the results of a multitechnique study, including RBS, optical absorption and Raman spectroscopy, on the Ag-cluster formation in implanted sapphire crystals. RBS experiments were used to determine the depth-profile of the implanted ions. The formation of nanoclusters of Ag in Al_2O_3 gives rise to strong optical absorption at the surface plasmon energy and this is responsible for the coloration of samples. Optical absorption spectroscopy in the UV-Vis region was exploited to study the effects of the ion implantation on the surface plasmon resonance of Ag colloids. The broad absorption band observed at about 440 nm in heavily implanted samples shifts to shorter wavelengths in samples which have been implanted with low fluences of silver ions. Low-frequency Raman spectroscopy measurements were also performed under nearly-resonant excitation with the Ag surface plasmon energy. A strong scattering from acoustic vibrations localized at the surface of the silver clusters is observed. Both optical absorption and Raman spectroscopy results indicate an increasing size of Ag colloids with the ion fluence, and, from low-frequency Raman spectra, an estimation of the mean size of metals particles is obtained.

EXPERIMENTAL PROCEDURES

Commercial Al_2O_3 crystals were cut in form of small pellets with the typical dimensions of $5 \times 5 \times 1 \text{ mm}^3$ and then implanted at room temperature with 300 keV-Ag⁺. The ion fluences ranged from 0.8 to $13.6 \times 10^{16} \text{ ions/cm}^2$ and the current density was $1 \mu\text{A/cm}^2$. The implanted samples were stored in air. Under white light, the samples implanted at low doses show a pale yellowish color, which tends to become more and more reddish at higher ion fluences.

RBS measurements were carried out using 2.0 MeV He⁺ beams and the scattering angle was 165° .

The optical absorption spectra in the range 200-800 nm (or 1.55-6.2 eV) were measured at room-temperature with a Cary 14 dual beam spectrophotometer. A virgin Al_2O_3 crystal was used as a reference sample.

Low-frequency Raman scattering spectra were collected at room temperature using standard equipment consisting of a 1 meter focal length, Jobin-Yvon double-pass monochromator equipped with holographic gratings (2000 lines/mm) and a photon counting system. For the spectra, excitation with either 488.0 nm or 514.5 nm lines of an Ar ion laser were employed. During the measurements the samples were mounted on a home-made sample holder to form an angle near to Brewster angle with the incident beam. Two significant polarization settings were used in order to probe the symmetry character of the vibrational modes responsible for the observed scattering, with the electric field of the incident beam parallel (V) or perpendicular (H) to the scattering plane, the scattered light being filtered by a polarizer with vertical axis (V). These settings allowed us to

obtain VV and HV spectra, respectively. The laser operates so that both spectra, and, therefore, the two spectral intensities, can be used to determine the depolarization factor of the low energy scattering. The typical band-pass of our spectrometer was less than 2.5 cm^{-1} and the spectra were recorded at data intervals of 0.5 cm^{-1} .

RESULTS

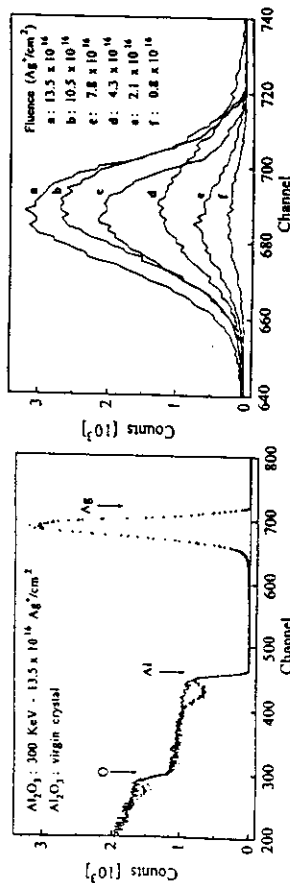


Figure 1 - Random-RBS spectra of the virgin and implanted Al_2O_3 crystals. The arrows indicate the position of the elements.

Figure 2 - Part of the RBS spectra of implanted Al_2O_3 crystals. Only the Ag peak is plotted.

The RBS channel spectrum for the sample implanted with $13.5 \times 10^{16} \text{ Ag/cm}^2$ is shown in Fig. 1, together with that for an unimplanted crystal. The depth profiles as determined from the RBS measurements indicate that the maximum concentration of silver occurs at $R_p = 83 \text{ nm}$ ($\Delta R_p = 26 \text{ nm}$).

Figure 3 shows the optical spectra Ag-implanted Al_2O_3 for five different ion fluences. The formation of Ag nanoclusters gives rises to strong optical absorption at the surface plasmon energy. The extinction spectra show a dramatic intensity

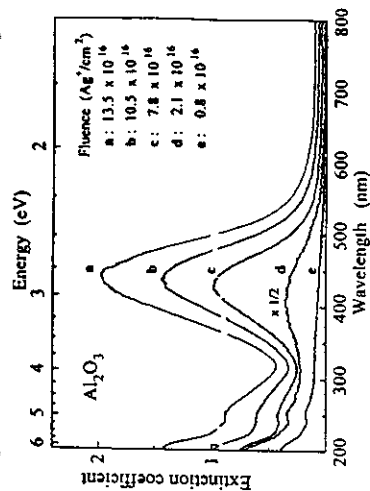


Figure 3 - UV-Vis extinction spectrum of implanted Al_2O_3 crystals.

increase with the ion fluence, while its maximum undergoes a slight shift. In fact, the absorption band for the sample implanted at $2 \times 10^{16} \text{ Ag/cm}^2$ is peaked at about 420 nm . It progressively shifts toward higher wavelengths when the ion fluence rises, peaking at 440 nm for the highest fluence.

Figure 4 shows the experimental Stokes Raman spectrum recorded at room temperature from a crystal implanted with $4.3 \times 10^{16} \text{ Ag/cm}^2$ under the excitation of the 488.0 nm laser line. The spectrum shows a very low frequency asymmetric band extending up to 200 cm^{-1} far from the laser line, and some sharp peaks occurring in the region above 380 cm^{-1} . No Raman feature is observed in the region between 200 and 380 cm^{-1} , where a flat signal is observed.

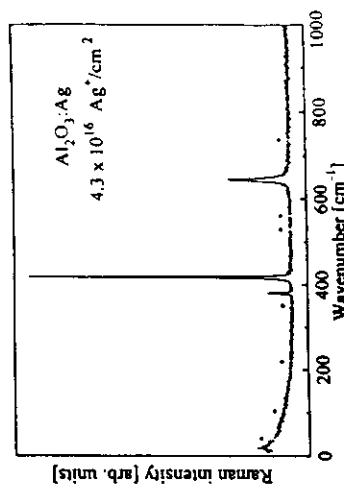


Figure 4 - Raman spectra carried out in VV-polarization from a Ag-implanted Al_2O_3 crystal. Stokes component is shown.

The anti-Stokes and Stokes parts of the low-frequency Raman spectra recorded in VV and HV polarization and are shown in Fig. 5 for the sample implanted with the highest dose. The spectra excited with the 514.5 nm line were almost identical with those shown in Fig. 5. In general, no significant change in the peak position or in the spectral shape for low-energy polarized (VV) and depolarized (HV) spectra of samples implanted at lower fluences was observed by varying the excitation energy.

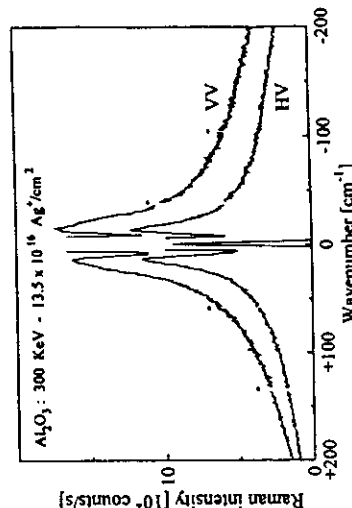


Figure 5-Raman spectra of implanted Al_2O_3 sample recorded at identical excitation conditions: (a) VV and (b) HV polarization. Both Stokes and anti-Stokes regions are reported. Excitation at 488 nm .

Figure 6 reports the low frequency VV Raman spectra (+100 cm⁻¹ to -100 cm⁻¹) for three samples. The scattering intensity shows a dramatic increase with the ion fluence, due to nearly-resonant excitation with the surface plasmon peak. As it appears from the inset, the Raman scattering is peaked at 13.5 cm⁻¹ for the sample implanted with 13.5x10¹⁶ Ag⁺/cm², shifts to 19 cm⁻¹ for samples implanted with 7.8x10¹⁶ Ag⁺/cm².

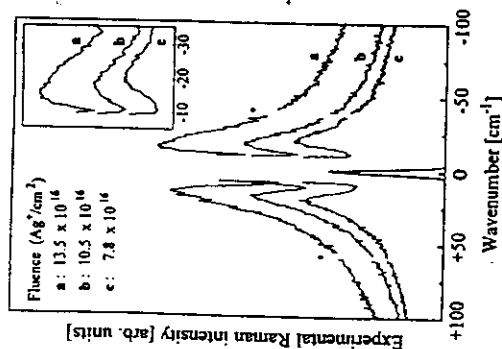


Figure 6 - Low-frequency anti-Stokes and Stokes Raman spectra recorded in the VV polarization. The inset shows the Stokes region. Excitation at 488.0 nm.

CONCLUSIONS

Single crystals of Al₂O₃ were implanted at room temperature with 300 keV-Ag⁺ at several fluences and silver colloid formation has been obtained. The metal precipitates were characterized by a multitechnique approach including RBS, optical absorption and Raman spectroscopy.

The silver profiles calculated from the RBS spectra substantially agree with the predictions of TRIM calculations. The formation of silver colloids was monitored by optical spectroscopy. The extinction spectra shows a dramatic intensity increase with the ion fluence. The small red-shift of the absorption peak suggests the progressive increase of the colloids mean sizes. However, the contribution of higher order absorption terms in Mie theory, i.e., the quadrupole term, cannot be discarded [8].

Raman spectra revealed the composite nature of the implanted materials: they consist of metal clusters embedded into a dielectric matrix. The energy of sharp peaks observed in the high energy correlate very well with the Raman modes of sapphire [9] and should be attributed to the Al₂O₃ matrix. On the other hand, the strong scattering occurring below 200 cm⁻¹ must be connected with the presence of metallic silver. Strong Raman

scattering in the range between few cm⁻¹ and typically 50 cm⁻¹ has been observed in many composite materials containing insulator, metal or semiconductors nanoclusters [10-15]. In these systems, the low-frequency Raman scattering has been discussed in terms of scattering from acoustic phonons confined within the nanoparticles and has been proved to be an efficient method for studying the size of very small aggregates dispersed in the solid matrices [10,11]. Using this approach, and assuming a spherical shape for metal particles, we are able to derive the average size of Ag clusters, which increases from about 2.5 nm to about 3.7 nm, with the ion fluences ranging respectively from 7.8x10¹⁶ Ag/cm² to 13.6x10¹⁶ Ag/cm².

REFERENCES

- [1] For a review: C. Flytzanis, F. Hache, M.C. Klein, D. Richard and Ph. Rousignol, in *Progress in Optics*, Vol. XXIX, E. Wolf (ed.), (North Holland, Amsterdam, 1991) pp. 323-411.
- [2] Ch. Buchal, S.P. Withrow, C.W. White and D.B. Poker, *Ann. Rev. Mater. Sci.* **24** (1994) 125.
- [3] G.W. Arnold, P. Mazzoldi, L. Tramontin, A. Boscolo-Boscoletto and G. Battaglin, *Mat. Res. Soc. Symp. Proc.* **279** (1993) 285.
- [4] F. Caccavalle, G. de Marchi, F. Gonella, P. Mazzoldi, C. Meneghini, A. Quaranta, G.W. Arnold, G. Battaglin and G. Mattei, *Nucl. Instr. Meth. B* (in press).
- [5] R.H. Magruder III, D.H. Osborne Jr. and R.A. Zuhr, *J. Non Cryst. Solids* **176** (1994) 299.
- [6] R.E. Haglund Jr., D.H. Osborne Jr., L. Yang, R. Magruder III, C.W. White and R.A. Zuhr, *Mater. Res. Soc. Symp. Proc.* **316** (1994) 421.
- [7] D.O. Henderson, S.H. Morgan, R. Mu, N. Chen, R.H. Magruder III, C.W. White and R.A. Zuhr, *Mat. Res. Soc. Symp. Proc.* **279** (1993) 439.
- [8] M. Vollmer and U. Kreibitz, in *Nuclear Physics Concepts in the study of Atomic Cluster Physics*, R. Schmidt, H.O. Lutz and R. Dreizler (eds.) Springer-Verlag, Berlin, 1992.
- [9] S.P.S. Porto and R.S. Krishnan, *J. Chem. Phys.* **47** (1971) 1009.
- [10] E. Duval, A. Boukenter and B. Champagnon, *Phys. Rev. Lett.* **56** (1986).
- [11] G. Mariotto, M. Montagna, G. Villani, E. Duval, S. Lafrant, E. Rzepka and C. Mai, *Europhys. Lett.* **6** (1988) 239.
- [12] M. Fujii, T. Nagareda, S. Hayashi and K. Yamamoto, *Phys. Rev. B* **44** (1991) 6243.
- [13] J.A. Capobianco, P.P. Proulx, B. Adrianosolo and B. Champagnon, *Phys. Rev. B* **43** (1991) 10031.
- [14] A. Tanaka, S. Onari and T. Arai, *Phys. Rev. B* **47** (1993) 1237.
- [15] K.E. Lipinska-Kalita, G. Mariotto and E. Zanghellini, *Phil. Mag. B* **71** (1995) 547.

SILVER NANOCLUSTER FORMATION IN IMPLANTED SILICA.

G. MARIOTTO* and F.L. FREIRE Jr.**

* Istituto Nazionale per la Fisica della Materia and Dipartimento di Fisica, Università di Trento, 38050 Povo, TN, Italy.

** Departamento de Fisica, PUC-Rio, Rio de Janeiro, 22452-970, RJ, Brazil

ABSTRACT

Samples of fused silica were implanted at room temperature with 300 keV-Ag⁺ for doses ranging from 0.8×10^{16} to 14×10^{16} ions/cm². A multi-technique approach including Rutherford backscattering spectrometry (RBS), x-ray diffraction (XRD), optical absorption and Raman scattering spectroscopies has been used to characterize silver precipitate. The Ag-depth profiles of samples implanted with doses higher than 6×10^{16} Ag⁺/cm² show a bi-modal distribution, with the appearance of a secondary maximum near the surface. XRD spectra indicated the formation of silver nanocrystals of ~10 nm in size within the heavily implanted samples. Optical absorption has been used to monitor the effects of ion dose on the optical properties of the metal clusters in the UV-Vis region. A single broad absorption band, due to surface plasmon resonance, is peaked at about 400 nm for low implantation doses. For doses higher than 4.3×10^{16} Ag⁺/cm², a second broad band originates at higher wavelength, peaking at 625 nm for the highest dose. The evolution of optical spectra is tentatively discussed in terms of the formation of silver particle aggregates with no longer spherical shape. An estimate of the mean size of silver nanoclusters of about 5.5 nm is obtained from low-frequency Raman scattering due to acoustic vibrations localized at the cluster surface. The discrepancies in the metal particle size obtained from XRD and Raman scattering measurements are discussed with respect to optical absorption data.

INTRODUCTION

Recent increase in research activities on semiconductor and metal nanocrystals embedded in solid transparent matrices is strongly motivated by the potential applications in the field of non-linear processing devices and by the interest in fundamental physics on the excited states of these composite systems. Metal nanoclusters dispersed in transparent matrices present highly enhanced optical non-linearity due to quantum confinement of electrons, which strongly affects the optical properties of these composite systems. Therefore, as far as the opto-electronics applications are concerned, a very crucial step is the accurate control of cluster size during the synthesis process. Ion implantation provides a suitable route to precipitate metal colloids or semiconductor particles in dielectric matrix [1]. The major advantages of ion implantation in metal composite fabrication lies in its capability of incorporating much higher local concentration of metal particles in the host matrix compared to the melt quenching method. Furthermore, it allows for the depth-distribution control of the precipitated nanostructures. Basic properties of metal and semiconductor nanocrystals formed by high-dose ion implantation in fused silica and sapphire have been recently reviewed by White et al. [2].

Since the pioneering work of Arnold and Borders [3] most of the experimental investigations carried out on metal colloid composites were addressed to the characterization of structural and optical properties of metal nanoparticles in glass matrices [4,5]. In particular, a number of publications reported on transmission electron microscopy (TEM) measurements of metal cluster sizes and distribution in fused silica under various implantation and annealing conditions [6-7].

Recently, low-frequency Raman scattering from acoustic vibrations, localized at the nanocluster surface, has been proven to be an efficient non-destructive tool alternative to TEM, to study the size of very small silver particles dispersed in dielectric matrices [8-11]. The analysis of low-frequency Raman scattering data in terms of Lamb's theory, which gives the vibrational frequencies of a homogeneous elastic body with a spherical form [12], provides an estimate of the silver cluster mean size, in reasonable agreement with TEM determinations.

In this work, a multi-technique approach, including RBS, XRD, optical absorption and low-frequency Raman scattering, has been adopted to characterize the silver colloid particles precipitated by ion implantation in fused silica. Our data suggest the formation of simple spherical silver clusters at low implantation doses and of complex aggregates of precipitated silver clusters at implantation doses equal or higher than $7.9 \times 10^{16} \text{ Ag}^+/\text{cm}^2$.

EXPERIMENTAL PROCEDURES

Silver ions were implanted at energy of 300 keV- Ag^+ into commercial fused silica (Herasil) samples, held at room temperature. The implantation doses ranged from 0.8×10^{16} to $14 \times 10^{16} \text{ Ag}^+/\text{cm}^2$ and the current density was $\sim 1 \mu\text{A}/\text{cm}^2$. No post-implantation thermal annealing was performed and the samples were stored in air. Under white light, samples implanted at low doses show a pale yellowish color, which tends to become more grayish when the ion dose increases, indicating the formation of metal colloids. RBS spectra were obtained using 2.0 MeV He^+ beams at a scattering angle of 165° .

X-ray diffraction patterns were recorded in the glancing incidence geometry (incidence angle 1.5°) using the Cu-K_α radiation of a ω -diffractometer (Siemens model D5000). The detector was equipped with a Soller slit and a LiF monochromator. The diffractograms were scanned between 34° and 46° in 2θ in order to detect both the (111) and the (200) diffraction lines of silver.

Optical extinction spectra were carried out in the wavelength range 200 nm to 800 nm using a Cary 14 dual beam spectrophotometer. The spectra were recorded at room temperature in the standard differential mode, with an unimplanted fused silica sample as reference.

Low-frequency Raman spectra were measured at room temperature using a commercial equipment consisting of an Ar^+ -ion laser, of a double monochromator (Jobin Yvon, model Ramanor HG2-S), equipped with holographic gratings (2000 lines/mm), and of a photon counting system. Two polarization settings were used in order to probe the symmetry character of the vibrational modes causing the light scattering, with the electric field of the incident beam parallel (V) or perpendicular (H) to the scattering plane. The scattered light was filtered by a polarizing-plate with vertical axis (V). These settings allowed to record VV and HV spectra, alternatively.

RESULTS AND DISCUSSION

RBS measurements were used to determine depth-profile of Ag^+ ions implanted at 300 keV under different doses in the range 0.8 to $14 \times 10^{16} \text{ ions}/\text{cm}^2$ in silica. Part of the RBS spectra of implanted samples is shown in Fig. 1. The silver depth profiles, as determined from RBS measurements, from samples implanted with a dose lower than $7.9 \times 10^{16} \text{ Ag}^+/\text{cm}^2$, indicate a maximum concentration at $R_p = 83 \text{ nm}$, with a full width at half maximum $\Delta R_p = 26 \text{ nm}$. The full width at half maximum of silver depth profiles in the heavily implanted samples is somehow narrower than those of samples implanted with low ion doses, this is presumably due to formation of metal precipitate grown at high ion doses. Furthermore, the silver depth profiles of samples implanted at ion doses higher than $7.9 \times 10^{16} \text{ Ag}^+/\text{cm}^2$ clearly show a bi-modal distribution, with a

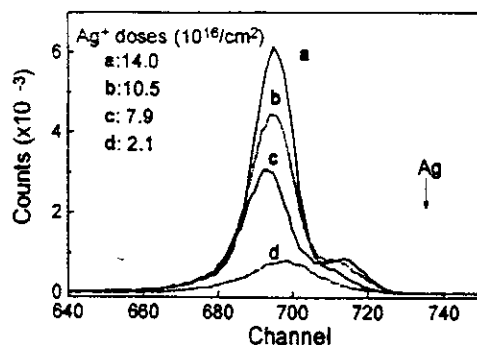


Figure 1- RBS spectra of implanted fused silica implanted with 300 keV-Ag⁺ at different ion doses. Only the energy region around the silver peak is shown. An arrow indicates the position of Ag atoms at the sample surface.

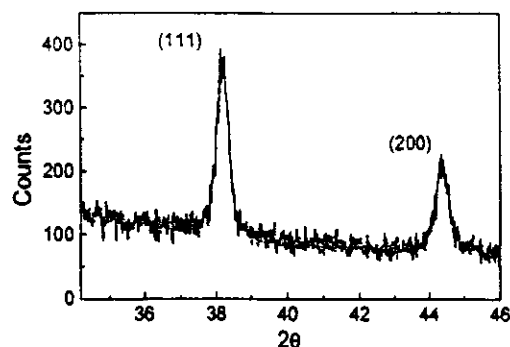


Figure 2- XRD patterns of the fused silica sample, implanted with 7.9×10^{16} Ag⁺/cm², showing both the (111) and the (200) diffraction lines of crystalline silver with cubic structure.

secondary maximum close to the depth where the maximum deposition of energy by the incident ions occurs.

The formation of silver crystalline aggregates at high doses is revealed by x-ray diffraction patterns. Figure 2 shows a XRD spectrum obtained at glazing angle from the sample implanted with 7.9×10^{16} Ag⁺/cm². The presence of silver nanocrystals is revealed by the XRD patterns through the occurrence of sharp reflections from the (111) and the (200) planes of silver with cubic structure, peaking at 38.1° and 44.3°, respectively. Assuming an isotropic distribution of metal particle shape, the Debye-Scherrer analysis of the line broadening of XRD peaks of Fig. 2 indicates an average diameter of ~10 nm for the metal particles in this sample. Similar mean sizes were obtained from XRD patterns of samples implanted with higher ion doses, but no silver diffraction line was observed from our fused silica samples underwent lower ion doses.

The extinction spectra of implanted samples are shown in Fig. 3. The formation of silver colloids even at the lowest dose of 0.8×10^{16} Ag⁺/cm² is revealed by the weak extinction occurring at the surface plasmon energy (~3.1 eV). The extinction spectra show a very strong intensity increase with the ion dose accompanied by a drastic change of their shape. In fact, the absorption spectra of samples implanted at doses not higher than 4.3×10^{16} Ag⁺/cm² consist of a single symmetric band peaked at about 400 nm. They broaden and increase in intensity on the side of higher wavelengths when the ion dose rises, and turn out into a clearly revolved doublet, with the second band peaked at about 625 nm at the highest dose. Similar double-band optical absorption spectra were observed in SiO₂ glass implanted at room temperature with 7.6×10^{16} Ag⁺/cm² of 150 keV [7]. They were discussed in terms of surface plasmon excitation of two types of silver colloids, the sizes of which were estimated to be lower than 10 nm and about 50 nm, according to calculations performed by Arnold and Borders [3]. However, TEM data didn't show the presence of any 50 nm-sized silver cluster in this implanted SiO₂ glass [7].

We interpret our optical data with a structural model, which assumes the occurrence of silver clusters for low implantation doses, and the formation of complex aggregates from precipitated silver clusters, with chain-like or even cluster-like clumping characters, for high implantation doses. The optical absorption spectra of our samples, in fact, close recall the experimental observations of Granquist et al. [13], which were reasonably well simulated using the Maxwell-Garnett formalism [14]. Therefore, the evolution of extinction spectra versus the implantation

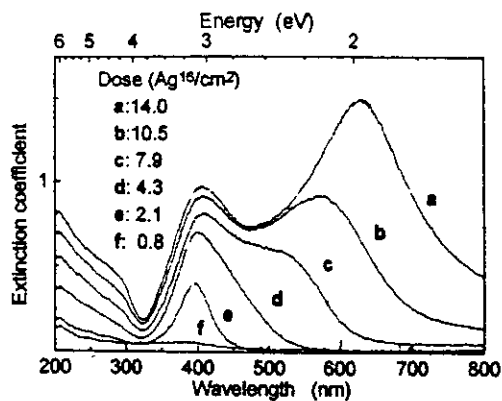


Figure 3- Extinction spectra of fused silica samples Ag-implanted at six different doses.

dose suggests that silver precipitation in fused silica may results into the formation of bigger metal particles, having no longer spherical symmetry.

Figure 4 shows the VV polarized Raman spectra recorded under excitation of the 488.0 nm laser line from two Ag-implanted silica samples (top panels) and from an unimplanted sample (bottom panel). The spectrum obtained from the not-implanted sample fits very well that of fused silica [15]. Raman spectra of both implanted samples show a paramount low-frequency scattering band, extending up to 200 cm^{-1} far from the excitation energy in both anti-Stokes and Stokes sides, which is superimposed on an apparently flat background extending up to about 600 cm^{-1} . A 20 times magnified plot of the region 200 cm^{-1} to 1200 cm^{-1} for sample implanted with $4.3 \times 10^{16}\text{ Ag}^+/\text{cm}^2$ (mid panel) undoubtedly reveals that the underlying background originates from silica matrix. The most significant change is due to the additional band peaked at about 980 cm^{-1} ; this band is related to stretching vibrational mode of terminating Si-OH units in silica [16]. Its

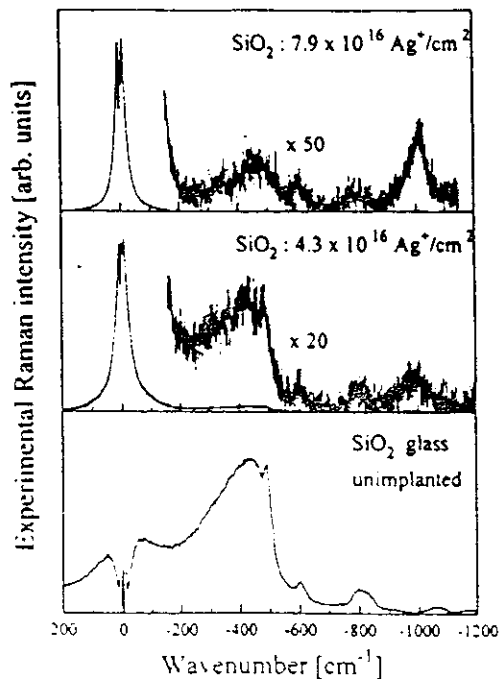


Figure 4- VV-polarized Raman spectra of silver implanted fused silica samples. Both anti-Stokes component below 200 cm^{-1} and the overall Stokes spectrum till 1200 cm^{-1} are shown.

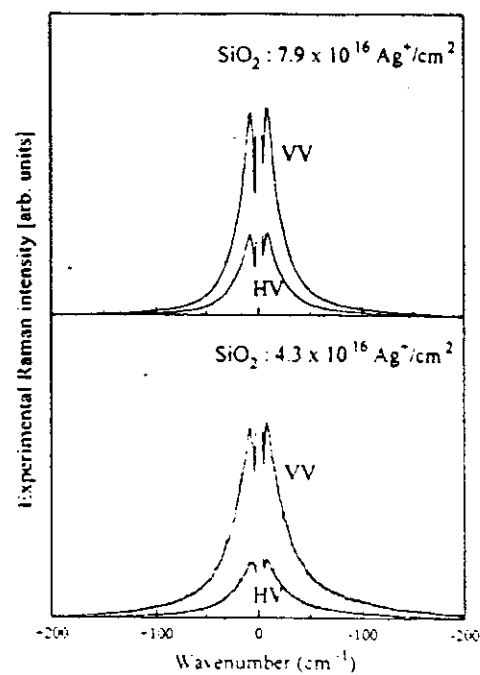


Figure 5- Polarized (VV) and depolarized (UV) low-frequency Raman scattering from two silver implanted silica samples. Both anti-Stokes and Stokes components are reported.

presence indicates that some hydration occurred in implanted sample and that hydrogen decorates the chemically reactive defects produced by the implantation in silica [17]. Similar considerations can be inferred from the 50 times magnified plot for sample implanted under higher dose (top panel), where the relative intensity of the band at 980 cm^{-1} suggests even a more important hydrogen decoration of the internal surface defects, due to ion radiation damage. Obviously, the reduced spectral intensity from the glass matrix observed in these implanted samples results from the strong absorption of exciting radiation by the colloidal surface plasmons. On the other hand, the excitation of surface plasmons localized in the silver clusters enhances the low-frequency Raman scattering observed from implanted samples.

Figure 5 shows both the low-frequency (below 200 cm^{-1}) anti-Stokes and Stokes components of the VV and the HV polarized Raman spectra recorded under identical excitation conditions from two implanted samples. Despite of the remarkably different intensity (about a factor 4 between the two samples), low frequency Raman scattering from both samples peaks at the same frequency ($\sim 8.5\text{ cm}^{-1}$ far from the laser energy, independent of the polarization), showing also a similar spectral shape. Moreover, low-frequency Raman scattering from silver implanted silica is depolarized, and shows a constant depolarization ratio throughout the overall spectral region below 200 cm^{-1} . This conclusion can be easily drawn by considering the shapes of HV and VV spectra of both samples. In other words, the depolarization ratio $\rho = I_{HV}/I_{VV}$, where I_{HV} and I_{VV} are the spectral intensity observed in HV and in VV polarization, is independent of the frequency, and is ≈ 0.3 [18]. All our samples implanted at higher doses show similar spectral characteristics, with respect to the peak position, bandshape and depolarization ratio.

Recent, independent observations [9] of low frequency depolarized Raman scattering from silica films, containing co-sputtered silver particles, show spectral characteristics (peak frequency in the region between 10 and 20 cm^{-1} , same spectral shape in VV and HV polarization, and depolarization ratio $\rho \approx 0.27$) similar to those described above. These results were discussed in terms of acoustic vibrations confined at the surface of the silver clusters. The mean size of metal particles - supposed to be spherical in shape - has been directly derived from the observed peak frequency. In fact, according to Lamb's theory [12], the frequencies of all vibrational modes of a homogeneous elastic sphere with a free surface scale as the inverse of the linear dimensions of the sphere. In addition, group-theory arguments suggest that the only Raman active modes of a sphere are the symmetric ($l=0$) and the quadrupolar ($l=2$) spheroidal modes [19]. Among them only the surface quadrupolar vibrational modes give a Raman depolarized spectrum. Using the results of calculations carried out by Fuji et al. [9], we estimate an average diameter of 5.5 nm for silver clusters precipitated in samples implanted with $4.3 \times 10^{16}\text{ Ag}^+/\text{cm}^2$ or with higher doses. Finally, the depolarization ratio we obtained for the same samples is even closer to $1/3$, i.e. the value expected for silver clusters in fused silica on the basis of theoretical calculation [20]. Therefore, the above findings definitively suggest that low frequency Raman scattering from our implanted fused silica samples originates from spheroidal quadrupolar vibrations localized at the surface of silver cluster of 5.5 nm in size.

CONCLUSIONS

Silver precipitates in fused silica implanted with 300 keV-Ag^+ at some doses, ranging from 0.8×10^{16} to $14 \times 10^{16}\text{ Ag}^+/\text{cm}^2$, were characterized by a multi-technique approach including RBS, XRD, optical absorption and low-frequency Raman scattering. Both, depth profiles and distribution widths of the implanted ions were provided by RBS. XRD patterns clearly indicate the formation of silver crystals of the order of 10 nm in heavily (doses higher $7.9 \times 10^{16}\text{ Ag}^+/\text{cm}^2$) implanted samples. Optical absorption spectra of samples implanted under low doses (lower than

$4.3 \times 10^{16} \text{ Ag}^+/\text{cm}^2$) consist of a broad symmetric band, peaked at the expected surface plasmon resonance energy for silver nanoclusters, which evolve toward a double-band structured spectra for higher implantation doses. On the other hand, Raman scattering from acoustic vibrations of silver particles shows spectral features that are independent of the ion dose. The average size of silver clusters, estimated from the peak position of low-frequency Raman scattering from samples underwent implantation doses between 4.3×10^{16} and $7.9 \times 10^{16} \text{ Ag}^+/\text{cm}^2$ is of order of 5.5 nm.

The discrepancy between the cluster sizes detected by Raman scattering and x-ray diffraction should be not fortuitous, but is probably due to the fact that these two analyzing tools are probing structures characterized by different sizes: the former one probing the precipitated silver clusters, while the latter one probes the metal aggregates formed only at the highest implantation doses. The existence of these types of particles is, in fact, compatible with the observed optical extinction spectra, which suggest the existence of both spherical clusters and aggregates with chain-like or even cluster-like clumping characters in samples implanted with the highest doses.

ACKNOWLEDGMENTS

This work has been partly granted by the Italian CNR and Brazilian CNPq within a bilateral cooperation project. The authors are indebted with Prof. I.J.R. Baumvol (UFRGS-Brazil) for ion implantation. They are also grateful to Dr. M. Cremona for his help in XRD experiments and to Dr. Wolf-Hartmut Schulte for the careful reading of the manuscript.

REFERENCES

1. Ch. Buchal, S.P. Withrow, C.W. White and D.B. Poker, *Annu. Rev. Sci.* **24**, 125 (1994).
2. C.W. White, J.D. Boudai, J.G. Zhu, S.P. Withrow, D.M. Hembree, D.O. Henderson, A. Ueda, Y.S. Tung and R. Mu, *Mat. Res. Soc. Symp. Proc.* **396**, 377 (1996).
3. G.W. Arnold and J. A. Borders, *J. Appl. Phys.* **48**, 1488 (1977).
4. H. Hosono, Y. Abe and N. Matsunami, *Appl. Phys. Lett.* **60**, 2613 (1992).
5. R.H. Magruder III, Li Yang, R.F. Haglund, Jr., C.W. White, Lina Yang, L. Dorsinville and R.R. Alfano, *Appl. Phys. Lett.* **62**, 1730 (1993).
6. H. Hosono, H. Fukushima, Y. Abe, R. A. Weeks and R.A. Zuhr, *J. Non-Cryst. Solids* **143**, 157 (1992).
7. N. Matsunami and H. Hosono, *Appl. Phys. Lett.* **63**, 2050 (1993).
8. G. Mariotto, M. Montagna, G. Viliani, E. Duval, S. Lefrant, E. Rzepka and C. Mai, *Europhys. Lett.* **6**, 239 (1988).
9. M. Fuji, T. Nagareda, S. Hayashi and K. Yamamoto, *Phys. Rev. B* **44**, 6243 (1991).
10. M. Ferrari, F. Gonella, M. Montagna and C. Tosello, *J. Appl. Phys.* **79**, 2055 (1996).
11. F.L. Freire Jr., N. Broll and G. Mariotto, *Mat. Res. Soc. Sym. Proc.* **396**, 385 (1996).
12. H. Lamb, *Proc. London Math. Soc.* **13**, 187 (1882).
13. C.G. Granquist, N. Calander and O. Hunderi, *Solid State Commun.* **31**, 249 (1979).
14. C.G. Granquist and O. Hunderi, *Phys. Rev. B* **16**, 3513 (1977).
15. C.A.M. Mulder and A.A.J.M. Damen, *J. Non-Cryst. Solids* **93**, 387 (1987).
16. G. Mariotto, M. Montagna, G. Viliani, R. Campostrini and G. Carturan, *J. Phys. C* **21**, L797 (1988).
17. C. Burman and W.A. Lanford, *J. Appl. Phys.* **54**, 2312 (1983).
18. G. Mariotto and F.L. Freire Jr., to be published.
19. E. Duval, *Phys. Rev. B* **46**, 5795 (1992).
20. M. Montagna and R. Dusi, *Phys. Rev. B* **52**, 10080 (1995).

